Radiative Transfer in Accreting Environments

Thesis by

Avery E. Broderick

In Partial Fulfillment of the Requirements

for the Degree of

Doctor of Philosophy

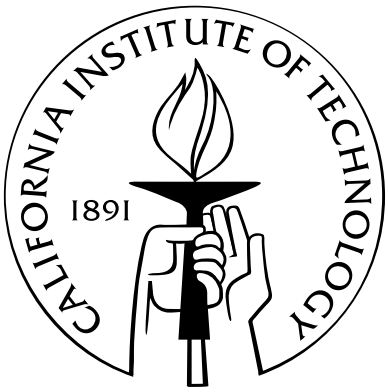

California Institute of Technology

Pasadena, California

2004

(Defended May 26, 2004)

© 2004
Avery E. Broderick
All Rights Reserved

To Alyssa, Ariel, and Alessandra,

who have given so freely of their time and moral support.

Acknowledgements

No effort is undertaken in vacuum. Hence I would be remiss not to mention the considerable support and assistance that I have received which made this project possible. I have had productive conversations with both Eric Agol and Andrew McFadyen which produced a number of useful insights. Yasser Rathore provided an invaluable sounding board for many of the ideas discussed here, and an excellent computer science teacher. Lastly, but not least, Roger Blandford has supplied many intuitive and fundamental insights, as is his style. Furthermore, he has done so frequently at my leisure despite his intractable schedule and countless responsibilities. There are of course many others too numerous to list who have contributed in less tangible ways, including those who have worked so hard to produce the relaxed and supportive environment present at TAPIR, those who have aided me in achieving my educational goals, and those who made it possible for me to pursue them.

Abstract

Accretion onto compact objects plays a central role in high-energy astrophysics. The process of accretion can substantially affect the magnetic field strength and geometry (e.g., via the magneto-rotational instability or dynamo processes) and the accreting plasma density. The presence of the compact object itself can significantly affect the character and structure of the accreting plasma as well as its emission. This is especially true, in the case of an accreting black hole, when a significant fraction of the emission originates or passes near the horizon. To address this, we develop a manifestly covariant magnetoionic theory, capable of tracing rays in the geometric optics approximation through a magnetized plasma in a general relativistic environment. This is discussed for both the cold and warm, ion and pair plasmas. We also address the problem of performing polarized radiative transfer covariantly in these environments, considering in particular the anisotropic nature of magnetized plasmas, the gravitational redshift and Doppler shift, the transport of the polarization vector along the ray, and the ellipticity of the plasma eigenmodes.

The presence of relativity qualitatively changes the dispersion relation, introducing a third branch. In addition it significantly augments various polarized emission and transfer effects in strongly sheared flows, such as jets. Additionally, we demonstrate that it is possible, due to refraction coupled with the existence of a horizon, to generate a net circular polarization regardless of the intrinsic polarization of the emission mechanism. We find that this is not likely to be of significant importance for circular polarization in AGN (including the Galactic center and M81). However, in the context of X-ray binaries, this may produce measurable circular polarizations in the infrared.

We also develop a formalism for performing polarized radiative transfer through

tangled magnetic fields. We find that for Faraday thick plasmas with a net magnetic helicity (but not necessarily a net magnetic field) it is possible to generate a circular polarization fraction which increases with frequency, as is observed to be the case in the Galactic center. In this case the handedness of the circular polarization is determined by the angular momentum of the accretion disk. This mechanism can be applied to extragalactic AGN and naturally explains the low degrees of circular polarization observed. As with the refractive mechanism, this may also be applied to X-ray binaries, and predicts $\sim 10\%$ polarization fractions at infrared wavelengths. Again, this provides a significant motivation for the development of infrared polarimetry.

Contents

List of Figures

Part I

Introduction

Chapter 1

Motivation

Magnetized plasmas are common in the Universe. While they can arise in many situations, the most exotic involve compact objects. Because accretion onto compact objects can power high luminosities, these tend to be the most easily observed as well. The presence of the compact object can play a significant role in the character of the magnetized plasma and the resulting emission. The very process of accretion can greatly alter the geometry and strength of the magnetic field (e.g., via the magneto-rotational instability (MRI) or dynamo processes) and the density and composition of the plasma. In addition, when a significant portion of the emission originates near, or passes near to, the compact object general relativistic effects may become important. Examples of when this may be the case include accreting black holes in active galactic nuclei (AGN) with masses $\sim 10^{6-9} M_{\odot}$, stellar mass black holes in X-ray binaries (XRBs) with masses $\sim 10 M_{\odot}$. Neutron stars in the form of pulsars or magnetars also provide an energetic environment in which both general relativity and plasma physics enter. As a direct result, techniques to perform plasma calculations in a general relativistic environment and with tangled magnetic fields are necessary to provide quantitative comparison with recent and future spectropolarimetric measurements. In the following sections some of the salient observational motivations and their contexts are briefly discussed.

1.1 AGN

1.1.1 General Observations

AGN are observationally characterized by broad-band continuum emission, extreme luminosity, small angular size, and commonly strong variability. AGN spectra tend to be flat, usually extending from the infrared to the X rays, and frequently reaching as far down as the radio and up as far as the γ-rays. This broad range in frequencies imply the presence of highly nonthermal particle populations.

Their high luminosities, which make it possible to observe them at high redshift ($z \lesssim 6$) and thus make them important as cosmological tools, typically range from 10^{40} to 10^{48} erg/s and are frequently sufficient to outshine their host galaxies ($\sim 10^{44}$ erg/s). Based upon the Eddington limit, a lower bound may be placed upon AGN masses,

$$M \gtrsim 10^6 \left(\frac{L}{10^{44}\ \mathrm{erg/s}} \right) M_\odot \,, \tag{1.1}$$

which ranges from 10^5 to $10^{10}\ M_\odot$. Again this is comparable to the mass of a typical host galaxy of $10^{10}\ M_\odot$, implying that AGN may also be dynamically important.

Despite being so luminous, AGN appear extremely compact. The most stringent limits come in the form of observations of stellar orbits about the AGN in the Galactic center (which will be discussed in more detail in Section 1.1.4). These restrict its size to be no greater than 5×10^{-4} pc, despite having a dynamically measured mass of $3.5 \times 10^6\ M_\odot$ (Schödel et al., 2003; Ghez et al., 2003). For more distant AGN such direct measurements are not feasible. Nonetheless, it is possible to use their effective temperatures and the observed flux to estimate their angular size. This places a limit of

$$\theta = 87(1+z)^2 \left(\frac{F_{\mathrm{obs}}}{10^{-11}\ \mathrm{ergcm^{-2}s^{-1}}} \right)^{1/2} \left(\frac{T_{\mathrm{eff}}}{10^3\ \mathrm{K}} \right)^{-2} \mu\mathrm{as} \,, \tag{1.2}$$

(Krolik, 1999), which while not nearly as constraining as the measurements of the Galactic center is also relatively compact considering their luminosity and mass.

Many nearby AGN also exhibit jets with large radio lobes over kpc scales. These jets are extremely well collimated and are known to be highly relativistic. Superlu-

minal ejections along the jets have been measured to propagate with bulk Lorentz factors greater than 20 (i.e., apparent velocities greater than $20c$) (see, e.g., Kellermann et al., 2000; Denn et al., 2000). Highly nonthermal synchrotron emission can be seen from the radio to the X rays from knots within some jets, implying an efficient reheating mechanism and the presence of strong magnetic fields. Further evidence of this has been provided by linear polarization measurements along the jets (Lister, 2001).

Combined, the first two properties suggest that AGN are powered by supermassive black holes. In the case of the Galactic center, the observations of stellar orbits have already ruled out a number of alternative models discussed in the literature, including fermion balls (Schödel et al., 2002), boson stars (Torres et al., 2000), and clusters of dark astrophysical objects (Maoz, 1998). In the context of distant AGN, and in particular Seyfert 1 galaxies, additional spectroscopic observations in the soft X rays have found a line-like feature that is typically interpreted as a fluorescence line of iron in a low ionization state. This Fe K_α line is peculiar in that it is extremely broad and asymmetric, presumably due to general relativistic effects within the ergosphere of a rotating black hole (see, e.g., Tanaka et al., 1995; Pariev et al., 2001; Fabian et al., 2002; Reynolds & Nowak, 2003). If this is correct, then not only are AGN inhabited by supermassive black holes, but a sizable portion of the X-ray emission is arising from very near the horizon ($\lesssim 10M$).

AGN have been known to vary on timescales ranging from minutes to years at all energies (Barr et al., 1980; Glass, 1981). The X-ray variability ($\sim 20\%$) timescales (10^{3-5} s) in particular have been shown to be correlated with the X-ray luminosity, with longer time scales being associated with higher luminosities (Green et al., 1993; Barr & Mushotzky, 1986). This has subsequently been shown to imply an inverse relationship between X-ray variability and the central black hole mass (Papadakis, 2004). Flares in the X-ray (Baganoff et al., 2001) and the near infrared have also been oberved (Genzel et al., 2003). More recently, simultaneous observations of X-ray and near infrared flares in the Galactic center have been made (Schödel et al., 2004; Eckart et al., 2004; Genzel et al., 2003). These have implied that the emission

Object Type	Point-like	Broad-band	Broad Lines	Narrow Lines	Polarized
Radio-loud quasars	Yes	Yes	Yes	Yes	Some
Broad-line radio galaxies	Yes	Yes	Yes	Yes	Weak
Narrow-line radio galaxies	No	No	No	Yes	No
OVV quasars	Yes	Yes	Yes	Yes	Yes
BL Lac objects	Yes	Yes	No	No	Yes

Table 1.1: Listed are a number of the radio loud subclasses of AGN with some typical characteristics (adapted from Krolik, 1999).

at these frequencies can originate within tens of gravitational radii (M in geometrized units) at most in some AGN.

In addition to these generic properties, many AGN also exhibit a number of specialized properties which are not shared by the entire group. These may include characteristics such as broad or narrow absorption lines, radio brightness, X-ray brightness, variability, polarization, and even total luminosity, which serve to categorize AGN into a number of subclasses. Since, in the context of AGN, we will be primarily concerned with radio observations, we have restricted ourselves to those AGN which are radio loud. In Table 1.1.1 some of the typical characteristics of these AGN are listed.

1.1.2 Unified Model of AGN

Perhaps not surprisingly, many of the properties in the previous section can be explained by a model powered by an accreting supermassive black hole (see, e.g., Urry & Padovani, 1995; Blandford, 1985). As schematically shown in Figure 1.1, central features of this model include jets, a geometrically thick accretion flow or molecular torus, a hot corona, and outflows of varying types. Based upon the geometry of the line of sight of the observer, this model can reproduce the varied properties of the different types of AGN. Blazars result when the line of sight lies within the jet, producing a high degree of variability due to precessing and shocking jets and high flux due to the extreme beaming. Broad-line radio galaxies are produced when the line of sight passes through the inhomogeneous outflows in the evacuated funnel, but not

the jet, leading to broad absorption lines as a result of the high proper motions of clumps in the outflows. Narrow-line radio galaxies are observed when the line of sight passes through the accretion flow directly.

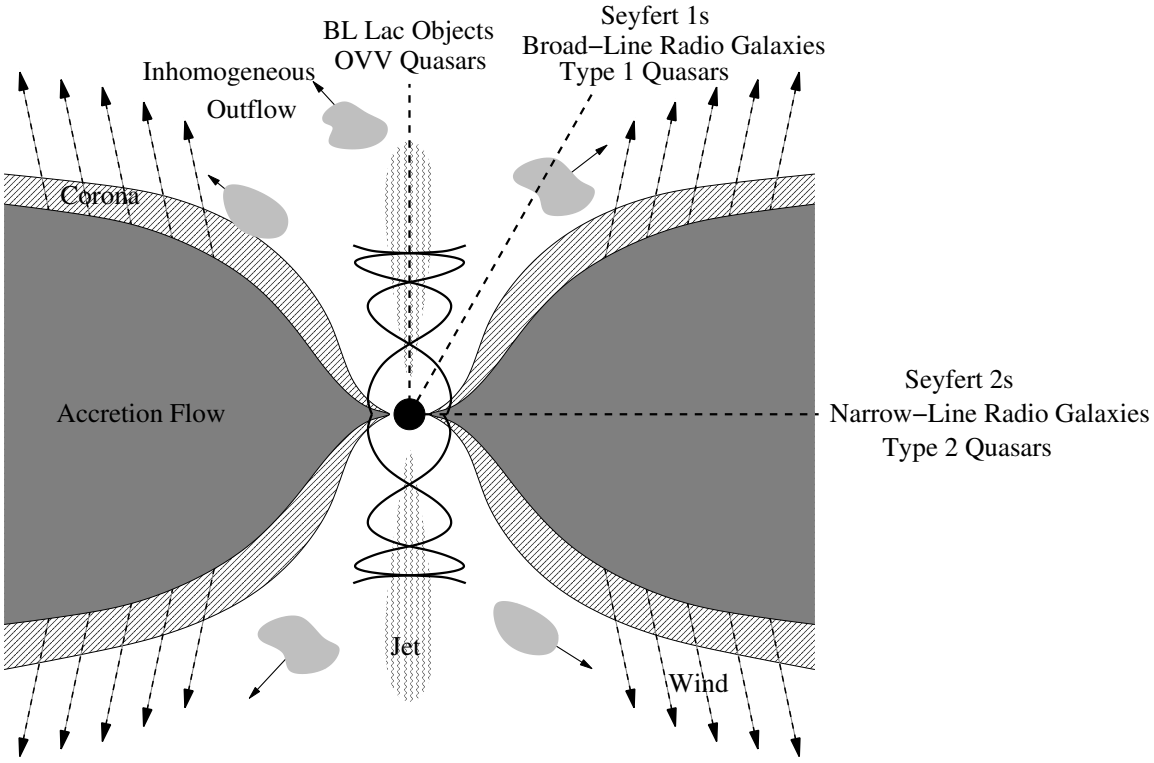

Figure 1.1: Diagram of the main features of the Unified Model of AGN. In particular, the central supermassive black hole, geometrically thick accretion flow, inhomogeneous outflow, magnetic fields, jets, hot corona, and the winds are shown. For reference, the lines of sight associated with the different types of observed AGN are also shown.

The hard X-ray emission is produced via Comptonization of soft disk photons in the hot corona (presumably heated by magnetic reconnection), with the rest of the emission due to the disk or the outflows. It is currently unclear where the majority of the emission originates, but the aforementioned Fe K_α fluorescence line implies that a significant portion of the luminosity is from the innermost regions. Nonetheless, the so-called Unified Model is therefore able to explain in a single model (*i*) the prodigious energy output of AGN, (*ii*) the high degree of variability in blazars, (*iii*) the broad and narrow line features in the different types of AGN, (*iv*) the high effective temperature,

and (v) the point-like nature of most AGN.

1.1.3 Polarimetric Observations

Polarization has long been recognized as diagnostic of the magnetic structure of AGN. More recently, spectropolarimetry has been important in constraining AGN models. As a result, there have been a number of polarization surveys of AGN. Many of these have focused upon linear polarization, which is presumably due to jet emission. These tend to be polarized at the 1-10% level (see, e.g., Saikia & Salter, 1988, and references therein), and has usually been interpreted as providing evidence for strong, ordered magnetic fields within the jets (see, e.g., Lister, 2001). However, of more interest here are the circular polarization surveys.

In one of the earliest catalogs of circular polarization measurements in AGN, Weiler & de Pater (1983) detected circular polarization at the 2σ level in 46 of 120 sources. Unfortunately, more than two circular polarization measurements were made on only 55 of the 120 objects. In all cases the circular polarization was found to be less than 0.5% despite the fact that the linear polarization fraction was as high as 10%. As discussed in Saikia & Salter (1988), there was no correlation between the linear and circular polarization fractions. While not surprising, considering that the mechanisms for linear-to-circular conversion depend upon many of the details of the source, it does suggest that the circular polarization may be produced in a region distinct from that producing the linear polarization.

In a subsequent study by Komesaroff et al. (1984), 22 compact extragalactic radio sources (ostensibly quasars and BL Lac objects) were monitored at 5 GHz for a six year period. During this time both the total intensity, linear, and circular polarization were measured. In 16 of the 22 objects circular polarization was detected at the 4σ level or greater (but still at the few tenths of a percent level). In general, the circular polarization had the highest fractional variability (typically greater than 60%), followed by the linear polarization (about 50%), and the intensity (about 25%). Despite this heirarchy, there appeared to be no correlation in the variability between

these components. There were instances of the polarization angle rotating by more than 90° without any significant change in the circular polarization fraction. The fact that the circular polarization rarely changed sign suggested that this variability was not due to cancellation between orthogonally polarized regions, as implied in some cases for the linear polarization, further differentiating the two.

More recent observations with sensitivities to circular polarizations as low as 0.01% were performed by Rayner et al. (2000). In these it was found that BL Lac objects and quasars had a systematically higher circular polarization fractions than non-blazar, radio-loud AGN. Furthermore, high levels of variability and flat/inverted spectra were associated with circular polarization detections, again suggesting that it is produced in a compact region.

Homan et al. (2001) have carried out parsec-scale polarization observations of 40 radio-loud AGN. In 11 circular polarization was detected at the 3σ level. Of these, 6 had been previous observed by Komesaroff et al. (1984), and 5 had been found to have maintained their sense of polarization, demonstrating the presence of long term ($\gtrsim$ 20 yr) stability in this property. These observations were distinct from earlier measurements due to their tremendously increased spatial resolution. The circular polarization was found to be associated with either the jet base or the radio core, in stark contrast to the linear polarization. Together with the previous observations, this implicates the central black hole and associated accretion flow in the production of the observed circular polarization.

1.1.4 Low-Luminosity AGN (Sgr A*& M81)

A subset of galactic nuclei are extremely underluminous (cf. luminosities of 10^{27} – 10^{30} erg/sHz with 10^{37} – 10^{43} erg/sHz for normal AGN). Nonetheless, despite being substantially sub-Eddington, these objects still show features characteristic of AGN, including flat spectra and high brightness temperatures.

The best-known low-luminosity AGN (LLAGN) is Sgr A*, the radio point source associated with the Galactic center. A number of observations have found circular

polarization between 1.4 and 15 GHz at the $\sim 1\%$ level (Bower et al., 1999; Sault & Macquart, 1999; Bower et al., 2002). Despite this, linear polarization is not present at these frequencies, in contrast to circular polarization in blazars. However, linear polarization without significant circular polarization has been found at significantly higher frequencies (112 GHz) (Aitken et al., 2000; Bower, 2003), implying a significant change in the environment over this range in wavelengths. The circular polarization varies on timescales no longer than days by as much as 100% despite having a constant sign over more than two decades (Bower, 2003). The largest variations appear to be associated with the transition from a low to flaring state in which the spectral index of the polarization fraction in the flaring state may reach as high as +1 (Bower, 2003). It is remarkable that the circular polarization fraction *increases* with frequency until reaching a high-frequency cutoff (presumably below 112 GHz). The typical mechanisms by which circular polarization is produced, e.g., synchrotron emission, Faraday conversion, etc., result in both a large linear polarization and a circular polarization fraction that decreases with increasing frequency. Hence, the polarization measurements in Sgr A* imply either a nontrivial environment or the presence of a novel polarization mechanism.

A radio survey (8.4 GHz) for polarization in LLAGN was performed by Bower et al. (2002). Of 11 sources, 3 were observed to have statistically significant levels of linear polarization (0.3–1.7%) and 1, M81, with a significant circular polarization (0.25%). In many ways M81 appears very similar to Sgr A*. These include the total luminosity, the presence of an inverted radio spectra, and similar circular and linear polarization behavior below 22 GHz. Of particular interest is the fact that as with Sgr A*, in M81 the circular polarization fraction increases with frequency at GHz frequencies, suggesting that this may be a generic behavior.

Recently, a putative jet-like feature has been observed in the X rays in Sgr A* (Baganoff, 2004). It can be distinguished from the diffuse X-ray background by the hardness of its spectrum ($4-8$ keV as opposed to $2-4$ keV). This feature is normal to the Galactic plane, and aligned with magnetic filiments at 30 pc. It ends in two X-ray lobes (emitting near 2 keV) which require an input power on the order

of 10^{39} erg/s. This has fueled speculation upon the source of the radio emission in the Galactic center, and in particular, whether it is produced in an accretion flow or the formative region of a jet. Bower et al. (2004) have limited the region responsible for the emission at 7mm to be less than 50 M across. This coupled with the lack of linear polarization below approximately 100 GHz and degree of circular polarization between 2 and 15 GHz implies that the forming radio jet would need to be relatively wide ($\gtrsim 15\,M$ across), heavily pair dominated (the lepton to baryon ratio must be in or above the thousands), and must be expanding laterally by this stage, limiting the size of the acceleration mechanism to $10 - 20\,M$.

In each of these observations, either the innermost regions of the accretion flow or the base of the jets are implicated in the production of the circular polarization. In the context of the former, general relativity becomes important and can play a dominant role if the emission region is small enough. In the latter, special relativistic shearing flows will be present. Since these regions are expected to be hot and thus highly ionized, plasma physics can be expected to be important as well. Both relativity and plasma physics can alter the spectral properties via gravitational lensing and refraction. In particular, it is possible to significantly alter the polarimetric properties via plasma transfer effects and differential refraction of the two polarization eigenmodes of the plasma coupled with general relativity. Therefore, as more detailed and sensitive polarimetric observations become available, it is necessary to develop a covariant plasma theory to make polarimetric predictions given particular AGN models.

1.2 X-ray Binaries

While much of this work was initially motivated by polarimetric observations in LLAGN, X-ray binaries (XRBs) provide an stellar mass analogue. Hence, many of the effects discussed for LLAGN can also be applied to these systems as well.

1.2.1 General Properties

Stellar mass black holes ($10M_{\odot}$) are the expected evolutionary end point of massive stars. Approximately $\sim$ 300 million such black holes are believed to exist in the Galaxy (Van den Heuvel, 1992; Brown & Bethe, 1994; Timmes et al., 1996), however due to the considerable difficulty in observing these, only a small number have been detected. Traditionally this has been accomplished by observing compact object binaries, specifically X-ray binaries. More recently, micro-lensing has been used as a technique to observe Galactic halo black holes. However, due to the serendipitous nature of the event required (a black hole must transit near a star in the Large or Small Magellanic clouds), the number of micro-lensing events is also small. Furthermore, this does not provide a method to study the detected black holes further after the micro-lensing event. Therefore, X-ray binaries provide the only current known environment in which stellar mass black holes may be studied in detail.

The most straightforward way to distinguish X-ray binaries containing black holes from those containing neutron stars is to measure the mass of the compact object. To date, no neutron stars with masses greater than $2M_{\odot}$ have been found to exist, nor is one expected for theoretical reasons (see, e.g., Shapiro & Teukolsky, 1983). Hence providing a lower limit on the mass function of the compact companion of $2.5M_{\odot}$ is sufficient to demonstrate that the X-ray binary does not contain a neutron star. This has been done in 17 of the 18 "confirmed" stellar mass black holes (see Table 1.2).

If a mass limit is not available, circumstantial evidence can come in the form of exhibiting a subset of the characteristic spectral/temporal states, or a lack of type I X-ray bursts. The current theory of type I X-ray bursts involves thermonuclear reactions on the surface of an accreting neutron star. Therefore, the lack of type I X-ray bursts may imply the lack of a stellar surface and hence the presence of a horizon (Narayan & Heyl, 2002).

Object	Mass ($M_\odot$)	$F_{\text{X-ray}}$ (μJy)	D (kpc)
V518 Per	$3.2 - 13.2$	3×10^2	2.6 ± 0.7
LMC X-3	$5.9 - 9.2$	6×10^1	50 ± 2.3
LMC X-1	$4.0 - 10.0$	3×10^1	50 ± 2.3
V616 Mon	$8.7 - 12.9$	5×10^4	1.2 ± 0.1
MM Vel	$6.3 - 8.0$	8×10^2	5.0 ± 1.3
KV UMa	$6.5 - 7.2$	4×10^1	1.8 ± 0.5
GU Mus	$6.5 - 8.2$	3×10^3	5 ± 1.3
IL Lupi	$7.4 - 11.4$	1.5×10^4	7.5 ± 0.5
V381 Nor	$8.4 - 10.8$	7×10^3	5.3 ± 2.3
V1033 Sco	$6.0 - 6.6$	3.9×10^3	3.2 ± 0.2
V821 Ara	—	1.1×10^3	4
V2107 Oph	$5.6 - 8.3$	3.6×10^3	8 ± 2
V4641 Sgr	$6.8 - 7.4$	1.3×10^4	$7.4 - 12.3$
V406 Vul	$7.6 - 12$	1.5×10^3	11
V1487 Aql	$10.0 - 18.0$	3.7×10^3	$11 - 12$
Cyg X-1	$6.9 - 13.2$	2.3×10^3	2.0 ± 0.1
QZ Vul	$7.1 - 7.8$	1.1×10^4	2.7 ± 0.7
V404 Cyg	$10.1 - 13.4$	2×10^4	$2.2 - 3.7$

Table 1.2: Listed are the 18 "confirmed" black hole binaries and some of their associated properties (adapted from McClintock & Remillard, 2003).

1.2.2 Analogy with AGN

Stellar mass black holes in X-ray binaries in the low/hard or quiescent state share many of the features of LLAGN. Both are tremendously underluminous accreting black holes (McClintock et al., 2003). However, the considerable difference in the mass scale must be taken into account. Some simple scaling laws can be obtained in terms of the radiative efficiency ($\eta \equiv L/\dot{M}c^2$) and the accretion rate ($\dot{M}$). At this point it is necessary to differentiate between the rate at which mass is supplied and that at which it is accreted.

Radiatively inefficient accretion flows (RIAFs) onto black holes have been implicated in many LLAGN. The radiative efficiency can be low in two limiting situations: when the accreting matter is substantially optically thick so that the photon diffusion time is long in comparison to the accretion timescale, and when the accreting matter is extremely tenuous. In this later case, the electrons and the protons can not

couple efficiently and hence the gravitational binding energy of the baryons can not be effectively transferred to the emitting electrons.

RAIFS are typically introduced to explain extremely sub-Eddington luminosities in which putative radiative efficiencies prevented the accreting matter from releasing its binding energy before crossing the horizon (see, e.g., Shapiro et al., 1976; Ichimaru, 1977; Rees et al., 1982). Despite this, in order to reproduce the low luminosity observed in LLAGN, extremely small accretion rates are still necessary. It was subsequently realized that the accreting matter necessarily had a positive Bernoulli constant, and hence was in some sense unbound (Blandford & Begelman, 1999). This resulted in the so-called advection dominated inflow-outflow solutions (ADIOS). In these the vast majority of the accreting gas leaves the system in the form of a wind as a result of the accretion of the remaining gas. The low luminosity is then due to the limited amount of gas that is actually accreted, despite reasonable radiative efficiencies. The primary distinction between the ADAF and ADIOS models is in the manner in which the accretion power is limited. In the former, the matter available to be accreted is assumed to be small, i.e., it is supply limited. In the later, despite having substantial amounts of mass available, the amount actually accreted is small, i.e., it is demand limited.

If the mass accretion rate is given in terms of the Eddington rate (see, e.g., equation 1.1), $\dot{M} = \epsilon \dot{M}_{\rm Edd}$, the luminosity will be proportional to M:

$$\eta \dot{M} c^2 = L \propto \epsilon \dot{M}_{\rm Edd} \propto \epsilon M \,. \tag{1.3}$$

This will also be proportional to the local density near the horizon of the black hole, and hence the plasma density (since it is likely to be highly ionized), by

$$\dot{M} \simeq 4\pi M^2 c \beta \rho \,, \tag{1.4}$$

where β is the inflow speed. From equipartition, this may be related to the total energy stored in the magnetic field ($\mathcal{B}$), divided by the typical timescale (M/c), and

hence

$$L \propto \eta M^2 \mathcal{B}^2 \,. \tag{1.5}$$

Therefore, combining this with equation (1.3), the resulting dependence of the cyclotron and plasma frequencies (ω_B and ω_P, respectively) is

$$\omega_P \sim \omega_B \propto \sqrt{\frac{\epsilon}{\eta M}} \,. \tag{1.6}$$

As a result, the frequencies at which interesting plasma effects appear can be expected to scale as $\sqrt{\epsilon/\eta M}$.

In the context of the Galactic center, the presence of two X-ray lobes, which are presumably powered by shocking winds from an accretion disk, imply that mass is supplied at nearly 10^{22} g/s. Of this, approximately 1% is accreted by the black hole, giving $\epsilon_{\mathrm{SgrA}^*} \simeq 2 \times 10^{-4}$. Therefore, in order to produce the putative luminosity observed it is necessary for $\eta_{\mathrm{SgrA}^*} \sim 10^{-5}$. If both the radiative efficiency and accretion rate in units of the Eddington rate are similar for XRBs, then if the peculiar radio polarization properties of LLAGN are a result of plasma effects, they would be expected to appear in the infrared. By varying the radiative efficiency and accretion rate this can be moved into the optical and ultraviolet. Currently, there have not been *any* measurements of infrared polarization of black holes, stellar mass or otherwise. Therefore, the analogy of XRBs with LLAGN provides a strong motivation for extending polarimetry into the infrared.

1.3 Neutron Stars

The third known class of general relativistic objects are neutron stars. Pulsars are perhaps the most obvious place in which to apply a general relativistic plasma theory. Refraction has been shown to have considerable effects upon pulse profiles (see, e.g., Barnard & Arons, 1986; Arons & Barnard, 1986; Petrova, 2000; Weltevrede et al., 2003), and while general relativity may not be important in the emission region, the dynamical nature of the problem is greatly simplified by the use of a covariant

formalism.

A less obvious but more tractable application to neutron stars is in the context of magnetar atmospheres. It has been shown that magnetar strength fields (10^{13} G) polarize the vacuum, leading to plasma-like transfer and refractive effects (see, e.g., Lloyd et al., 2003; Heyl et al., 2003; Shaviv et al., 1999). Lai & Ho (2003a) have shown that the transition from standard plasma effects to those associated with the birefringence of the vacuum can produce polarimetric signatures in the X rays diagnostic of the magnetic field structure in the neutron star atmosphere. However, this is a highly anisotropic environment due to the presence of the ultra-strong magnetic field. As a result, the radiative transfer properties are strongly dependent upon the direction of propagation of the photons (Lai & Ho, 2003b). Therefore, the inclusion of refraction can have a strong effect upon the magnitude and type of polarimetric properties that would be expected, despite the fact that the neutron star atmosphere is on the order of a centimeter deep.

1.4 Fundamental Physics

In addition to modeling the observed properties of astronomical objects, there are several fundamental reasons to develop a covariant formulation of plasma physics. First and foremost is that it offers a way to probe strong field relativity using polarization observations. That strong field relativity will play a significant role in the polarimetric properties of black hole systems has been appreciated for some time now (see, e.g., Connors & Stark, 1977; Connors et al., 1980; Laor et al., 1990). Because significant polarization effects only occur for photons that pass near the horizon, using polarization it is possible to select out photons that necessarily probe this region of spacetime. However, this presumes the existence of an accretion disk model that is at least partially understood. Note that because purely general relativistic effects are achromatic for $\lambda \ll M$, using polarized and unpolarized spectra it should be possible to deconvolve those effects that are due to general relativity and accretion disk physics. This will be altered by the presence of plasma effects appearing at low

frequencies, which may be be used as an additional constraint.

The second area of fundamental astrophysics that can be probed in this way is accretion disk physics. If the behavior of the black hole is assumed, then the observed spectral and polarimetric properties depend only upon the accretion flow. There has been considerable effort expended in the astrophysical community to do just this. However, much of this has either ignored general relativity (which is a good approximation for emission distant from the horizon) or ignored significant plasma effects. Currently there has been no study which includes refractive plasma effects. Despite the fact that refraction would appear to complicate this procedure, and would occur only at low frequencies, it would provide a direct measurement of the plasma density and distribution. While for low frequencies the photosphere may be large, polarization measurements may be able to select out emission from near the horizon. Hence, if measured, refraction would be an invaluable tool in constraining accretion physics.

Chapter 2

Previous Work

A great deal of work has been done on understanding polarized radiative transfer. These investigations have principally been focused upon either polarized emission, transfer effects, or general relativistic effects. Few have been concerned with covariant formulations of plasma theory and none have considered the full problem of an accreting compact object.

2.1 Intrinsic Emission

The most straightforward way in which to produce a polarized flux is by a polarized emission mechanism. The best-known example in astrophysics is synchrotron emission, first discussed by Westfold (1959). As is well-known, synchrotron emission can produce high degrees of linear polarization (as high as 100% for sufficiently steep power-law electron distributions). It is possible for a moderately relativistic electron distributions to generate some circular polarization as well, however, this is reduced by the inverse of the typical Lorentz factor of the emitting electron distribution (Legg & Westfold, 1968). In the limit of nonrelativistic electrons, this simply reduces to the cyclotron resonances which are known to be highly circularly polarized (see, e.g., Rybicki & Lightman, 1979).

Radiative physics can be significantly complicated by the presence of a plasma. The most obvious difference is the change in phase velocity that enters into the Liénard-Wiechert potentials, the so-called Razin suppression (see, e.g., Rybicki &

Lightman, 1979). However, in nonuniform or anisotropic plasmas (e.g., a magnetized plasma), care must be taken in choosing which quantities are evolved via the transfer equations and in how the emissivities and absorptivities are calculated. Nonetheless, a considerable literature exists regarding the techniques involved in calculating the transfer coefficients and emissivities for warm plasmas (see, e.g., Montgomery & Tidman, 1964; Bekefi, 1966; Krall & Trivelpiece, 1973).

Obtaining a net polarization from a macroscopic source via a polarized intrinsic emission mechanism requires some large scale structure. In the case of synchrotron or cyclotron emission, this requires a large scale ordered magnetic field. Furthermore, in order to reproduce the peculiar polarimetric properties of LLAGN, some secondary processing of the photons must occur to remove the predominant linear polarization.

2.2 Plasma Transfer Effects

The study of polarized transfer effects through magnetized media dates back to the discovery of Faraday rotation (Faraday, 1846). Since that time a considerable literature has developed regarding the polarized radiative transfer through magnetized plasmas. The two primary plasma transfer effects are Faraday rotation, which results in a rotation of the plane of polarization, and Faraday conversion (also known as Faraday pulsation, generalized Faraday rotation, and Faraday repolarization), which leads to the cyclical creation and destruction of circular polarization (Sazonov & Tsytovich, 1968; Sazonov, 1969; Jones & O'Dell, 1977b,a). Both are a result of the difference in the phase velocities between the two electromagnetic plasma eigenmodes. While Faraday conversion typically is discussed in the context of pair plasmas, both can occur in ion plasmas as the plasma eigenmodes are generally elliptically polarized. Faraday rotation and polarization have been employed in attempts to explain the polarimetric properties of LLAGN (Beckert & Falcke, 2002). However, as described in Macquart (2002), Faraday rotation and conversion make strong predictions for the frequency dependence of polarization fractions, which are not present in the observations. Of course, this may be the result of significant structure in the source.

A more stringent requirement upon transfer effects is the strong depolarization of linear polarization at low frequencies. Strong Faraday depolarization necessarily eliminates circular polarization created via Faraday pulsation as well. Furthermore, in regions which are strongly Faraday depolarized, a consistent handedness for the circular polarization would not be expected unless a highly ordered environment was present. Inhomogeneous environments (and in particular inhomogeneous magnetic fields) have begun to be theoretically investigated. Studies have fallen loosely into three categories: (*i*) investigations of slowly varying inhomogeneous materials and the resulting geometric phase effects (see, e.g., Budden & Smith, 1976; Jones & O'Dell, 1977a; Enßlin, 2003), (*ii*) discussions of scintillation by inhomogeneous screens (Macquart & Melrose, 2000), and (*iii*) attempts to calculate emergent properties after averaging over a large number of field reversals (Ruszkowski & Begelman, 2002). Applications of the first and the third to the polarimetric observations in Sgr A* have found it necessary to assume significant structure in the magnetic field, usually due to an weak average homogeneous magnetic field. Highly variable circular polarization can be produced by scintillation (Macquart & Melrose, 2000). In this case, small-scale inhomogeneities in the source or an intervening screen produce small random phase shifts along an initially smooth plane wave. Due to the anisotropic nature of magnetized plasmas, the magnitudes of these phase shifts will differ for the two plasma eigenmodes, creating small regions of circular polarization via a process similar to Faraday conversion. In this case, the variability will likely be dominated by that of the screen, and will occur over the timescale which inhomogeneities change appreciable (e.g., the eddy turn over time if the inhomogeneities are due to turbulence). However, the net polarization produced via scintillation must necessarily vanish unless there is a considerable amount of structure in the scintillating screen itself. All of these mechanisms have difficulty reproducing the long term stability in the sign of polarization. An alternative in which the polarization sense is determined by the angular momentum (the only other axial vector in the problem), in an accretion disk involving tangled fields (a net field is unnecessary) is analyzed in Part III.

None of these effects account for general or special relativistic effects or for refrac-

tive effects. As a result, these must be modified appropriately to apply to a general relativistic environment. Furthermore, as stated it does not appear likely that any of these transfer effects alone could produce the observed polarimetric behavior.

2.3 General Relativistic Transfer Effects

The importance of gravitational lensing upon the spectral and polarimetric properties of accreting black holes was first appreciated by Connors & Stark (1977). They considered the case of an optically thick accretion disk with a scattering atmosphere orbiting a stellar mass black hole in the context of an XRB. While the standard electron scattering theory, first worked out by Chandrasekhar (1960), predicts degrees of X-ray polarization as high as 10%, general relativistic effects (via disk lensing), and special relativistic effects (via Lorentz boosting of the emission regions and polarization vectors), serve to depolarize the emission substantially. These calculations were carried out by directly integrating the parallel transport equations. Subsequent calculations using more physically motivated disk models were performed by making use of a complex spinor constant that is admitted by type (2,2) spacetimes (the Penrose-Walker constant), and in particular the Kerr spacetime (see, e.g., Chandrasekhar, 1992; Connors et al., 1980; Walker & Penrose, 1970). Since refractive plasma effects can be safely ignored at X-ray energies, the paths taken by the photons are simply null geodesics. Associated with each null vector is a spinor, which may be decomposed into the space orthogonal to the null vector itself. As a direct result, it is possible to cast the polarization unit vector as a spinor and hence utilize the Penrose-Walker constant to parallel propagate the polarization unit vector without explicitly integrating the parallel transport equations.

Laor et al. (1990) extended this analysis to AGN, albeit in the optical/ultraviolet regime. Here they found results similar to those of Connors et al. (1980) and Connors & Stark (1977). In both it was found that the polarization spectrum was diagnostic of both the accretion theory and the spin of the central black hole. Qualitatively, higher black hole spins allow the accretion disk to extend further down to the horizon, leading

to larger lensing and boosting effects, and lower net linear polarizations.

Because a growing body of numerical simulations suggest that accretion flows may be highly inhomogeneous (Hawley et al., 2001), some effort has been spent studying the polarimetric properties of blobs of material (Bao et al., 1997) as a first approximation. Alternatively, a cylindrically symmetric disk illuminated by asymmetric corona has also been considered (Bao et al., 1998; Dovciak et al., 2004). In both cases, general relativity leads to spectral and polarimetric effects that are diagnostic of the emission geometry.

In addition to gravitational lensing, the gravitational redshift has been shown to be important. Perhaps the best-known example of a gravitational redshift in AGN is the observation of the iron K_α line (see Section 1.1.1). In recent efforts both the geometric and redshift effects have been incorporated in an attempt to model the response (or lack thereof) of the K_α to variations in the hard X-ray emission (Matt et al., 1997; Miniutti et al., 2003; Reynolds & Nowak, 2003).

There have been some attempts to include plasma effects with the aforementioned general relativistic effects. Bromley et al. (2001) attempted to do this by evolving the two plasma modes independently along null geodesics, thus mapping the intrinsic polarization of the emission mechanism to the observer at infinity. However, the use of the approximation in which the plasma eigenmodes can be evolved independently is not valid in the limit of vanishing plasma density. Furthermore, since only high frequencies were considered, this did not address the circular polarization measurements.

In general, none of these calculations can be trivially extended into the radio regime (or infrared in the case of XRBs) since they explicitly ignore refractive effects which may become important at low frequencies.

2.4 Covariant Plasma Theory

Plasma theory, and more specifically magnetoionic theory, has been well developed in the context of radio wave propagation in the ionosphere (see, e.g., Boyd & Sander-

son, 1969; Budden, 1961; Ginzburg, 1970; Krall & Trivelpiece, 1973; Dendy, 1990). This has typically been done via dynamics (cold plasmas) or kinetic theory (warm plasmas), and has been successful in reproducing many of the radio phenomena in the atmosphere.

There have been a number of attempts to develop a covariant plasma theory. This was done earliest in the context of pulsar magnetospheres to account for the dynamical nature of the environment (Barnard & Arons, 1986; Arons & Barnard, 1986; Petrova, 2000, 2002; Weltevrede et al., 2003), in which it was found that refraction had considerable implications for the pulse morphology. Kulsrud & Loeb (1992) employed a variational approach to the unmagnetized plasma, deriving a covariant dispersion relation and the appropriate equations to define rays in the geometric optics approximation. Long wavelength waves in one-dimensional magnetized plasma were considered by Gedalin et al. (1998) and Melrose et al. (1999). Besides being one-dimensional, these are developed only for conditions appropriate for special relativistic applications. A two fluid approach was utilized in Melrose & Gedalin (2001) to produce a fully covariant theory. However, due to the fluid treatment, it also is limited to long wavelengths and is not a generalization of the magnetoionic theory which has been so successful in the atmosphere.

Chapter 3

Summary of This Work

In this work, we develop a covariant generalization of the well-known magnetoionic theory. In Chapter 4, this is done in analogy with the nonrelativistic derivations where possible in order to make use of the techniques used in conventional plasma theory, facilitate comparison, and ensure consistency. Different plasma compositions/environments are characterized solely by a covariant conductivity which allows a wide degree of application, far beyond those discussed here.

The problem of radiative transfer is treated in Chapter 5. Polarized radiative transfer is complicated by (*i*) the presence gravitational radiation, (*ii*) the presence of the plasma, (*iii*) the anisotropy associated with the magnetic field, and most importantly (*iv*) the highly refractive nature of the environment. The first three can be partly addressed by evolving the photon occupation number, and appropriately defined analogues of the Stoke's parameters Q, U, V, instead of the Stoke's parameters directly. The last requires a detailed discussion of when the plasma eigenmodes are and are not coupled. Fortunately, a detailed discussion of this does exist in the conventional literature (see, e.g., Ginzburg, 1970), which may be subsequently extended to a covariant form.

Some didactic example applications of the formalism developed in Chapters 4 and 5 are presented in Chapter 6 as well as applications to the Galactic center, M81, and XRBs in Chapter 7. It is found that due to the presence of a horizon and refraction it is possible to produce a predominantly circularly polarized signal. While this appears to be only marginally plausible in the context of LLAGN, it does have interesting

implications for XRBs.

In Part III, a completely distinct yet complementary problem is addressed, namely, that of tangled magnetic fields. We find that in Faraday thick plasmas with a net magnetic helicity, though not necessarily a net magnetic field, it is possible to generate a circular polarization signal which *increases* with frequency, reaching a high-frequency cutoff. We then apply this to the Galactic center and XRBs, finding circular polarization fractions as high as 10%, again providing a motivation for polarimetric observations in the infrared.

Finally, in Part IV we review the results and discuss the implications of this work for polarimetry.

Unless otherwise noted, we use geometrized units ($G = c = 1$) and metric signature $(-+++)$.

Part II

Covariant Magnetoionic Theory

Chapter 4

Tracing Rays

The natural place to begin a study of plasma modes is the covariant formulation of Maxwell's equations (see, e.g., Misner et al., 1973):

$$\nabla_\mu F^{\nu\mu} = 4\pi J^\nu \;\text{ and }\; \nabla_\mu {}^*F^{\nu\mu} = 0\,, \tag{4.1}$$

where $F^{\nu\mu} \equiv \nabla^\nu A^\mu - \nabla^\mu A^\nu$ is the electromagnetic field tensor, ${}^*F^{\nu\mu} \equiv \frac{1}{2}\varepsilon^{\nu\mu\alpha\beta}F_{\alpha\beta}$ is the dual to $F^{\mu\nu}$ ($\varepsilon^{\mu\nu\alpha\beta}$ is the Levi-Civita pseudo tensor) , and J^ν is the current four-vector. In order to close this set of equations, a relation between the current and the electromagnetic fields is required. For the field strengths of interest here, this will take the form of Ohm's Law:

$$J^\nu = \sigma^\nu{}_\mu F^{\mu\alpha}\overline{u}_\alpha\,, \tag{4.2}$$

where $\overline{u}^\mu$ is the average plasma four-velocity and $\sigma^\nu{}_\mu$ is the covariant generalization of the conductivity tensor, defined by this relationship. As a result of the anti-symmetry of $F^{\mu\nu}$, the conductivity will in general have only nine physically meaningful components, namely the spatial components in the slicing orthogonal to $\overline{u}^\mu$. Nonetheless, in order to investigate the behaviors of plasma modes in a general relativistic environment, it is necessary to express the conductivity in this covariant fashion.

This can be more naturally expressed in terms of $E^\mu \equiv F^{\mu\nu}\overline{u}_\nu$ and $B^\mu \equiv {}^*F^{\mu\nu}\overline{u}_\nu$, the four-vectors coincident with the electric and magnetic field vectors in the locally flat center-of-mass rest (LFCR) frame of the plasma. In terms of E^μ and B^μ, the

electromagnetic field tensor and its dual take the forms

$$F^{\mu\nu} = \overline{u}^{\mu} E^{\nu} - E^{\mu} \overline{u}^{\nu} + \varepsilon^{\mu\nu\alpha\beta} \, \overline{u}_{\alpha} \, B_{\beta} \, , \tag{4.3}$$

$$^{*}F^{\mu\nu} = B^{\mu} \overline{u}^{\nu} - \overline{u}^{\mu} B^{\nu} + \varepsilon^{\mu\nu\alpha\beta} \, \overline{u}_{\alpha} \, E_{\beta} \, . \tag{4.4}$$

Inserting these and Ohm's law into Maxwell's equations yields eight partial differential equations,

$$\nabla_{\mu} \left(\overline{u}^{\nu} E^{\mu} - E^{\nu} \overline{u}^{\mu} + \varepsilon^{\nu\mu\alpha\beta} \, \overline{u}_{\alpha} \, B_{\beta} \right) = 4\pi \sigma^{\nu}{}_{\mu} E^{\mu} \, , \tag{4.5}$$

$$\nabla_{\mu} \left(B^{\nu} \overline{u}^{\mu} - \overline{u}^{\nu} B^{\mu} + \varepsilon^{\nu\mu\alpha\beta} \, \overline{u}_{\alpha} \, E_{\beta} \right) = 0 \, , \tag{4.6}$$

which may be solved for E^{μ} and B^{μ} given an explicit form of the conductivity.

4.1 Geometric Optics Approximation

The general case can be prohibitively difficult to solve for physically interesting plasmas. Fortunately, the problem can be significantly simplified by making use of a two length scale expansion (also known as the WKB, Eikonal, or Geometric Optics approximations) in terms of $\lambda / \mathcal{L}$, where λ and $\mathcal{L}$ are the wavelength and typical plasma length scale, respectively. In this approximation it is assumed that the electric and magnetic fields have a slowly varying amplitude with a rapidly varying phase, i.e., E^{μ}, $B^{\mu} \propto \exp\left(iS\right)$ where S is the action, and $\nabla_{\mu} S = k_{\mu}$ defines the wave four-vector. Then, to first order in $\lambda / \mathcal{L}$, Maxwell's equations are

$$k_{\mu} \left(\overline{u}^{\nu} E^{\mu} - E^{\nu} \overline{u}^{\mu} + \varepsilon^{\nu\mu\alpha\beta} \, \overline{u}_{\alpha} \, B_{\beta} \right) = 4\pi \sigma^{\nu}{}_{\mu} E^{\mu} \, , \tag{4.7}$$

$$k_{\mu} \left(\overline{u}^{\nu} B^{\mu} - B^{\nu} \overline{u}^{\mu} + \varepsilon^{\nu\mu\alpha\beta} \, \overline{u}_{\alpha} \, E_{\beta} \right) = 0 \, . \tag{4.8}$$

At this point it is useful to point out a number of properties of E^{μ} and B^{μ} that follow directly from their definitions and Maxwell's equations.

(i) $\overline{u}_{\mu} E^{\mu} = \overline{u}_{\mu} B^{\mu} = 0$, which follows directly from the definitions of E^{μ} and B^{μ} and

the antisymmetry of $F^{\mu\nu}$ and ${}^*F^{\mu\nu}$.

(ii) $k_\mu B^\mu = 0$, which follows from equation (4.8) and the definition of B^μ.

(iii) $E_\mu B^\mu = 0$, which follows from $\omega E_\mu B^\mu = E_\mu k_\nu {}^*F^{\mu\nu} = 0$, where

$$\omega \equiv -k_\mu \overline{u}^\mu \tag{4.9}$$

(chosen so that ω is positive) is the frequency in the LFCR frame and is assumed to be nonzero.

(iv) $\omega B^\mu B_\mu = -\varepsilon^{\mu\nu\alpha\beta} B_\mu k_\nu \overline{u}_\alpha E_\beta$, which also follows from equation (4.8), $\omega B^\mu B_\mu + \varepsilon^{\mu\nu\alpha\beta} B_\mu k_\nu \overline{u}_\alpha E_\beta = B_\mu k_\nu {}^*F^{\mu\nu} = 0$.

Properties (i)-(iv) define B^μ in terms of k^μ, E^μ, and $\overline{u}^\mu$:

$$B^\mu = -\frac{1}{\omega} \varepsilon^{\mu\nu\alpha\beta} k_\nu \overline{u}_\alpha E_\beta \,. \tag{4.10}$$

Substituting equation (4.10) into equations (4.3) and (4.4) gives

$$F^{\mu\nu} = \frac{1}{\omega} \left(k^\mu E^\nu - E^\mu k^\nu \right) , \tag{4.11}$$

$${}^*F^{\mu\nu} = \frac{1}{\omega} \varepsilon^{\mu\nu\alpha\beta} \, k_\alpha \, E_\beta \,. \tag{4.12}$$

Inserting these back into Maxwell's equations and combining yields

$$\Omega^\mu{}_\nu E^\nu = 0 \,, \tag{4.13}$$

where

$$\Omega^\mu{}_\nu \equiv (k^\alpha k_\alpha \delta^\mu_\nu - k^\mu k_\nu - 4\pi i \omega \sigma^\mu{}_\nu) \tag{4.14}$$

defines the dispersion tensor.

Note that this is extremely general; all of the local physics is contained in the conductivity tensor. The expressions for the electromagnetic field tensor and its dual are for the radiation fields only. Hence, external fields appear only in the conductivity.

4.2 Ray Equations

Rays are well defined in the context of geometric optics. These are curves which are orthogonal at every point to the surfaces of constant phase (S). Given a relation in the form of equation (4.13) it is possible to explicitly construct these rays. This has been done in detail for Euclidean spaces (see, e.g., Weinberg, 1962). The generalization to a Riemannian space is straightforward and will be done in analogy with Weinberg (1962).

Consider the general case of an equation governing the dynamics of a field, Ψ, in space time in terms of a linear operator, $\mathbf{M}$,

$$\mathbf{M}\left(\nabla_\mu, x^\mu\right)\Psi = 0\,. \tag{4.15}$$

Expanding in a two length scale approximation, as in §2.1, gives to lowest order

$$\mathbf{M}\left(k_\mu, x^\mu\right)\Psi = 0\,. \tag{4.16}$$

This implies that $\det \mathbf{M}\left(k_\mu, x^\mu\right) = 0$ along the rays of the wave field. This provides a dispersion relation, $D\left(k_\mu, x^\mu\right)$, a scalar function of the wave four-vector and position that vanishes along the ray. If the eigenvalues of $\mathbf{M}$ are nondegenerate, then this also uniquely defines the polarization of Ψ.

The ray can now be explicitly constructed by employing the least action principle. The action can be explicitly constructed from the wave four-vector and the position by

$$S(\tau_1, \tau_2) = \int_{\tau_1}^{\tau_2} k_\mu \frac{dx^\mu}{d\tau} d\tau\,, \tag{4.17}$$

where τ is an affine parameter along the ray. Let Γ be the hypersurface of constant phase passing through the point $x^\mu\left(\tau_1\right)$. By definition, $k_\mu\left(\tau_1\right)$ is perpendicular to Γ. By varying $S\left(\tau_1, \tau_2\right)$ with respect to k_μ and x^μ, restricting $x^\mu\left(\tau_1\right)$ to lie on Γ, it is

possible to derive equations which define the ray,

$$\begin{aligned}\delta S &= \int_{\tau_1}^{\tau_2} \left[\frac{dk_\mu}{dx^\nu}\,\delta x^\nu \frac{dx^\mu}{d\tau} + k_\mu\,\delta\!\left(\frac{dx^\mu}{d\tau}\right)\right] d\tau \\ &= \int_{\tau_1}^{\tau_2} \left[\frac{dk_\mu}{dx^\nu}\frac{dx^\mu}{d\tau} - \frac{dk_\mu}{d\tau}\frac{dx^\mu}{dx^\nu}\right] \delta x^\nu d\tau + k_\mu\,\delta x^\mu\Big|_{\tau_1}^{\tau_2}.\end{aligned} \tag{4.18}$$

Because $x^\mu(\tau_1)$ is restricted to lie upon Γ, $k_\mu \delta x^\mu\big|_{\tau_1} = 0$. Because at τ_2 it is necessary for $k_\mu(\tau_2) = \nabla_\mu S \rightarrow \delta S = k_\mu(\tau_2)\,\delta x^\mu(\tau_2)$. These imply that the integral must vanish for arbitrary variations. This will be generally true if there exists a scalar function $D(k_\mu, x^\mu)$ such that

$$\frac{dx^\mu}{d\tau} = \left(\frac{\partial D}{\partial k_\mu}\right)_{x^\mu} \quad \text{and} \quad \frac{dk_\mu}{d\tau} = -\left(\frac{\partial D}{\partial x^\mu}\right)_{k_\mu}, \tag{4.19}$$

and hence,

$$\begin{aligned}\frac{dk_\mu}{dx^\nu}\frac{dx^\mu}{d\tau} - \frac{dk_\mu}{d\tau}\frac{dx^\mu}{dx^\nu} &= \left(\frac{\partial D}{\partial k_\mu}\right)_{x^\mu}\frac{dk_\mu}{dx^\nu} + \left(\frac{\partial D}{\partial x^\mu}\right)_{k_\mu}\frac{dx^\mu}{dx^\nu} \\ &= \frac{dD}{d\tau}\frac{d\tau}{dx^\nu} = 0\,,\end{aligned}$$

where the final equality follows from the fact that D is constant along the path (namely $D(k_\mu, x^\mu) = 0$). Therefore, equations (4.19) can be used to construct a ray given initial conditions and a dispersion relation. These are covariant analogues of Hamilton's equations. Note that the affine parameterization depends upon the particular form of the dispersion relation. For example, from $D'(k_\mu, x^\mu) \equiv f(k_\mu, x^\mu)\,D(k_\mu, x^\mu)$ it is possible to construct the rays associated with $D = 0$, with the affine parameters related by $d\tau' = d\tau/f$: i.e.,

$$\begin{aligned}\frac{dx^\mu}{d\tau'} &= \left(\frac{\partial D'}{\partial k_\mu}\right)_{x^\mu} \\ &= f\left(\frac{\partial D}{\partial k_\mu}\right)_{x^\mu} + D\left(\frac{\partial f}{\partial k_\mu}\right)_{x^\mu} \\ &= f\frac{dx^\mu}{d\tau}\,,\end{aligned} \tag{4.20}$$

and similarly for k_μ. Hence, any convenient affine parameterization can be selected by employing the appropriate function f.

While this derivation is done in some generality, here $\mathbf{M} = \Omega^\mu{}_\nu$ and $\Psi = E^\mu$.

4.3 Ohm's Law for Cold Plasmas

At this point it is necessary to determine an explicit form for the conductivity tensor $\sigma^\mu{}_\nu$. For cold plasmas this can be obtained via dynamical arguments. Three assumptions are made in the derivations below; (*i*) the equations of motion of the electrons are well approximated by the lowest-order perturbations, (*ii*) the motions of the electrons are nonrelativistic, and (*iii*) the electrons execute motions over a small enough region of space that all other forces may be considered constant. Assumptions (*i*) and (*ii*) are often employed in standard plasma physics. Assumption (*iii*) will generally be true as long as the geometric optics approximation holds.

4.3.1 Isotropic Cold Electron Plasma

This is considered as an example and a zero-field limit of the case where a constant external magnetic field is applied (cf. Dendy, 1990).

It is useful to introduce an order parameter (ϵ) to linearize the force equations. All field quantities are clearly of first order. In addition, the change in the velocity of the charged particles is of first order ($\delta u^\mu \equiv u^\mu - \overline{u}^\mu \propto \epsilon \exp(iS)$). Then, the electromagnetic force upon a single electron is given by

$$\begin{aligned} \mathcal{F}^\mu_{\rm EM} &= F^{\mu\nu} e u_\nu \\ &= e\overline{u}^\mu \epsilon E^\nu u_\nu - e\epsilon E^\mu \overline{u}^\nu u_\nu + e\varepsilon^{\mu\nu\alpha\beta}\, \overline{u}_\alpha\, \epsilon B_\beta u_\nu \,. \end{aligned} \tag{4.21}$$

In the first and third terms only the deviation from $\overline{u}^\mu$ contributes, thus they are of order ϵ^2. In the second term $\overline{u}^\mu u_\mu = -1 + \mathcal{O}(\epsilon)$ hence there is a first-order contribution, and $\mathcal{F}^\mu_{\rm EM} = eE^\mu$. The force is related to u^μ to first order in ϵ by $\mathcal{F}^\mu_{\rm EM} = -i\omega m\ \delta u^\mu$. The current is related to δu^μ by $J^\mu = e n_e\, \delta u^\mu$. Therefore, the conductivity tensor is

given by

$$\sigma^{\mu}{}_{\nu} = -\frac{\omega_P^2}{4\pi i\omega}\delta^{\mu}_{\nu}\,, \tag{4.22}$$

where $\omega_P \equiv \sqrt{4\pi e^2 n_e/m}$ is the plasma frequency.

4.3.2 Magnetoactive Cold Electron Plasma

In the presence of an externally generated magnetic field, $\mathcal{B}^{\mu}$, (defined in the LFCR frame in the same way as B^{μ}), the electromagnetic force upon a single electron is

$$\begin{aligned}\mathcal{F}^{\mu}_{\rm EM} &= F^{\mu\nu}eu_{\nu} \\ &= e\overline{u}^{\mu}\epsilon E^{\nu}u_{\nu} - e\epsilon E^{\mu}\overline{u}^{\nu}u_{\nu} + e\varepsilon^{\mu\nu\alpha\beta}\,\overline{u}_{\alpha}\,(\epsilon B_{\beta} + \mathcal{B}_{\beta})\,u_{\nu}\,.\end{aligned} \tag{4.23}$$

In contrast to equation (4.21), there is a first-order contribution from the third term in this case. Hence, to first order $\mathcal{F}^{\mu}_{\rm EM} = eE^{\mu} + e\varepsilon^{\mu\nu\alpha\beta}\,\overline{u}_{\alpha}\,\mathcal{B}_{\beta}\,u_{\nu}$. It is useful to decompose δu^{μ} and E^{μ} into temporal, and spatial components along and orthogonal to $\mathcal{B}^{\mu}$:

$$\begin{gathered}\delta u^{\mu}_{t} \equiv (\delta u_{\nu}\,\overline{u}^{\nu})\,\overline{u}^{\mu} \quad , \quad \delta u^{\mu}_{\parallel} \equiv \left(\frac{\mathcal{B}^{\nu}\delta u_{\nu}}{\mathcal{B}^{\alpha}\mathcal{B}_{\alpha}}\right)\mathcal{B}^{\mu}\,, \\ \delta u^{\mu}_{\perp} \equiv \delta u^{\mu} - \delta u^{\mu}_{t} - \delta u^{\mu}_{\parallel}\,,\end{gathered} \tag{4.24}$$

$$E^{\mu}_{\parallel} = \left(\frac{\mathcal{B}^{\nu}E_{\nu}}{\mathcal{B}^{\alpha}\mathcal{B}_{\alpha}}\right)\mathcal{B}^{\mu} \quad , \quad E^{\mu}_{\perp} = E^{\mu} - E^{\mu}_{\parallel}\,. \tag{4.25}$$

With these new definitions it is simple to show that the force equation separates into

$$\begin{aligned}-i\omega\delta u^{\mu}_{t} &= 0\,, \\ -i\omega\delta u^{\mu}_{\parallel} &= \frac{e}{m}E^{\mu}_{\parallel}\,, \\ -i\omega\delta u^{\mu}_{\perp} &= \frac{e}{m}E^{\mu}_{\perp} + \frac{e}{m}\varepsilon^{\mu\nu\alpha\beta}\,\overline{u}_{\alpha}\,\mathcal{B}_{\beta}\,\delta u_{\perp\,\nu}\,.\end{aligned} \tag{4.26}$$

Clearly $J^\mu_\parallel = -\,(\omega_P^2/4\pi i\omega)\,E^\mu_\parallel$. The perpendicular component may be determined by taking a second proper time derivative whence, to lowest order,

$$\begin{aligned} -\omega^2\delta u^\mu_\perp &= -\,i\omega\frac{e}{m}E^\mu_\perp \\ &\quad + \frac{e}{m}\varepsilon^{\mu\nu\alpha\beta}\,\overline{u}_\alpha\,\mathcal{B}_\beta\left(\frac{e}{m}E_{\perp\,\nu} + \frac{e}{m}\varepsilon_{\nu\gamma\sigma\varepsilon}\,\overline{u}^\sigma\mathcal{B}^\varepsilon\delta u^\gamma_\perp\right) \\ &= -\,i\omega\frac{e}{m}E^\mu_\perp + \left(\frac{e}{m}\right)^2\varepsilon^{\mu\nu\alpha\beta}\,\overline{u}_\alpha\,\mathcal{B}_\beta\,E_{\perp\,\nu} \\ &\quad - \left(\frac{e}{m}\right)^2\mathcal{B}^\nu\mathcal{B}_\nu\,\delta u^\mu_\perp\,. \end{aligned} \tag{4.27}$$

Defining $\omega_B^2 \equiv (e/m)^2\mathcal{B}^\mu\mathcal{B}_\mu$ and solving for $J^\mu_\perp = en_e\,\delta u^\mu_\perp$ gives

$$\delta u^\mu_\perp = \frac{\omega_P^2}{4\pi\,(\omega_B^2-\omega^2)}\Big(-i\omega g^{\mu\nu} + \frac{e}{m}\varepsilon^{\mu\nu\alpha\beta}\,\overline{u}_\alpha\,\mathcal{B}_\beta\Big)E_{\perp\,\nu}\,. \tag{4.28}$$

After substituting in the expressions for $E^\mu_\parallel$ and $E^\mu_\perp$ the total current is given by

$$J^\mu = J^\mu_\parallel + J^\mu_\perp = -\frac{\omega_P^2}{4\pi i\omega\,(\omega_B^2-\omega^2)}\left(-\omega^2 g^{\mu\nu} + \omega_B^2\frac{\mathcal{B}^\nu\mathcal{B}^\mu}{\mathcal{B}^\alpha\mathcal{B}_\alpha} - i\omega\frac{e}{m}\varepsilon^{\mu\nu\alpha\beta}\,\overline{u}_\alpha\,\mathcal{B}_\beta\right)E_\nu\,. \tag{4.29}$$

As a result, the conductivity tensor can be identified as

$$\sigma_{\mu\nu} = -\frac{\omega_P^2}{4\pi i\omega\,(\omega_B^2-\omega^2)}\left(-\omega^2 g_{\mu\nu} + \omega_B^2\frac{\mathcal{B}_\nu\mathcal{B}_\mu}{\mathcal{B}^\alpha\mathcal{B}_\alpha} - i\omega\frac{e}{m}\varepsilon_{\mu\nu\alpha\beta}\,\overline{u}^\alpha\,\mathcal{B}^\beta\right). \tag{4.30}$$

In a flat space, the spatial components of this can be compared to the standard result (see, e.g., Boyd & Sanderson, 1969; Dendy, 1990).

4.4 Ohm's Law for Warm Plasmas

For AGN and X-ray binaries, accreting plasma near the central compact object will in general be hot. Even in low-luminosity AGN, accreting electrons can have γ's on the order of $10 - 10^3$ (see, e.g., Melia & Falcke, 2001; Narayan et al., 1998). In these environments assumption (*ii*) in Section 4.3, that the motions of the electrons are nonrelativistic, is no longer valid.

For warm plasmas, ones in which the thermal velocities of the electrons are significant compared to the phase velocities of the modes, it is possible to determine the conductivities using the Vlasov equation just as in flat space (see, e.g., Dendy, 1990; Boyd & Sanderson, 1969; Montgomery & Tidman, 1964):

$$u^\mu \left(\frac{\partial f}{\partial x^\mu}\right)_{p^\mu} + \mathcal{F}^\mu_{\rm EM} \left(\frac{\partial f}{\partial p^\mu}\right)_{x^\mu} = 0\,, \tag{4.31}$$

where p^μ and f are the momentum and distribution function of the electrons, respectively. The average plasma velocity, $\overline{u}^\mu$, must now be averaged over temperature in addition to the induced oscillations. Note that unlike the analyses of warm plasmas in flat space, this must now be done in a manifestly covariant way. At this point it is necessary to determine the form of the force, $\mathcal{F}^\mu_{\rm EM}$, under which the system is evolving.

4.4.1 Isotropic Warm Electron Plasma

In this case $\mathcal{F}^\mu_{\rm EM} = F^{\mu\nu} e u_\nu$. Hence expanding the distribution function in terms of the order parameter introduced in Section 4.3.1 to first order, $f = f_0 + \epsilon f_1 + \mathcal{O}(\epsilon^2)$, and inserting into equation (4.31) gives

$$u^\mu \left(\frac{\partial f_1}{\partial x^\mu}\right)_{p^\mu} + eF^{\mu\nu}u_\nu \left(\frac{\partial f_0}{\partial p^\mu}\right)_{x^\mu} = 0\,. \tag{4.32}$$

Considering the lowest order in the two length scale expansion of Section 4.1, this may now be solved for f_1:

$$f_1 = \frac{ieu_\nu}{u^\alpha k_\alpha} F^{\mu\nu} \left(\frac{\partial f_0}{\partial p^\mu}\right)_{x^\mu}\,, \tag{4.33}$$

which is the covariant analogue of the expressions found in the kinetic theory literature (see, e.g., Dendy, 1990).

Assuming that the plasma was originally charge neutral the current density is

related to the perturbation in the distribution function, f_1, by

$$J^\mu = e \int d^4p \, f_1 u^\mu \, .$$

Then, using equation (4.11) this may be written in terms of E^μ as

$$J^\mu = -\frac{ie^2}{\omega} k^\alpha E^\nu \int d^4p \frac{u^\mu}{u^\beta k_\beta} \left[u_\alpha \left(\frac{\partial f_0}{\partial p^\nu} \right)_{x^\mu} - u_\nu \left(\frac{\partial f_0}{\partial p^\alpha} \right)_{x^\mu} \right] . \tag{4.34}$$

From this it is clear that the conductivity tensor is

$$\sigma^\mu{}_\nu = -\frac{ie^2}{\omega m} k^\alpha \int d^4p \frac{p^\mu}{p^\beta k_\beta} \left[p_\alpha \left(\frac{\partial f_0}{\partial p^\nu} \right)_{x^\mu} - p_\nu \left(\frac{\partial f_0}{\partial p^\alpha} \right)_{x^\mu} \right] . \tag{4.35}$$

In order to make a connection with the expression derived in the previous section it is convenient to integrate this by parts,

$$\sigma_{\mu\nu} = \frac{ie^2}{\omega m} \int d^4p \left[g_{\mu\nu} - \frac{k_\mu p_\nu + k_\nu p_\mu}{p_\alpha k^\alpha} + \frac{k_\alpha k^\alpha p_\mu p_\nu}{(p_\beta k^\beta)^2} \right] f_0 \, , \tag{4.36}$$

where the boundary terms vanish by virtue of the convergence of $\int d^4p \, f_0$. For the cold plasma, $f_0 = n\delta^4(p^\mu - m\overline{u}^\mu)$, thus,

$$\sigma_{\mu\nu} = -\frac{\omega_P^2}{4\pi i\omega} \left(g_{\mu\nu} + \frac{k_\mu \overline{u}_\nu + k_\nu \overline{u}_\mu}{\omega} + \frac{k_\alpha k^\alpha \overline{u}_\mu \overline{u}_\nu}{\omega^2} \right) . \tag{4.37}$$

This differs from the result in Section 4.3.1 in two respects: terms proportional to $\overline{u}_\mu$ and the term proportional to k_μ. Because the conductivity enters Maxwell's equations only through a contraction with the electric four-vector, the former are superfluous. The latter represents the sonic mode which appears in the dynamical calculation of the conductivity only in the form of an infinite wavelength mode. For the two transverse electromagnetic modes ($E^\mu k_\mu = 0$) this does agree.

4.4.2 Magnetoactive Warm Electron Plasma

In the presence of an external magnetic field $\mathcal{F}^{\mu}_{\rm EM}$ has a zeroth-order contribution:

$$\mathcal{F}^{\mu}_{\rm EM} = eF^{\mu\nu}\,u_{\nu} + eF^{\mu\nu}_{\rm Ex}\,u_{\nu}\,, \tag{4.38}$$

where, in terms of the external magnetic field (again defined in the LFCR frame), $F^{\mu\nu}_{\rm Ex} \equiv \varepsilon^{\mu\nu\alpha\beta}\overline{u}_{\alpha}\mathcal{B}_{\beta}$, (cf. equation (4.3)). Expanding the Vlasov equation in the perturbation parameter ϵ to first order and in the two length scale expansion (Section 4.1) now gives

$$iu^{\mu}k_{\mu}f_1 + \frac{e}{m}F^{\mu\nu}_{\rm Ex}\,p_{\nu}\left(\frac{\partial f_1}{\partial p^{\mu}}\right)_{x^{\mu}} = -\frac{e}{m}F^{\mu\nu}p_{\nu}\left(\frac{\partial f_0}{\partial p^{\mu}}\right)_{x^{\mu}}\,. \tag{4.39}$$

At this point it is useful to introduce a function η defined implicitly by

$$\frac{d}{d\eta} = \frac{e}{m}F^{\mu\nu}_{\rm Ex}\,p_{\nu}\left(\frac{\partial}{\partial p^{\mu}}\right)_{x^{\mu}}\,. \tag{4.40}$$

(cf. Lifshitz & Pitaevskii, 1981; Krall & Trivelpiece, 1973). In terms of η, the electron momenta are determined by the equation

$$\frac{dp^{\mu}}{d\eta} = \frac{e}{m}F^{\mu\nu}_{\rm Ex}\,p_{\nu} = \frac{e}{m}\varepsilon^{\mu\nu\alpha\beta}\,\overline{u}_{\alpha}\mathcal{B}_{\beta}p_{\nu}\,. \tag{4.41}$$

As in the cold case, this may be reduced to a two-dimensional problem by an appropriate decomposition of the momentum:

$$p^{\mu}_{t} = (p_{\nu}\,\overline{u}^{\nu})\,\overline{u}^{\mu}\quad,\quad p^{\mu}_{\parallel} = \left(\frac{\mathcal{B}^{\nu}p_{\nu}}{\mathcal{B}^{\alpha}\mathcal{B}_{\alpha}}\right)\mathcal{B}^{\mu}\,,$$
$$p^{\mu}_{\perp} = p^{\mu} - p^{\mu}_{t} - p^{\mu}_{\parallel}\,, \tag{4.42}$$

In terms of these, the system of equations for p^μ reduce to

$$\begin{aligned} \frac{dp_t^\mu}{d\eta} &= 0\,, \\ \frac{dp_\parallel^\mu}{d\eta} &= 0\,, \\ \frac{dp_\perp^\mu}{d\eta} &= \frac{e}{m}\varepsilon^{\mu\nu\alpha\beta}\,\overline{u}_\alpha \mathcal{B}_\beta p_{\perp\,\nu}\,. \end{aligned} \tag{4.43}$$

This last equation is simply that governing cyclotron motion. Using the fact that $d/d\eta$ commutes with the metric (this is because the metric depends only upon x^μ and not p^μ) it may be rewritten as a pair of uncoupled, second-order ordinary differential equations:

$$\frac{d^2 p_\perp^\mu}{d\eta^2} + \omega_B^2 p_\perp^\mu = 0\,. \tag{4.44}$$

This has solutions

$$p_\perp^\mu = p_x^\mu \cos(\omega_B \eta + \phi_0) + p_y^\mu \sin(\omega_B \eta + \phi_0)\,, \tag{4.45}$$

where p_x^μ and p_y^μ are a pair of bases which span the space perpendicular to $\overline{u}^\mu$ and $\mathcal{B}^\mu$, and ϕ_0 is a phase factor. By inserting this solution into equation (4.41) and matching up trigonometric terms, p_y^μ can be found in terms of p_x^μ,

$$p_y^\mu = \frac{1}{\omega_B}\varepsilon^{\mu\nu\alpha\beta}\,\overline{u}_\alpha \mathcal{B}_\beta p_{x\,\beta}\,. \tag{4.46}$$

It is possible to now solve for η in terms of p^μ, p_x^μ, and ϕ_0:

$$\eta = \frac{1}{\omega_B}\left[\arctan\left(\frac{e\varepsilon_{\mu\nu\alpha\beta}p^\mu p_x^\nu \overline{u}^\alpha \mathcal{B}^\beta}{m\omega_B \underset{\xi}{p_x} p_\xi}\right) - \phi_0\right]\,. \tag{4.47}$$

Inserting $p^\mu(\eta)$ into f_1 and f_0 transform equation (4.39) into a first-order differential equation for f_1. This has solution

$$f_1 = \left(\mu^{-1}\int \mu\beta_\mu d\eta\right) E^\mu\,, \tag{4.48}$$

where

$$\beta_\mu \equiv \frac{e}{\omega m} k^\nu \left[p_\nu \left(\frac{\partial f_0}{\partial p^\mu} \right)_{x^\mu} - p_\mu \left(\frac{\partial f_0}{\partial p^\nu} \right)_{x^\mu} \right] , \tag{4.49}$$

$$\mu \equiv \exp\left(-i k_\mu \int \frac{p^\mu}{m} d\eta \right) . \tag{4.50}$$

The integral for μ may be rewritten in terms of p^μ by using equations (4.43) and (4.44),

$$\int \left(p_t^\mu + p_\parallel^\mu \right) d\eta = \left(p_t^\mu + p_\parallel^\mu \right) \eta \, , \tag{4.51}$$

$$\begin{aligned} \int p_\perp^\mu d\eta &= \frac{1}{\omega_B^2} \int \frac{d^2 p_\perp^\mu}{d\eta^2} = \frac{1}{\omega_B^2} \frac{dp_\perp^\mu}{d\eta} \\ &= \frac{1}{\omega_B^2} \varepsilon^{\mu\nu\alpha\beta} \, \overline{u}_\alpha \mathcal{B}_\beta p_{\perp\,\nu} \, . \end{aligned} \tag{4.52}$$

Thus,

$$\mu = \exp\left\{ i \left[\left(\omega \overline{u}_\mu - \frac{\mathcal{B}^\nu k_\nu}{\mathcal{B}_\alpha \mathcal{B}^\alpha} \mathcal{B}_\mu \right) \eta - \frac{1}{\omega_B^2} \varepsilon_{\mu\nu\alpha\beta} \, k^\nu \overline{u}^\alpha \mathcal{B}^\beta \right] \frac{p^\mu}{m} \right\} . \tag{4.53}$$

With equation (4.45) this may be treated as a function of η, while with equation (4.47) this may be treated as a function of p^μ.

As in the previous case, the current four-vector is then found by integrating over the momentum portion of the phase space. This gives the conductivity tensor to be

$$\sigma^\mu{}_\nu = -\frac{e}{m} \int d^4 p \, p^\mu \left[\mu^{-1} \int \mu \beta_\nu d\eta \right] (p^\mu) \, , \tag{4.54}$$

where it has been emphasized that the interior integral is to be treated as a function of the momenta.

4.4.3 Conductivity in Quasi-Longitudinal Approximation

In general, the integrals over η in equation (4.54) can be evaluated in terms of sums of Bessel functions in an analogous fashion to that typically done for the nonrelativistic case (see, e.g., Krall & Trivelpiece, 1973). Nonetheless, this can be significantly

simplified by considering the case where (i) f_0 is a function of $\mathcal{P}^2 \equiv p^\mu p_\mu$ and $\epsilon \equiv p^\mu \overline{u}_\mu$ only (typically f_0 can be written in the form $f(\epsilon)\delta(\mathcal{P}^2 + m^2)$ where the delta function is required to place the distribution on the mass-shell), (ii) $\varepsilon^{\mu\nu\alpha\beta}\,\overline{u}_\alpha \mathcal{B}_\beta k_\mu = 0$ (i.e., the quasi-longitudinal approximation), (iii) $\omega_B \ll \omega$, and (iv) f_0 is such that $p^\mu \overline{u}_\mu / m - 1 \ll 1$ (i.e., cool, not hot).

Assumption (i) simplifies β_μ,

$$\beta^\mu = \frac{e}{m\omega}\frac{\partial f_0}{\partial \epsilon} k_\nu \left(\overline{u}^\mu p^\nu - \overline{u}^\nu p^\mu\right) . \tag{4.55}$$

Note that because ϵ is independent of η, the terms involving f_0 can now be brought out of the innermost integral in equation (4.54). Assumption (ii) gives that $k_\mu p_\perp^\mu = 0$ and hence,

$$\mu = \mathrm{e}^{i\varpi\eta} , \tag{4.56}$$

where $\varpi \equiv k^\mu p_\mu / m$. Therefore, the two integrals that must be done are

$$\int p_\parallel^\mu \mathrm{e}^{i\varpi\eta} d\eta = p_\parallel^\mu \frac{\mu}{i\varpi} , \tag{4.57}$$

and

$$\int p_\perp^\mu \mathrm{e}^{i\varpi\eta} d\eta = \left(g^{\mu\nu} - \frac{e}{i\varpi m}\varepsilon^{\mu\nu\alpha\beta}\,\overline{u}_\alpha \mathcal{B}_\beta\right) p_{\perp\,\nu} \frac{\varpi^2}{\varpi^2 - \omega_B^2}\frac{\mu}{i\varpi} . \tag{4.58}$$

Therefore, in the quasi-longitudinal approximation,

$$f_1 = \frac{e}{i\varpi m}\frac{\partial f_0}{\partial \epsilon}\frac{1}{\varpi^2 - \omega_B^2}\left[\varpi^2 g_{\mu\nu} - \omega_B^2 \frac{\mathcal{B}_\mu \mathcal{B}_\nu}{\mathcal{B}^\alpha \mathcal{B}_\alpha} + \frac{i\varpi e}{m}\varepsilon_{\mu\nu\alpha\beta}\overline{u}^\alpha \mathcal{B}^\beta\right] p^\nu E^\mu , \tag{4.59}$$

where the definitions of $p_\parallel^\mu$, $p_\perp^\mu$, and E^μ were used. In the quasi-longitudinal approximation, E^μ is orthogonal to the external magnetic field, $\mathcal{B}^\mu$. As a result, the there are only two integrals that must be done in order to find the conductivity tensor:

$$\begin{aligned} I_1^{\mu\nu} &= -\frac{i\omega}{m}\int d^4p \frac{i\varpi}{\varpi^2 - \omega_B^2} p^\mu p^\nu \frac{\partial f_0}{\partial \epsilon} \\ I_2^{\mu\nu} &= -\frac{i\omega}{m}\int d^4p \frac{1}{\varpi^2 - \omega_B^2} p^\mu p^\nu \frac{\partial f_0}{\partial \epsilon} . \end{aligned} \tag{4.60}$$

In terms of these, the conductivity is

$$\sigma^{\mu}{}_{\nu} = -\frac{e^2}{i\omega m}\left(I_1^{\mu\gamma}g_{\gamma\nu} - \frac{e}{m}I_2^{\mu\gamma}\varepsilon_{\nu\gamma\alpha\beta}\overline{u}^{\alpha}\mathcal{B}^{\beta}\right). \tag{4.61}$$

From equation (4.55) it follows that

$$p_\mu p_\nu \frac{\partial f_0}{\partial \epsilon} = \frac{p_\mu k^\alpha}{\omega}\left(p_\alpha \frac{\partial f_0}{\partial p^\nu} - p_\nu \frac{\partial f_0}{\partial p^\alpha}\right) - \frac{k^\alpha p_\alpha}{\omega} p_\mu \overline{u}_\nu \frac{\partial f_0}{\partial \epsilon}. \tag{4.62}$$

Noting that the $I^{\mu\nu}$ will only be contracted on the second index with terms orthogonal to $\overline{u}^\mu$ (for $I_1^{\mu\nu}$ this is the electric field), the $I^{\mu\nu}$ are given by

$$\begin{aligned} I_1^{\mu\nu} &= -i\int d^4p \frac{i\varpi}{\varpi^2-\omega_B^2} p^\mu \left(\varpi g^{\nu\alpha} - \frac{p^\nu k^\alpha}{m}\right)\frac{\partial f_0}{\partial p^\alpha} \\ I_2^{\mu\nu} &= -\frac{i}{m}\int d^4p \frac{1}{\varpi^2-\omega_B^2} p^\mu \left(\varpi g^{\nu\alpha} - p^\nu k^\alpha\right)\frac{\partial f_0}{\partial p^\alpha}. \end{aligned} \tag{4.63}$$

Because there is already a term linear in ω_B in equation (4.61), to lowest order in assumption (*iii*) ω_B^2 may be neglected in the $I^{\mu\nu}$. Thus,

$$\begin{aligned} I_1^{\mu\nu} &= \int d^4p\, p^\mu \left(g^{\nu\alpha} - \frac{p^\nu k^\alpha}{m\varpi}\right)\frac{\partial f_0}{\partial p^\alpha} \\ I_2^{\mu\nu} &= -i\int d^4p \frac{p^\mu}{\varpi}\left(g^{\nu\alpha} - \frac{p^\nu k^\alpha}{m\varpi}\right)\frac{\partial f_0}{\partial p^\alpha}. \end{aligned} \tag{4.64}$$

These may be integrated by parts to produce

$$\begin{aligned} I_1^{\mu\nu} &= -\int d^4p\, f_0 \left(g^{\mu\nu} - \frac{p^\mu k^\nu + p^\nu k^\mu}{m\varpi} + \frac{p^\mu p^\nu}{m^2\varpi^2}k^\alpha k_\alpha\right) \\ I_2^{\mu\nu} &= i\int d^4p \frac{f_0}{\varpi}\left(g^{\mu\nu} - \frac{2p^\mu k^\nu + p^\nu k^\mu}{m\varpi} + 2\frac{p^\mu p^\nu}{m^2\varpi^2}k^\alpha k_\alpha\right). \end{aligned} \tag{4.65}$$

Note that in this case, $I_1^{\mu\nu}$ is simply the integral that had to be done for the warm isotropic plasma (cf.equation (4.36)).

Assumption (*iv*) enters by expanding ϖ about ω. Define $\wp^2 \equiv \epsilon^2 - m^2$, i.e., $\wp$ is the magnitude of the spatial components of the momentum in the LFCR frame.

Then, to second order in $\wp$,

$$\varpi^j \simeq (-\omega)^j \left[1 - j\left(\frac{p^\mu \mathcal{B}_\mu k^\nu \mathcal{B}_\nu}{m\omega \mathcal{B}^\alpha \mathcal{B}_\alpha}\right) + \frac{j(j-1)}{2}\left(\frac{p^\mu \mathcal{B}_\mu k^\nu \mathcal{B}_\nu}{m\omega \mathcal{B}^\alpha \mathcal{B}_\alpha}\right)^2 + j\frac{\wp^2}{2m^2}\right] . \tag{4.66}$$

Thus,

$$\begin{aligned} I_1^{\mu\nu} &\simeq -\int d^4p\, f_0 \left(g^{\mu\nu} + \frac{p^\mu p^\nu}{m^2}\frac{k^\alpha k_\alpha}{\omega^2}\right) \\ I_2^{\mu\nu} &\simeq -i\int d^4p\, \frac{f_0}{\omega}\left\{\left[1 - \frac{\wp^2}{2m^2} + \left(\frac{p^\mu \mathcal{B}_\mu k^\nu \mathcal{B}_\nu}{m\omega \mathcal{B}^\alpha \mathcal{B}_\alpha}\right)^2\right] g^{\mu\nu} + 2\frac{p^\mu p^\nu}{m^2}\frac{k^\alpha k_\alpha}{\omega^2}\right\}, \end{aligned} \tag{4.67}$$

where terms odd in p^μ and terms $\propto k^\nu$ have been dropped. The former is due to the fact that f_0 has been chosen to be an isotropic function of the spatial components of the momentum in the LFCR frame and hence any odd terms will vanish upon integration. The latter is allowed because, as stated earlier, these will only have significance when contracted with terms orthogonal to k^μ (for $I_2^{\mu\nu}$ this is results from the quasi-longitudinal approximation in which k^μ can be written in terms of $\overline{u}^\mu$ and $\mathcal{B}^\mu$ only). From symmetry it is clear that

$$\int d^4p\, f_0 \frac{\left(p^\mu \mathcal{B}_\mu\right)^2}{\mathcal{B}^\alpha \mathcal{B}_\alpha} = \frac{1}{3} n_e m^2 \left\langle f_0 \right\rangle_2 , \tag{4.68}$$

where

$$\left\langle f_0 \right\rangle_2 \equiv \frac{1}{n_e m^2}\int d^4p\, f_0 \wp^2 . \tag{4.69}$$

In addition, the off-diagonal components of the integrals over $p^\mu p^\nu$ will vanish due to the symmetry of f_0. Because adding terms $\propto \overline{u}^\nu$ will not alter the physical solutions, it is possible to replace $\int d^4p\, p^\mu p^\nu f_0$ with $\frac{1}{3} n_e m^2 \left\langle f_0 \right\rangle_2 g^{\mu\nu}$. Lastly, note that

$$\frac{\left(k^\nu \mathcal{B}_\nu\right)^2}{\mathcal{B}^\alpha \mathcal{B}_\alpha} = \omega^2 + k^\alpha k_\alpha . \tag{4.70}$$

Therefore, the $I^{\mu\nu}$ are given by

$$I_1^{\mu\nu} \simeq n_e \mathcal{I}_1 g^{\mu\nu} \quad \text{and} \quad I_2^{\mu\nu} \simeq \frac{n_e}{i\omega} \mathcal{I}_2 g^{\mu\nu} \,, \tag{4.71}$$

where

$$\begin{aligned} \mathcal{I}_1 &\equiv 1 + \frac{1}{3} \frac{k^\alpha k_\alpha}{\omega^2} \langle f_0 \rangle_2 \\ \mathcal{I}_2 &\equiv 1 - \frac{1}{6} \langle f_0 \rangle_2 + \frac{k^\alpha k_\alpha}{\omega^2} \langle f_0 \rangle_2 \,. \end{aligned} \tag{4.72}$$

Because the terms multiplying $\mathcal{I}_2$ in the conductivity are already of first order (the order of ω_B is necessarily equal to or smaller than that of $\wp$ for the approximations thus far to hold), to second order in small quantities in the conductivity, $\mathcal{I}_2 \simeq 1$. As a result, with the lowest-order finite temperature corrections the conductivity is given by

$$\sigma_{\mu\nu} \simeq -\frac{\omega_P^2}{4\pi i\omega} \left(\mathcal{I}_1 g_{\mu\nu} - \frac{e}{i\omega m} \varepsilon_{\mu\nu\alpha\beta} \overline{u}^\alpha \mathcal{B}^\beta \right) \tag{4.73}$$

For the cold plasma $\mathcal{I}_1 = 1$ and this does reduce to the appropriate expansion of the conductivity derived in Section 4.3.2.

4.5 Dispersion Relations

Given the conductivities derived in Section 4.3 & Section 4.4 it is now possible to obtain the associated dispersion relations. It is instructive to compare these to the dispersion relation for massive particles (de Broglie waves):

$$D(k_\mu, x^\mu) = k^\mu k_\mu + m^2 \,. \tag{4.74}$$

That this does produce the time-like geodesics when inserted into the ray equations is demonstrated in Appendix A.

4.5.1 Isotropic Electron Plasma

The conductivity tensor obtained in Section 4.3.1 for the isotropic cold electron plasma yields the dispersion tensor

$$\Omega^{\mu}{}_{\nu} = \left(k^{\alpha}k_{\alpha} + \omega_P^2\right)\delta^{\mu}_{\nu} - k^{\mu}k_{\nu}\,. \tag{4.75}$$

For the transverse modes, this gives the dispersion relation

$$D(k_{\mu}, x^{\mu}) = k^{\mu}k_{\mu} + \omega_P^2\,, \tag{4.76}$$

(cf. Kulsrud & Loeb, 1992). For constant density plasmas this is nothing more than the massive particle equation, cf. equation (4.74). For plasmas with spatially varying densities this leads to a variable effective "mass". Hence in general, photons in plasmas will not follow geodesics. This is a representation of the refractive nature of the plasma.

4.5.2 Quasi-Longitudinal Approximation for the Cold Electron Plasma

When magnetic fields are present it is necessary to utilize the conductivity tensor obtained in Section 4.3.2. In the quasi-longitudinal approximation the wave three-vector is parallel to the external magnetic field in the LFCR. In this approximation, the modes are transverse. This follows from the fact that in the LFCR frame this is true and that since this is a local property expressible in covariant form, it must also be true in an arbitrary frame. This can be explicitly verified by comparison with the results of Section 4.5.5 where the general case is considered.

Under these conditions the dispersion tensor takes the form

$$\Omega^{\mu}{}_{\nu} = \alpha\delta^{\mu}_{\nu} - i\gamma M^{\mu}{}_{\nu}\,, \tag{4.77}$$

where α, γ, and $M_{\mu\nu}$ are defined by

$$\alpha \equiv k^\mu k_\mu - \delta\omega^2\,, \quad \gamma \equiv \delta\omega\left(\frac{e}{m}\right)\,, \tag{4.78}$$
$$\delta \equiv \frac{\omega_P^2}{\omega_B^2 - \omega^2}\,, \quad M_{\mu\nu} = -M_{\nu\mu} \equiv \varepsilon_{\mu\nu\alpha\beta}\,\overline{u}^\alpha \mathcal{B}^\beta\,.$$

Taking the determinant of $\Omega^\mu{}_\nu$ yields

$$\begin{aligned}\det \Omega^\mu{}_\nu &= \alpha^4 - \alpha^2\gamma^2 \mathcal{B}^\mu \mathcal{B}_\mu \\ &= \alpha^2\left(\alpha - \delta\omega\omega_B\right)\left(\alpha + \delta\omega\omega_B\right) = 0\,.\end{aligned} \tag{4.79}$$

The two modes corresponding to $\alpha = 0$ are the sonic mode and the unphysical mode proportional to $\overline{u}^\mu$ which is eliminated by the condition that $\overline{u}_\mu E^\mu = 0$. The other two modes have dispersion relations

$$\begin{aligned}D\left(k_\mu, x^\mu\right) &= \alpha \pm \delta\omega\omega_B \\ &= k^\mu k_\mu + \frac{\omega\omega_P^2}{\omega \pm \omega_B}\,.\end{aligned} \tag{4.80}$$

As with equation (4.76), this dispersion relation also has a term that could be identified with the mass in equation (4.74). In contrast with equation (4.76), now that "mass" depends upon the polarization eigenmode. As a result, different eigenmodes will propagate differently. This is an expression of the dispersive nature of a magnetized plasma.

In addition to dispersion, a noticeable departure from its nonrelativistic analogue is the presence of k_μ in the definition of ω (equation (4.9)). This is not surprising since it is the most general Lorentz covariant extension of the quasi-longitudinal dispersion relation. Of interest is the fact that the dispersion relation is now cubic in the magnitude of $\vec{k}$, κ. Because two roots clearly exist in the low-density limit, a third root must also exist. This results in a new branch in the dispersion relation. This will be explored in more detail in Section 6.1.

4.5.3 Quasi-Longitudinal Approximation for the Warm Electron Plasma

For the conductivity derived in Section 4.4.3, this is identical to the previous section, where α and δ, are replaced by $k^\mu k_\mu + \mathcal{I}_1\omega_P^2$ and $-\omega_P^2/\omega^2$. Then,

$$\begin{aligned} D\left(k_\mu, x^\mu\right) &= \alpha \pm \omega_P^2 \frac{\omega_B}{\omega} \\ &= k^\mu k_\mu + \mathcal{I}_1\omega_P^2 \pm \omega_P^2 \frac{\omega_B}{\omega} \\ &= \left(1 + \frac{1}{3}\frac{\omega_P^2}{\omega^2}\left\langle f_0\right\rangle_2\right) k^\mu k_\mu + \omega_P^2 \pm \omega_P^2 \frac{\omega_B}{\omega}\,. \end{aligned} \tag{4.81}$$

For a thermal electron distribution, $\left\langle f_0\right\rangle_2 = 3kT/m$ and hence

$$\frac{1}{3}\frac{\omega_P^2}{\omega^2}\left\langle f_0\right\rangle_2 = \frac{\omega_T^2}{\omega^2} \quad \text{where} \quad \omega_T^2 = \frac{kT}{m}\omega_P^2\,. \tag{4.82}$$

Note that ω_T is related to the Debye frequency, ω_D, by $\omega_T = \omega_P^2/\omega_D$. Thus, including the lowest order finite temperature corrections, the dispersion relation in the quasi-longitudinal approximation is

$$D\left(k_\mu, x^\mu\right) = \left(1 + \frac{\omega_T^2}{\omega^2}\right) k^\mu k_\mu + \omega_P^2 \pm \omega_P^2 \frac{\omega_B}{\omega}\,. \tag{4.83}$$

4.5.4 General Magnetoactive Cold Pair Plasma

The conductivity for the pair plasma may be obtained by adding the conductivities for the electrons and the positrons,

$$\begin{aligned} \sigma_{\mu\nu}^{\text{pair}} &= \sigma_{\mu\nu}^{e^-} + \sigma_{\mu\nu}^{e^+} \\ &= -\frac{\omega_P^2}{4\pi i\omega\left(\omega_B^2 - \omega^2\right)}\left(-\omega^2 g_{\mu\nu} + \omega_B^2 \frac{\mathcal{B}_\nu \mathcal{B}_\mu}{\mathcal{B}^\alpha \mathcal{B}_\alpha}\right)\,, \end{aligned} \tag{4.84}$$

where now the plasma frequency is defined in terms of the sum of the number densities of the electrons and positrons. The resulting dispersion tensor is

$$\Omega_{\mu\nu} = \alpha g_{\mu\nu} - k_\mu k_\nu + \beta \mathcal{B}_\mu \mathcal{B}_\nu \,, \tag{4.85}$$

where α, γ, δ, and $M_{\mu\nu}$ are defined as in equation (4.78), and $\beta \equiv \delta(e/m)^2$. In addition to the requirement that $\Omega^\mu{}_\nu E^\nu = 0$, E^μ must be orthogonal to $\overline{u}^\mu$. As a result, it is necessary to alter $\Omega^\mu{}_\nu$ in such a way that it explicitly separates the eigenmodes orthogonal to $\overline{u}^\mu$ from the unphysical mode. This can be trivially accomplished by adding a term $-\omega k_\mu \overline{u}_\nu$ to the dispersion tensor. Note that this does not change the dispersion equation for the physical modes because $E^\mu \overline{u}_\mu = 0$ by definition. Thus, consider

$$\Omega_{\mu\nu} = \alpha g_{\mu\nu} - k_\mu \left(k_\nu - \omega \overline{u}_\nu\right) + \beta \mathcal{B}_\mu \mathcal{B}_\nu \,, \tag{4.86}$$

instead of the dispersion tensor given in equation (4.85). For this dispersion tensor, the unphysical mode is trivially found to be $\overline{u}^\mu$, with dispersion relation $D = \alpha$. As in Section 4.5.2 the dispersion relations can be found by taking the determinant of the dispersion tensor:

$$\det \Omega^\mu{}_\nu = -(1+\delta)\omega^2 \alpha^2 \left[\alpha + \delta\omega_B^2 - \frac{\delta}{1+\delta}\left(\frac{e\mathcal{B}^\mu k_\mu}{m\omega}\right)^2\right], \tag{4.87}$$

where the definition of α was used. Therefore, the dispersion relations for the two electromagnetic modes are

$$\begin{aligned} D_1\left(k_\mu, x^\mu\right) &= k^\mu k_\mu - \frac{\omega_P^2}{\omega_B^2 - \omega^2} \\ D_2\left(k_\mu, x^\mu\right) &= k^\mu k_\mu + \omega_P^2 - \frac{\omega_P^2}{\omega_P^2 + \omega_B^2 - \omega^2}\left(\frac{e\mathcal{B}^\mu k_\mu}{m\omega}\right)^2 . \end{aligned} \tag{4.88}$$

It is straightforward to show that D_1 and D_2 correspond to the extraordinary and ordinary modes, respectively, by considering the transverse limit ($\mathcal{B}^\mu k_\mu = 0$).

4.5.5 General Magnetoactive Cold Electron Plasma

For the general case, no approximations, except those used to derive equations (4.13) and (4.30), are made. In this case, inserting the conductivity tensor obtained in Section 4.3.2 into equation (4.14) gives

$$\Omega_{\mu\nu} = k^\alpha k_\alpha g_{\mu\nu} - k_\mu k_\nu - \frac{\omega_P^2}{(\omega_B^2 - \omega^2)}\left(\omega^2 g_{\mu\nu} - \omega_B^2 \frac{\mathcal{B}_\mu \mathcal{B}_\nu}{\mathcal{B}^\alpha \mathcal{B}_\alpha} + i\omega \frac{e}{m} \varepsilon_{\mu\nu\alpha\beta}\, \overline{u}^\alpha\, \mathcal{B}^\beta\right). \quad (4.89)$$

Collecting the coefficients of like tensors gives

$$\Omega^\mu{}_\nu = \alpha \delta^\mu{}_\nu - k^\mu k_\nu + \beta \mathcal{B}^\mu \mathcal{B}_\nu - i\gamma M^\mu{}_\nu\,, \quad (4.90)$$

where α, β, γ, δ, and $M_{\mu\nu}$ are defined as in Section 4.5.2 and Section 4.5.4. As in the previous section, it is useful to add a term proportional to $\overline{u}_\nu E^\nu$ to the dispersion equation. Hence consider

$$\Omega^\mu{}_\nu = \alpha \delta^\mu_\nu - k^\mu \left(k_\nu - \omega \overline{u}_\nu\right) + \beta \mathcal{B}^\mu \mathcal{B}_\nu - i\gamma M^\mu{}_\nu\,. \quad (4.91)$$

Proceeding as in the previous sections, the scalar dispersion relations corresponding to the different eigenmodes can be found by considering the determinant of the dispersion tensor:

$$\begin{aligned}\det \Omega^\mu{}_\nu = \alpha \Big\{ & \alpha^3 + \left[\beta \mathcal{B}^\mu \mathcal{B}_\mu - \left(k^\mu k_\mu + \omega^2\right)\right] \alpha^2 \\ & - \left[\delta \omega_B^2 \left(k^\mu k_\mu + \omega^2\right) - \delta \left(\frac{e}{m} \mathcal{B}^\mu k_\mu\right)^2 + \delta^2 \omega^2 \omega_B^2\right] \alpha \\ & - \delta^2 \omega^2 \left[\delta \omega_B^4 - \left(\frac{e}{m} \mathcal{B}^\mu k_\mu\right)^2\right] \Big\}. \quad (4.92)\end{aligned}$$

Inserting the definition of α reduces the terms in the braces to a quadratic in $k^\mu k_\mu$, which may be solved to produce the desired dispersion relation:

$$D\left(k_\mu, x^\mu\right) = k^\mu k_\mu - \delta\omega^2 - \frac{\delta}{2\left(1+\delta\right)}\left\{\left[\left(\frac{e\mathcal{B}^\mu k_\mu}{m\omega}\right)^2 - \left(1+2\delta\right)\omega_B^2\right] \pm \sqrt{\left(\frac{e\mathcal{B}^\mu k_\mu}{m\omega}\right)^4 + 2\left(2\omega^2 - \omega_B^2 - \omega_P^2\right)\left(\frac{e\mathcal{B}^\mu k_\mu}{m\omega}\right)^2 + \omega_B^4}\right\}. \quad (4.93)$$

This is a covariant extension of the Appleton–Hartree dispersion relation (see, e.g., Boyd & Sanderson, 1969). As in the previous two sections, this continues to bear a resemblance to the dispersion relation for massive particles. Again the effective "mass" depends upon position and the polarization eigenmode. Additionally, it now depends upon the direction of propagation relative to the external magnetic field as well.

Chapter 5

Polarized Radiative Transfer in Refractive Plasmas

Both emission and absorption are local processes. However, because the transfer of radiation necessarily involves a comparison between the state of the radiation at different points in space, global propagation effects need to be accounted for. These take two general forms: correcting for the gravitational redshift and Doppler shifts; and keeping track of the local coordinate system, i.e., ensuring that polarized emission is being added appropriately in the presence of a rotation of the coordinate system propagated along the ray. In addition, for a magnetoactive plasma, it is necessary to determine how to perform the radiative transfer in the presence of refraction.

5.1 Length Scales and Regimes

The problem of performing radiative transfer in a magnetoactive plasma has been treated in detail in the context of radio-wave propagation in the ionosphere (for a detailed discussion see, e.g., Ginzburg, 1970; Budden, 1961). In these cases it was found that there were two distinct limiting regimes (see, e.g., Appendix C). These can be distinguished by comparing two fundamental scales of the affine parameter τ: that over which the polarization eigenmodes (which are generally elliptical) change appreciably, τ_S, and the Faraday rotation length, τ_F. Before τ_S can be defined it is necessary to define a pair of basis four-vectors that define the axes of the polarization

ellipse:

$$\hat{e}_{\parallel}^{\mu} = \frac{\left(k^{\alpha}k_{\alpha}+\omega^{2}\right)\mathcal{B}^{\mu} - \mathcal{B}^{\nu}k_{\nu}\left(k^{\mu}-\omega\overline{u}^{\mu}\right)}{\sqrt{k^{\beta}k_{\beta}+\omega^{2}}\sqrt{\left(k^{\sigma}k_{\sigma}+\omega^{2}\right)\mathcal{B}^{\gamma}\mathcal{B}_{\gamma}-\left(\mathcal{B}^{\gamma}k_{\gamma}\right)^{2}}} \tag{5.1}$$

$$\hat{e}_{\perp}^{\mu} = \frac{\varepsilon^{\mu\nu\alpha\beta}\overline{u}_{\nu}k_{\alpha}\mathcal{B}_{\beta}}{\sqrt{\left(k^{\sigma}k_{\sigma}+\omega^{2}\right)\mathcal{B}^{\gamma}\mathcal{B}_{\gamma}-\left(\mathcal{B}^{\gamma}k_{\gamma}\right)^{2}}}\,, \tag{5.2}$$

where $\varepsilon^{\mu\nu\alpha\beta}$ is the Levi-Civita pseudo-tensor. In terms of these, the ellipticity angle χ can be defined by

$$\tan\chi \equiv i\frac{e_{\parallel}^{\mu}E_{O\,\mu}}{e_{\perp}^{\nu}E_{O\,\nu}} = i\frac{e_{\perp}^{\mu}E_{X\,\mu}}{e_{\parallel}^{\nu}E_{X\,\nu}}\,. \tag{5.3}$$

In general, an additional angle, ϕ, is necessary to define the polarization, namely the angle which defines the orientation of the ellipse. The basis four-vectors have been chosen such that ϕ is identically zero. However, this choice introduces a new geometric term into the equations which accounts for the necessary rotation of the basis four-vectors, contributing a nonzero $d\phi/d\tau$ (see §5.1.2 for more details). Then, in general,

$$\tau_{S} \equiv \left(\left|\frac{d\phi}{d\tau}\right|^{2} + \left|\frac{d\chi}{d\tau}\right|^{2}\right)^{-1/2}\,, \tag{5.4}$$

For the ordered fields employed here (see the appendices),

$$\tau_{S} \simeq \left|\frac{\omega_{B}}{\omega^{3}}\frac{\partial\omega_{P}^{2}}{\partial x^{\mu}}\frac{dx^{\mu}}{d\tau}\right|^{-1}\,, \tag{5.5}$$

where this approximation form is true for small cyclotron and plasma frequencies and all but the most oblique angles of incidence. The Faraday rotation length is defined to be the distance over which the phase difference between the two polarization eigenmodes reaches 2π, i.e.,

$$\tau_{F} \equiv \left|\Delta k_{\mu}\frac{dx^{\mu}}{d\tau}\right|^{-1}\,, \tag{5.6}$$

where Δk^{μ} is the difference between the wave vectors of the two modes. Strictly speaking in addition to τ_{F}, τ_{S} should be compared to a term describing the rate of change of the Faraday rotation length, however in the situations under consideration

here this term is completely dominated by τ_F.

Together, these length scales define three regimes: the *adiabatic* regime ($\tau_F \ll \tau_S$), the *intermediate* regime ($2\tau_F \sim \tau_S$), and the *strongly coupled* regime ($\tau_F \gg \tau_S$). In all regimes the polarization of the plasma eigenmodes is uniquely set by the dispersion equation, equation (4.13).

In general, as $\theta \to \pi/2$, $\Delta k \simeq (\omega_P^2 \omega_B/\omega^2 c)\cos\theta + (\omega_P^2\omega_B^2/\omega^3 c)$, where θ is the angle between the wave-vector and the magnetic field. Hence to remain in the adiabatic regime $\tau_S \gg (\omega/\omega_B)^2 \tau_F(\theta = 0)$, which is typically not true in astrophysical sources. As a result, as the magnetic field becomes perpendicular to the wave-vector, the modes generally become strongly coupled. This is the reason why, when dealing with a large number of field reversals (e.g., in a molecular cloud), the amount of Faraday rotation and conversion is $\propto \mathbf{B} \cdot d\mathbf{x}$ and not $|\mathbf{B}| \cdot d\mathbf{x}$ (which would follow in the adiabatic regime) despite the fact that $\tau_s \gg \tau_F(\theta = 0)$ may be true throughout the entire region.

5.1.1 Adiabatic Regime

In the adiabatic regime the two polarization modes propagate independently (see, e.g., Ginzburg, 1970). As a result, to a good approximation, the net polarization is simply given by the sum of the two polarizations. The intensities, I_O and I_X, of the ordinary and the extraordinary modes, respectively, are not conserved along the ray due to the gravitational redshift. Consequently, the photon occupation numbers of the two modes, N_O and N_X, which are Lorentz scalars, and hence are conserved along the rays, are used. Therefore, the equation of radiative transfer is given by

$$\frac{dN_{O,X}}{d\tau} = \frac{dl}{d\tau}\left(\overline{j}_{O,X} - \alpha_{O,X} N_{O,X}\right) , \tag{5.7}$$

where

$$\frac{dl}{d\tau} = \sqrt{g_{\mu\nu}\frac{dx^\mu}{d\tau}\frac{dx^\nu}{d\tau} + \left(u_\mu \frac{dx^\mu}{d\tau}\right)^2} \tag{5.8}$$

is the conversion from the line element in the LFCR frame to the affine parameterization, and $\overline{j}_{O,X}$ is the emissivity in the LFCR frame scaled appropriately for the occupation number (as opposed to the intensity). In practice, the occupation numbers will be large. However, up to fundamental physical constants, it is permissible to use a scaled version of the occupation numbers such that $N_{O,X} = \omega^{-3} I_{O,X}$ in vacuum.

It is also this regime in which Faraday rotation and conversion occur. However, because these propagation effects result directly from interference between the two modes, and hence require the emission to be coherent among the two modes, when they diverge sufficiently the modes must be added incoherently and thus Faraday rotation and conversion effectively cease. The modes will have divereged sufficiently when

$$|\Delta x_\perp| \gtrsim \frac{\lambda^2}{\Delta\lambda}\,, \tag{5.9}$$

where $\Delta\lambda$ is the emission bandwidth. For broad-band emission, this reduces to $|\Delta x_\perp| \gtrsim \lambda$. Therefore in a highly refractive medium an additional constraint is placed upon Faraday rotation. The depth at which equation (5.9) is first satisfied can be estimated by considering an oblique ray entering a plane-parallel density and magnetic field distribution (at angle ζ to the gradient). In this case, to lowest order in ω_P and ω_B,

$$\frac{d^2\Delta x_\perp}{dz^2} \simeq -\sin\zeta \frac{\partial D}{\partial z} \simeq \frac{\omega_B \omega_P^2}{\omega^3 z} \tag{5.10}$$

As a result,

$$|\Delta x_\perp| \simeq \frac{\omega_B \omega_P^2 z}{2\omega^3}, \quad \text{hence} \quad z_{\max} \simeq \sqrt{\lambda \frac{2\omega^3}{\omega_B \omega_P^2}}\,. \tag{5.11}$$

The resulting number of Faraday rotations, n_F, is then given by

$$n_F \equiv \int_0^{z_{\max}} \frac{\Delta k}{2\pi} dz \simeq \frac{1}{2\pi \sin\zeta}\,, \tag{5.12}$$

which is typically small for all but the smallest ζ. Because, as discussed in Chapter 4, linear polarization is strongly suppressed by refraction, such a small Faraday rotation in negligible. As a result, for the situations of interest here, in this regime the modes

can be added together incoherently to yield the net polarization.

5.1.2 Strongly Coupled Regime

In the limit of vanishing plasma density it is clear that the polarization propagation must approach that in vacuum regardless of the magnetic field geometry. In this limit the two modes must be strongly coupled such that their sum evolves as in vacuum. In particular, it is necessary to keep track of their relative phases. This can be most easily accomplished by using the Stokes parameters to describe the radiation. In this case also it is possible to account for the gravitational redshift by using the photon occupation number instead of intensities, N, N_Q, N_U, N_V. However, it is also necessary to define the N_Q, N_U, and N_V in a manner that is consistent along the entire ray. In order to do this we may align the axes of N_Q along the magnetic field, i.e.,

$$\begin{aligned} N_Q &= N(\hat{e}^\mu_\parallel) - N(\hat{e}^\mu_\perp) \\ N_U &= N\left(\frac{1}{\sqrt{2}}\hat{e}^\mu_\parallel - \frac{1}{\sqrt{2}}\hat{e}^\mu_\perp\right) - N\left(\frac{1}{\sqrt{2}}\hat{e}^\mu_\parallel + \frac{1}{\sqrt{2}}\hat{e}^\mu_\perp\right) \\ N_V &= N\left(\frac{1}{\sqrt{2}}\hat{e}^\mu_\parallel + \frac{i}{\sqrt{2}}\hat{e}^\mu_\perp\right) - N\left(\frac{1}{\sqrt{2}}\hat{e}^\mu_\parallel - \frac{i}{\sqrt{2}}\hat{e}^\mu_\perp\right) , \end{aligned} \tag{5.13}$$

where $N(e^\mu)$ is the occupation number of photons in the polarization defined by e^μ. Thus the problem of relating N_Q, N_U, and N_V along the ray is reduced to propagating $\hat{e}^\mu_\parallel$ and $\hat{e}^\mu_\perp$. A change in τ by $d\tau$ is associated with a rotation of the basis by an angle

$$d\phi = \hat{e}_{\perp\mu}\frac{dx^\nu}{d\tau}\nabla_\nu \hat{e}^\mu_\parallel d\tau \, , \tag{5.14}$$

where the use of the covariant derivative, ∇_ν, accounts for the general relativistic rotations of $\hat{e}^\mu_\parallel$ and $\hat{e}^\mu_\perp$. As a result, the transfer effect due to general relativity *and*

the rotation of the magnetic field about the propagation path is

$$\begin{aligned} \frac{dN_Q}{d\tau} &= -2\frac{d\phi}{d\tau}N_U \\ \frac{dN_U}{d\tau} &= 2\frac{d\phi}{d\tau}N_Q\,, \end{aligned} \tag{5.15}$$

where the factor of 2 arises from the quadratic nature of N.

After a specific emission model is chosen the emissivities and the absorption coefficients are scaled as in Section 5.1.1. An example will be discussed in more detail in Section 5.2.

5.1.3 Intermediate Regime

At some point it is necessary to transition from one limiting regime to the other. In this intermediate regime the polarization freezes out. A great deal of effort has been expended to understand the details of how this occurs (see, e.g., Budden, 1952). However, to a good approximation it is enough to set the polarization at the point when $\tau_F = 2\tau_S$ to the incoherent sum of the polarization eigenmodes (see the discussion in Ginzburg, 1970):

$$\begin{aligned} N &= N_O + N_X \\ N_Q &= -\cos 2\chi (N_O - N_X) \\ N_U &= 0 \\ N_V &= \sin 2\chi (N_O - N_X) \end{aligned} \tag{5.16}$$

It is straightforward to show that in terms of the generalized Stokes parameters N_O and N_X are given by (this is true even when they are offset by a phase)

$$\begin{aligned} N_O &= \frac{1}{2}\left(N - \cos 2\chi N_Q + \sin 2\chi N_V\right) \\ N_X &= \frac{1}{2}\left(N + \cos 2\chi N_Q - \sin 2\chi N_V\right)\,. \end{aligned} \tag{5.17}$$

Note that, in general, polarization information will be lost in this conversion. This is a reflection of the fact that the space spanned by the incoherent sum of the two modes forms a subset of the space of unpolarized Stokes parameters. This is clear from their respective dimensionalities; the former is three-dimensional (there are only three degrees of freedom for the decomposition into the two polarization modes, namely their amplitudes and relative phase), while the later is four-dimensional (I, Q, U, and V, subject only to the condition that $I^2 \geq Q^2 + U^2 + V^2$).

5.2 Low-Harmonic Synchrotron Radiation into Cold Plasma Modes

As discussed in the previous section, emission and absorption are inherently local processes. As a result it will be sufficient in this context to treat them in the LFCR frame, and hence in flat space. In this frame it is enough to solve the problem in three dimensions and then insert quantities in a covariant form.

Because refractive effects become large only when $\omega \sim \omega_B, \omega_P$, for there to be significant spectral and polarimetric effects it is necessary to have an emission mechanism which operates in this frequency regime as well. A plausible candidate is low-harmonic synchrotron emission. It is assumed that a hot power-law distribution of electrons is responsible for the emission while the cold plasma is responsible for the remaining plasma effects. In Chapter 4 we did present the theory for the warm plasma as well, however, as in the conventional magnetoionic theory, it is much more cumbersome to utilize.

5.3 Razin Suppression

A well-known plasma effect upon synchrotron emission is the Razin suppression (see, e.g., Rybicki & Lightman, 1979; Bekefi, 1966). This arises due to the increase in the wave phase velocity above the speed of light, preventing electrons from maintaining

phase with the emitted electromagnetic wave, resulting in an exponential suppression of the emission below the Razin frequency,

$$\omega_R = \frac{\omega_P^2}{\omega_B}\,. \tag{5.18}$$

However, as discussed in the Appendix, for the disk model we have employed here, typically $\omega_B > \omega_P$ and hence the Razin effects do not arise.

5.4 Projection onto Non-Orthogonal Modes

A significant problem with emission mechanisms in the $\omega \sim \omega_B, \omega_P$ frequency regime is that the modes are no longer orthogonal. It is true that for a lossless medium (such as the cold plasma), equation (4.13), which defines the polarization, is self-adjoint. However, because the k^μ differ for the two modes, it is a slightly different equation for each mode, and hence the polarizations are eigenvectors of slightly different hermitian differential operators. In the high-frequency limit this difference becomes insignificant.

The energy in the electromagnetic portion of the wave (neglecting the plasma portion) is given by

$$\mathcal{E} = \frac{\mathbf{E}^* \cdot \epsilon \cdot \mathbf{E}}{4\pi} = \frac{1}{4\pi}\mathbf{E}^* \cdot \left(1 + \frac{4\pi i}{\omega}\sigma\right) \cdot \mathbf{E} \tag{5.19}$$

For each mode ($\mathbf{E}_O$ and $\mathbf{E}_X$), the dispersion equation gives

$$\begin{aligned}\left(\omega^2 + 4\pi i\omega\sigma\right) \cdot \mathbf{E}_{O,X} &= \left(k_{O,X}^2 - \mathbf{k}_{O,X} \otimes \mathbf{k}_{O,X}\right) \cdot \mathbf{E}_{O,X} \\ &= k_{O,X}^2 \left(\mathbf{1} - \hat{\mathbf{k}} \otimes \hat{\mathbf{k}}\right) \cdot \mathbf{E}_{O,X}\,. \end{aligned} \tag{5.20}$$

Therefore, with $\mathbf{E} = \sum_i \mathbf{E}_i$,

$$\mathcal{E} = \frac{1}{4\pi\omega^2} \sum_{i,j} k_j^2 \mathbf{E}_i^* \cdot \left(\mathbf{1} - \hat{\mathbf{k}} \otimes \hat{\mathbf{k}}\right) \cdot \mathbf{E}_j\,. \tag{5.21}$$

However, for a lossless medium it is also true that

$$\mathcal{E} = \mathcal{E}^\dagger = \frac{1}{4\pi\omega^2} \sum_{i,j} k_i^2 \mathbf{E}_i^* \cdot \left(\mathbf{1} - \hat{\mathbf{k}} \otimes \hat{\mathbf{k}} \right) \cdot \mathbf{E}_j \,, \tag{5.22}$$

and therefore,

$$\sum_{i,j} \left(k_i^2 - k_j^2 \right) \mathbf{E}_i^* \cdot \left(\mathbf{1} - \hat{\mathbf{k}} \otimes \hat{\mathbf{k}} \right) \cdot \mathbf{E}_j = 0 \,. \tag{5.23}$$

For a nondegenerate dispersion relation, e.g., that of a magnetoactive plasma, this implies that the the components of the polarization transverse to the direction of propagation are orthogonal for the two modes, i.e.,

$$\hat{\mathbf{F}}_i^* \cdot \hat{\mathbf{F}}_j = k_i^2 \delta_{ij} \tag{5.24}$$

where

$$\hat{\mathbf{F}}_{O,X} = k_{O,X} \frac{\left(\mathbf{1} - \hat{\mathbf{k}} \otimes \hat{\mathbf{k}} \right) \cdot \hat{\mathbf{E}}_{O,X}}{\hat{\mathbf{E}}_{O,X}^* \cdot \left(\mathbf{1} - \hat{\mathbf{k}} \otimes \hat{\mathbf{k}} \right) \cdot \hat{\mathbf{E}}_{O,X}} \,. \tag{5.25}$$

As a result it is possible to define $\mathcal{E}_{O,X}$ such that

$$\mathcal{E}_{O,X} = \frac{\mathbf{F}_{O,X}^* \cdot \mathbf{F}_{O,X}}{4\pi} \quad \text{and} \quad \mathcal{E} = \sum_i \mathcal{E}_i \,, \tag{5.26}$$

i.e., that the electromagnetic energy can be uniquely decomposed into the electromagnetic energy in the two modes.

Expressions for the $\mathbf{F}_{O,X}$ can be obtained by solving for the eigenvectors of the dispersion equation. For the cold magnetoactive plasma this gives

$$\hat{\mathbf{F}}_{O,X} = \frac{k_{O,X}}{\sqrt{2}} \left[\sqrt{1 \pm (1+\varepsilon)^{-1/2}} \, \hat{\mathbf{e}}_\parallel \pm \, i \sqrt{1 \mp (1+\varepsilon)^{-1/2}} \, \hat{\mathbf{e}}_\perp \right] \,, \tag{5.27}$$

where, (not to be confused with the Levi-Civita pseudo-tensor)

$$\varepsilon = \left(\frac{\sin^2\theta}{2\cos\theta} \frac{\omega\omega_B}{\omega_P^2 - \omega^2} \right)^{-2} \,, \tag{5.28}$$

θ is the angle between the magnetic field and the wave vector, and $\hat{\mathbf{e}}_{\parallel,\perp}$ are the flat space analogues of the basis vectors in equation (5.2). θ may be defined covariantly by

$$\cos^2\theta = \frac{\left(\mathcal{B}^\mu k_\mu\right)^2}{\mathcal{B}^\nu \mathcal{B}_\nu \left(k^\sigma k_\sigma + \omega^2\right)} \,. \tag{5.29}$$

This corresponds to the polarization found in the literature (cf. Budden, 1961).

5.5 Emissivities

Because the electromagnetic energy can be uniquely decomposed into contributions from each polarization eigenmode, it is possible to calculate the emissivities and absorption coefficients by the standard far-field method. For synchrotron radiation this was originally done by Westfold, 1959. The calculation is somewhat involved but straightforward and has been done in detail in the subsequent literature (see, e.g., Rybicki & Lightman, 1979). Consequently, only the result for the power emitted (per unit frequency and solid angle) for a given polarization is quoted below:

$$\langle P^{O,X}_{\omega\,\Omega} \rangle = \frac{e^3 \mathcal{B} \sin\theta}{8\sqrt{3}\pi^2 m k^2_{O,X}} n_r^2 \int d^3p f(\mathbf{p}) \Bigg[\left(\left| \hat{\mathbf{F}}_{O,X} \cdot \hat{\mathbf{e}}_\parallel \right|^2 + \left| \hat{\mathbf{F}}_{O,X} \cdot \hat{\mathbf{e}}_\perp \right|^2 \right) F(x) + \left(\left| \hat{\mathbf{F}}_{O,X} \cdot \hat{\mathbf{e}}_\parallel \right|^2 - \left| \hat{\mathbf{F}}_{O,X} \cdot \hat{\mathbf{e}}_\perp \right|^2 \right) G(x) \Bigg] \,, \tag{5.30}$$

where

$$x = \frac{2mc\omega}{3\gamma^2 e \mathcal{B} \sin\theta} \,, \tag{5.31}$$

$f(\mathbf{p})$ is the distribution function of emitting electrons, n_r is the ray-refractive index (for a suitable definition see Bekefi, 1966), and F and G have their usual definitions,

$$F(x) = x \int_x^\infty K_{\frac{5}{3}}(y) dy \quad \text{and} \quad G(x) = x K_{\frac{2}{3}}(x) \,, \tag{5.32}$$

where the $K_{5/3}$ and $K_{2/3}$ are the modified Bessel functions of 5/3 and 2/3 order, respectively. The addition factor of n_r^2 arises from the difference in the photon phase

space, d^3k and the analogous integral over frequency, $4\pi d\omega$.

For the adiabatic regime, the emissivities, $\overline{j}_{O,X\,\omega}$, can now be defined:

$$\overline{j}_{O,X} = \frac{1}{4\pi n_r^2 \omega^3} \langle P^{O,X}_{\omega\,\Omega} \rangle \,. \tag{5.33}$$

For a power-law distribution of emitting electrons, $f(\mathbf{p})d^3p = \mathcal{C}\gamma^{-s}d\gamma$, this gives

$$\overline{j}_{O,X} = \frac{\sqrt{3}e^2\mathcal{C}}{24\pi^2\omega^2 c(1+s)} \left(3\frac{\omega_B}{\omega}\sin\theta\right)^{\frac{s+1}{2}} \Gamma\left(\frac{s}{4}+\frac{19}{12}\right) \times \Gamma\left(\frac{s}{4}-\frac{1}{12}\right)\left[1 \pm \frac{3s+3}{3s+7}(1+\varepsilon)^{-\frac{1}{2}}\right] . \tag{5.34}$$

The Stokes emissivities and absorption coefficients for an emitting hot power law (ignoring effects of order γ^{-1} as these explicitly involve the propagation through the hot electrons) are given by

$$\overline{j}_N = \overline{j}_O + \overline{j}_X \tag{5.35}$$

$$\overline{j}_Q = \frac{\sqrt{3}e^2\mathcal{C}}{48\pi^2\omega^2 c} \left(3\frac{\omega_B}{\omega}\sin\theta\right)^{\frac{s+1}{2}} \times \Gamma\left(\frac{s}{4}+\frac{7}{12}\right)\Gamma\left(\frac{s}{4}-\frac{1}{12}\right) \tag{5.36}$$

$$\overline{j}_U = \overline{j}_V = 0 \,. \tag{5.37}$$

Note that for low γ synchrotron can efectively produce circular polarization, namely $\overline{j}_V \sim 3/\gamma$. The production of circular polarization in this way in environments with large Faraday depths will be considered in future publications.

5.6 Absorption Coefficients

For the adiabatic regime, detailed balance for each mode requires that the absorption coefficients are then given by

$$\alpha_{O,X} = \frac{\sqrt{3}\pi e^2 \mathcal{C}}{6\omega mc} \left(3\frac{\omega_B}{\omega}\sin\theta\right)^{\frac{s+2}{2}} \Gamma\left(\frac{s}{4}+\frac{11}{6}\right)\Gamma\left(\frac{s}{4}+\frac{1}{6}\right)\left[1 \pm \frac{3s+6}{3s+10}\left(1+\varepsilon\right)^{-\frac{1}{2}}\right]. \tag{5.38}$$

In the strongly coupled regime, the Stokes absorption coefficient matrix is (see, e.g., Jones & O'Dell, 1977b, and references therein),

$$\begin{pmatrix} \alpha_N & \alpha_Q & 0 & \alpha_V \\ \alpha_Q & \alpha_N & 0 & 0 \\ 0 & 0 & \alpha_N & 0 \\ \alpha_V & 0 & 0 & \alpha_N \end{pmatrix}, \tag{5.39}$$

where the Faraday rotation and conversion due to the hot electrons have been ignored as a result of the fact that they will be negligible in comparison to the Faraday rotation and conversion due to the cold electrons. The individual α's can be obtained in terms of the $\alpha_{O,X}$ using the fact that the energy in the electromagnetic oscillations can be uniquely decomposed into contributions from each mode (equation (5.26)). Then,

$$\begin{aligned} \frac{dN}{d\lambda} &= \frac{dN_O}{d\lambda} + \frac{dN_X}{d\lambda} \\ &= j_O + j_X - \alpha_O N_O - \alpha_X N_X \\ &= (j_O + j_X) - \frac{1}{2}(\alpha_O + \alpha_X)N \\ &\quad + \frac{1}{2}\cos 2\chi\,(\alpha_O - \alpha_X)\,Q - \frac{1}{2}\sin 2\chi\,(\alpha_O - \alpha_X)\,V\,. \end{aligned} \tag{5.40}$$

Therefore, the absorption coefficients may be identified as

$$\alpha_N = \frac{1}{2}\left(\alpha_O + \alpha_X\right) \tag{5.41}$$

$$\alpha_Q = -\frac{1}{2}\cos 2\chi\left(\alpha_O - \alpha_X\right) \tag{5.42}$$

$$\alpha_V = \frac{1}{2}\sin 2\chi\left(\alpha_O - \alpha_X\right) . \tag{5.43}$$

5.7 Unpolarized Low-Harmonic Synchrotron Radiation

To highlight the role of refraction in the generation of polarization, an unpolarized emission mechanism is also used. To compare with the results of the polarized emission model discussed in the previous section, the artificial scenario in which the synchrotron emission is split evenly into the two modes was chosen. In this case,

$$\bar{j}_{O,X}^{\mathrm{UP}} = \frac{1}{2}\bar{j}_N \,, \tag{5.44}$$

and

$$\bar{j}_N^{\mathrm{UP}} = \bar{j}_N \,, \tag{5.45}$$

with the other Stokes emissivities vanishing. Similarly, the absorption coefficients are given by

$$\alpha_{O,X}^{\mathrm{UP}} = \alpha_N^{\mathrm{UP}} = \alpha_N \,, \tag{5.46}$$

with the other absorption coefficients vanishing as well.

5.8 Constraints upon the Emitting Electron Fraction

For refractive plasma effects to impact the spectral and polarimetric properties of an accretion flow, it is necessary that it be optically thin. This places a severe constraint

upon the fraction of hot electrons, $f \equiv \mathcal{C}/[n_e(s-1)]$. In terms of the plasma frequency and f the absorptivity is approximately

$$\alpha_N \sim \frac{\sqrt{3}}{24c} f \frac{\omega_P^2}{\omega} \left(3\frac{\omega_B}{\omega}\sin\theta\right)^{(s+2)/2} . \tag{5.47}$$

With $s \sim 2$, and $\omega \sim \omega_P$, ω_B, the typical optical depth (not to be confused with the affine parameter) is

$$\tau \sim 10^{-1} f \frac{R}{\lambda} \qquad \text{hence} \qquad f \sim 10\frac{\lambda}{R}\,, \tag{5.48}$$

where R is the typical disk scale length (here on the order of $10M$).

Chapter 6

Generic Example Applications

In the previous chapters the general theory of a covariant magnetoionic theory was presented for electron-ion (in the Appleton-Hartree limit) and pair plasmas. While astrophysical plasmas will in general be warm, the cold electron plasma does provide an instructive setting in which to highlight some of the similarities and differences that a fully general relativistic magnetoionic theory has compared to general relativity or plasma effects alone.

6.1 Bulk Plasma Flows

A number of novel effects will appear in special relativistic plasma flows. The covariant formulation of magnetoionic theory can have implications for the structure of the dispersion relation. As briefly mentioned in Section 4.5.2, the equation for the magnitude of the spatial part of the wave vector is now cubic. This is essentially due to Doppler shifting. Thus these effects should appear in relativistic bulk plasma flows as well as in regions of strong frame dragging (e.g., near the ergosphere of a Kerr hole).

For a relativistic bulk flow (in the x direction)

$$\omega = \frac{k_t - v k_x \cos\theta}{\sqrt{1-v^2}}\,, \tag{6.1}$$

where θ is the angle between the wave vector and the motion and v is the velocity

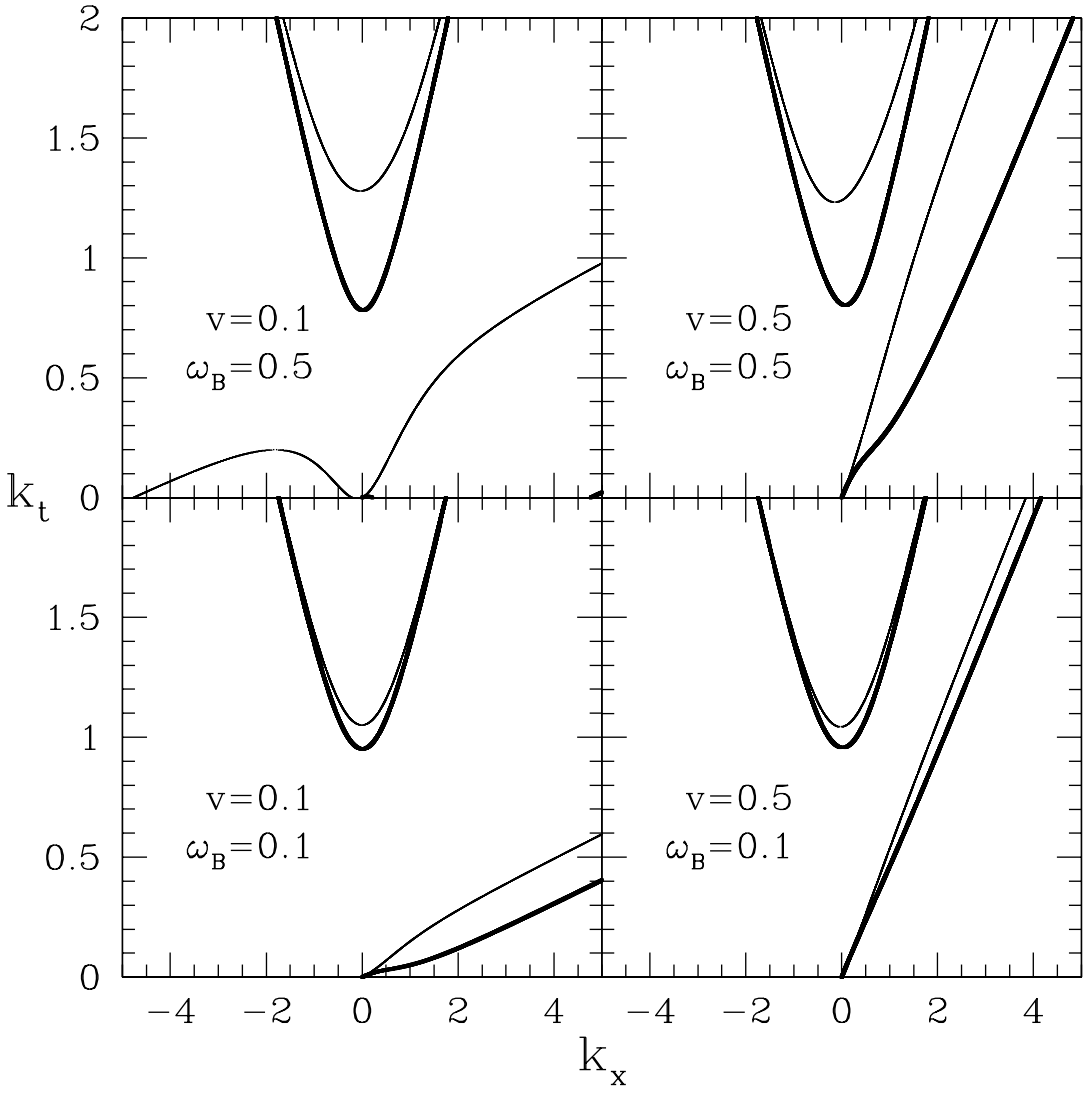

Figure 6.1: The dispersion diagram at a number of magnetic field strengths and velocities for a relativistic bulk plasma flow. The frequency scale is set by $\omega_P = 1$. The ordinary (extraordinary) eigenmode is shown by the thick (thin) line. Note that the dispersion diagrams are asymmetric due to the plasma motion.

of the motion. Clearly the coupling between the previously mentioned third branch depends upon both v and θ, being strongest when $\theta = 0$. Shown in Figure 6.1 are the quasi-longitudinal dispersion relations for a relativistic bulk flow for a number of velocities and magnetic field strengths and $\theta = 0$. The frequencies are measured in units of the plasma frequency, making this otherwise scale invariant. Note that

a whistler-like branch appears for the ordinary mode which is not present in the nonrelativistic theory. Similar to the whistler branch of the extraordinary mode, it is asymmetric due to the bulk motion. In the limit of vanishing plasma density this branch does not transform into a vacuum branch, in much the same manner as portions of the whistler. Therefore, in the context of a strongly sheared flow, this mode cannot escape from the plasma, necessarily reflecting at the surfaces of the plasma distribution. This may have implications for the pressure balance in thick disks with large velocity shears and jets, even at frequencies where these are optically thin.

In bulk plasma flows the new branch appears because the velocity mixes the spatial and temporal components of k^μ. In a Kerr spacetime, frame dragging is responsible for mixing these components. In this case

$$\omega = \sqrt{-g^{tt}} \left(k_t + \frac{g^{\phi t}}{g^{tt}} k_\phi \right) . \tag{6.2}$$

This is similar to equation (6.1) with the role of the velocity being taken by $g^{\phi t}/g^{tt}$. Hence, the overall effect is qualitatively the same; a new branch similar to the whistler appears for the ordinary mode.

6.2 Relativistic Shearing Flows and Jets

Jets represent a natural environment in which relativistically shearing plasmas must be considered. While it is currently unclear as to what type of plasma inhabits jets, a pair plasma is clearly the least restrictive in terms of energy per particle, and is the model adopted here for the purpose of concreteness. Because it is generally necessary for the density to be low inside of the jet, refractive effects are unlikely to have a significant impact. Nonetheless, it is possible to significantly modify the net polarization associated with a non-flat emission mechanism.

Emission mechanisms can typically be parametrized in terms of the frequency in the LFCR frame, ω, as discussed at length in Section 5.2. Therefore, the evolution

of ω along the ray determines the departure from the vacuum emissivity. From its definition,

$$\frac{d\omega}{d\tau} = \frac{d\overline{u}^\mu}{d\tau} k_\mu + \overline{u}^\mu \frac{dk_\mu}{d\tau} \tag{6.3}$$

$$= k_\mu \frac{\partial \overline{u}^\mu}{\partial x^\nu} \frac{\partial D}{\partial k_\mu} - \overline{u}^\mu \frac{\partial D}{\partial x^\mu} \,, \tag{6.4}$$

where the ray equations were used. This can be simplified greatly if it is assumed that D is a function only of $k^2 \equiv k^\alpha k_\alpha$, ω, and x^μ, as is the case for the pair plasma. In this case

$$\frac{d\omega}{d\tau} = 2k_\mu k^\nu \frac{\partial \overline{u}^\mu}{\partial x^\nu} \frac{\partial D}{\partial k^2} - \overline{u}^\mu \frac{\partial D}{\partial x^\mu} \,. \tag{6.5}$$

The first term arises from crossing shear layers (cf. section B.2 and recall that this is Minkowski space). Therefore, the evolution in the difference between the local frequencies of the two modes is given by

$$\begin{aligned} \frac{d\Delta\omega}{d\tau} &= 2\frac{\partial \overline{u}^\mu}{\partial x^\nu} \left(k_{1\,\mu} k_1^\nu \frac{\partial D_1}{\partial k^2} - k_{2\,\mu} k_2^\nu \frac{\partial D_2}{\partial k^2} \right) - \overline{u}^\mu \frac{\partial \left(D_1 - D_2 \right)}{\partial x^\mu} \\ &= 2\frac{\partial \overline{u}^\mu}{\partial x^\nu} \left(\Delta k_\mu k^\nu + k_\mu \Delta k^\nu \right) - \frac{\overline{u}^\mu}{\omega^2} \frac{\partial \omega_P^2 \omega_B^2}{\partial x^\mu} \,, \end{aligned} \tag{6.6}$$

where this last expression is appropriate for high frequencies in a pair plasma. This must be supplemented with an equation for Δk^μ,

$$\frac{d\Delta k_\mu}{d\tau} = -\frac{\partial \Delta D}{\partial x^\mu} \,. \tag{6.7}$$

For concreteness and simplicity, we assume that in the lab frame the jet travels along the z-axis, shears only in the x direction, the plasma density and/or magnetic field gradients are along the z-axis, and the line of sight lies in the x-z plane. Then, $\Delta k^\mu = \Delta k^z \delta^{\mu z}$, and thus all of the shearing terms in equation (6.6) vanish. The remaining terms then give

$$\frac{d\Delta\omega}{d\tau} = -\frac{\gamma\beta}{\omega^2} \frac{d\omega_P^2 \omega_B^2}{dz} = -\frac{1}{2k^z} \frac{\gamma\beta}{\omega^2} \frac{d\omega_P^2 \omega_B^2}{d\tau} \,, \tag{6.8}$$

where the last equality is obtained via the ray equations. As a result, a rough approximation for $\Delta\omega$ is

$$\frac{\Delta\omega}{\omega} \simeq -\gamma^2\beta\frac{\omega_P^2\omega_B^2}{\omega^4} \simeq -\gamma^2\beta\frac{\omega_P^2}{\omega^2}\left(\frac{\omega_B}{\omega}\right)^2 , \tag{6.9}$$

which may be large given γ despite the smallness of ω_P and ω_B.

For non-gray emissivities, this will result in a net polarization due to the difference in emission into the two polarization eigenmodes. This will be characterized by a rotation of the polarization angle by 90° at breaks in the spectrum in which the spectral index changes sign (e.g., when the source goes from being optically thick to optically thin).

Many of these effects will also be present in the context of an ion dominated jet as well. However, in this case the resultant polarization would be expected to be dominantly circular due to the polarization of the plasma eigenmodes. Furthermore, since $\Delta D \simeq \omega_P^2\omega_B/\omega$,

$$\frac{\Delta\omega}{\omega} \simeq -\gamma^2\beta\frac{\omega_P^2}{\omega^2}\frac{\omega_B}{\omega} , \tag{6.10}$$

hence the necessarily lower γ could be moderated by the factor of ω/ω_B in comparison to the result for the pair plasma.

6.3 Isotropic Plasmas and Particle Dynamics

In both special and general relativistic settings, the propagation of photons through an isotropic (field free) plasma can be represented in a manner analogous to that of particle dynamics in a potential (see, e.g., Thompson et al., 1994, for the nonrelativistic case). Following the manipulations in Appendix A, it is straightforward to show that for the dispersion relation given in Section 4.5.1, $D = k^\mu k_\mu + \omega_P^2$, that

$$v^\nu\nabla_\nu v^\mu = -\nabla^\mu 2\omega_P^2 , \tag{6.11}$$

where $v^\mu \equiv dx^\mu/d\tau$, i.e., $2\omega_P^2$ acts as a potential in which the the photons propagate (the factor of 2 is due to the particular affine parameter chosen, namely that associated with the choice of the dispersion relation given above).

For plasmas in which magnetoionic effects are not significant to the photon propagation (magnetoionic effects may still be important for emission and the propagation of polarization) this allows a somewhat more simplified analysis. If enough symmetries are present, then the rays may be determined via direct integration. For example, consider a stationary, spherically symmetric plasma distribution around a Schwarzschild black hole. In this case equation (6.11) shows that v_t and v_ϕ are conserved, associated with the time and azimuthal Killing vector fields, respectively. Therefore, with the dispersion relation,

$$\begin{aligned}
\frac{dt}{d\tau} &= v^t = g^{tt} v_t = -\left(1 - \frac{2M}{r}\right)^{-1} v_t \\
\frac{d\phi}{d\tau} &= v^\phi = g^{\phi\phi} v_\phi = \frac{v_\phi}{r^2} \\
\frac{dr}{d\tau} &= v^r = \sqrt{v_t^2 - \left(1 - \frac{2M}{r}\right)\left(\frac{v_\phi}{r^2} + 4\omega_p^2\right)},
\end{aligned} \tag{6.12}$$

Which may be directly integrated to give the ray as a function of the affine parameter τ in precisely the same fashion as is typically done to find the particle orbits of the Schwarzschild metric.

6.4 Bondi Accretion Flow

6.4.1 Photon Capture Cross Sections

In the vicinity of a black hole, polarization can arise even in the case of a gray, intrinsically unpolarized emissivity. This occurs when one mode is preferentially captured by the black hole due to dispersive plasma effects. Even without a method for performing the radiative transfer, this can be estimated by considering the photon capture cross section of Schwarzschild black hole. It is necessary to provide a plasma

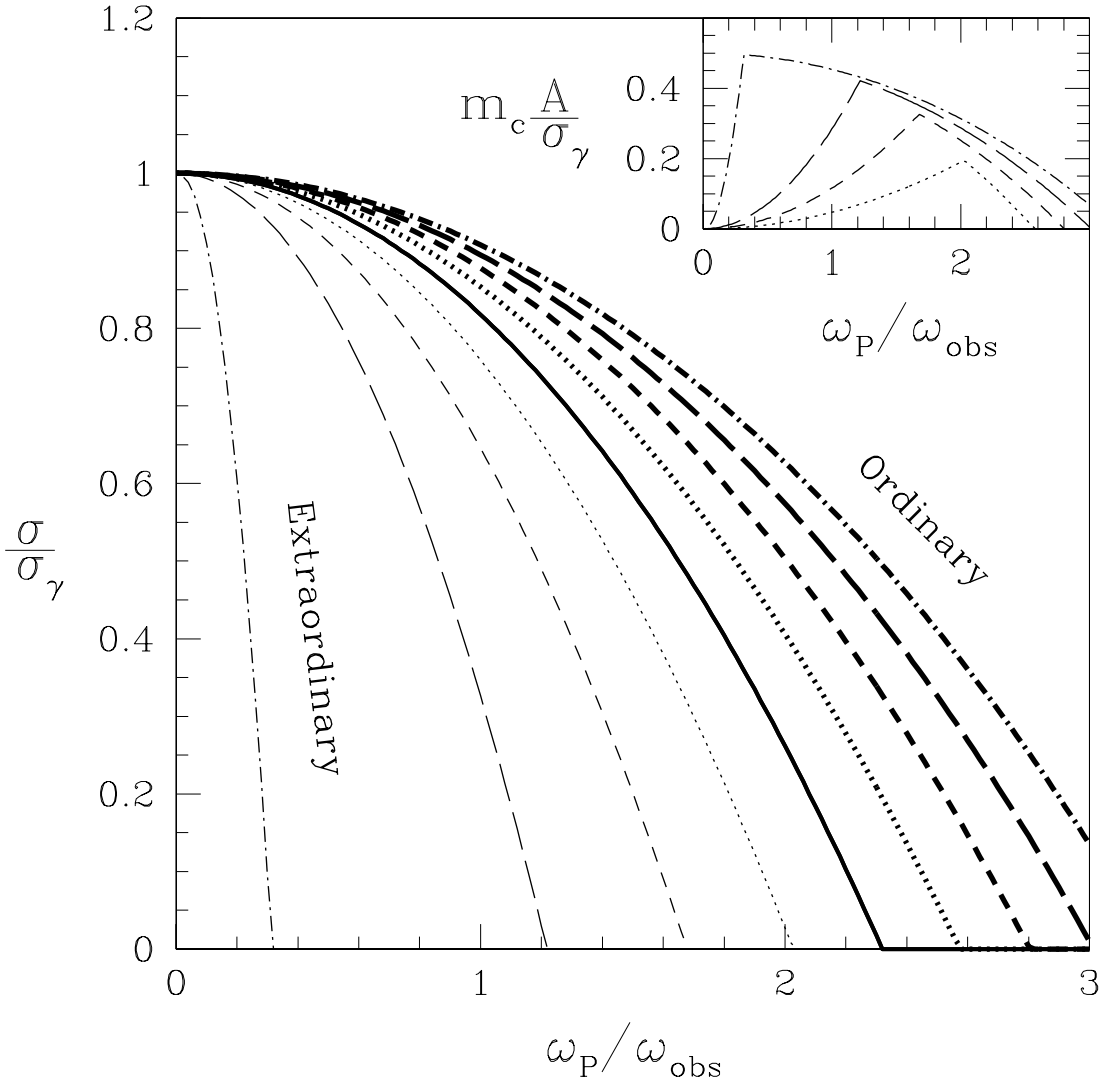

Figure 6.2: Photon capture cross sections in units of the vacuum capture cross section, $\sigma_\gamma = 27\pi M^2$, for the quasi-longitudinal approximation as a function of plasma density ($\omega_P/\omega_{\rm obs}$ is the value of the plasma frequency at $r = 3M$) at a number of magnetic field strengths. The solid, dotted, short dashed, long dashed, and dash-dotted lines correspond to $\omega_B/\omega_{\rm obs} = 0$, 0.7, 1.4, 2.1, and 2.8, respectively, at $r = 3M$. The inset shows the circular polarization fraction, m_c, in terms of the effective emission area, A, for the same set of magnetic field strengths.

geometry—the plasma density, velocity, and magnetic field—as functions of position. Here, the density is given by the self-similar Bondi solution, $\omega_P \propto r^{-3/4}$, the magnetic field is chosen to be a fixed fraction of the equipartition value, $\omega_B \propto r^{-5/4}$, and

the velocity is chosen such that the plasma has zero angular momentum, i.e., $\overline{u}_t = 1/\sqrt{-g^{tt}}$ and $\overline{u}_r = \overline{u}_\theta = \overline{u}_\phi = 0$. While this doesn't correspond to a realistic accretion flow, it does provide insight into the type of effects dispersive refraction can have. In order to further simplify the problem the quasi-longitudinal approximation was used. Typically this is a good approximation, only failing when the angle between k^μ and $\mathcal{B}^\mu$ is within $\sim \omega_B/\omega$ of $\pi/2$. This dispersive polarization mechanism produces primarily circular polarization for the same reason.

Shown in Figure 6.2 are these cross sections for a number of different plasma densities (through ω_P) and magnetic field strengths (through ω_B). These are both scaled by the observed frequency at infinity, and hence are not tied to any particular frequency scale. The capture cross section of the extraordinary mode decreases more rapidly than that of the ordinary mode, with increasing density. The disparity between the two capture cross sections increases with increasing magnetic field strength.

This can be a very efficient manner of creating polarization over the inner portions of the accretion flow. However, far from the hole (outside the inner $5 - 10M$) this becomes a small effect. As a result, the fraction of polarization produced depends upon the magnitude of the diluting emission from regions of the accretion flow distant from the hole. Nonetheless, it is possible to parameterize the unknown emission in terms of an effective emitting area (the details of which still depend upon the details of the accretion flow). Shown in the inset of Figure 6.2 is the circular polarization fraction scaled by the effective emission area in units of the vacuum photon capture cross section.

6.4.2 Ray Trajectories

With general dispersion relation for cold magnetoactive plasmas, equation (4.93), and the ray equations, equations (4.19), it is straightforward to explicitly construct rays. The plasma geometry outlined in the previous section will be used here as well, with the scales set by $\omega_P(r = 3M) = \omega_{\rm obs}$ and $\omega_B(r = 3M) = 2\omega_{\rm obs}$, where $\omega_{\rm obs}$ is the

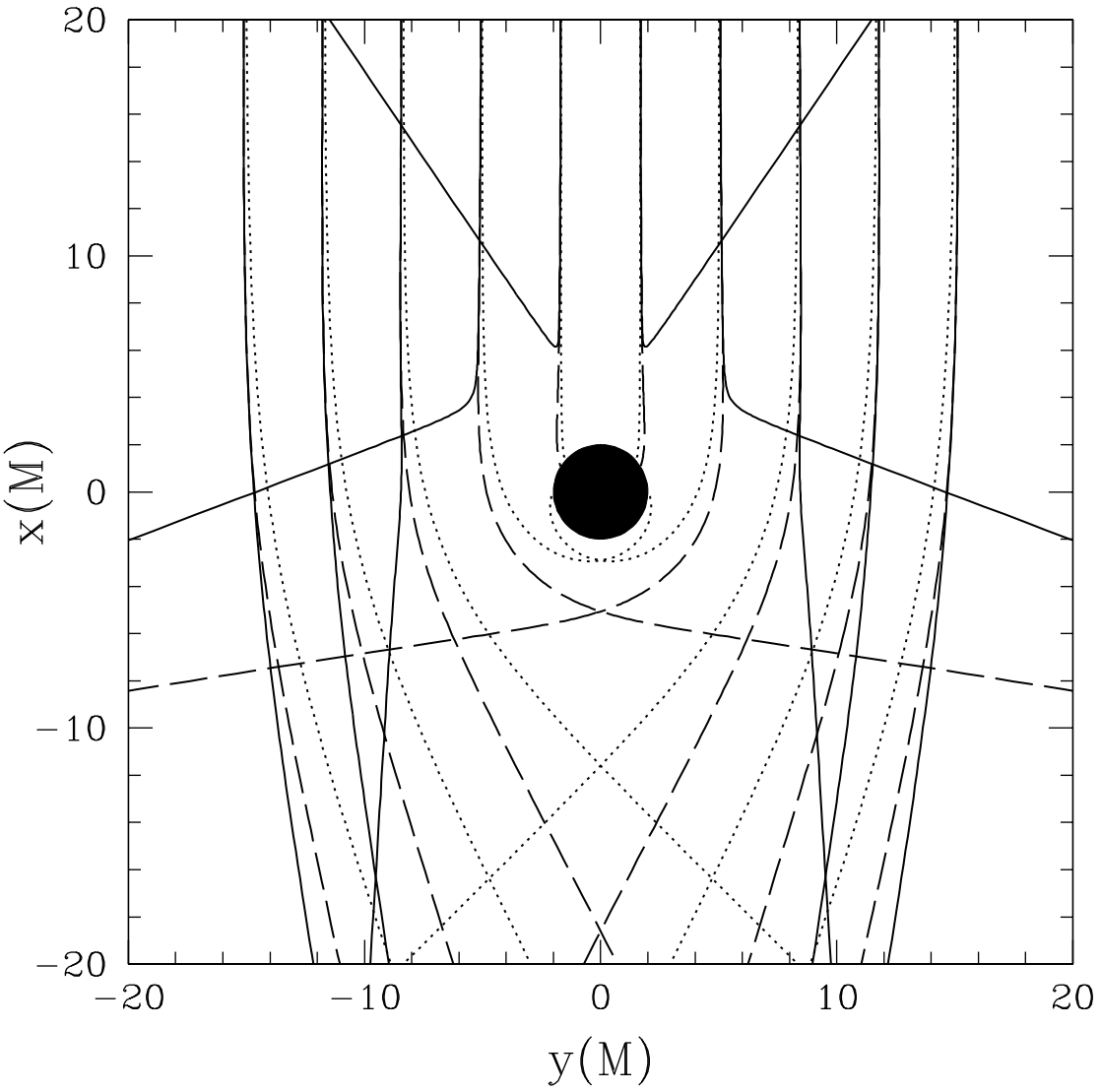

Figure 6.3: The paths of the ordinary and extraordinary polarization eigenmodes in the vicinity of a Schwarzschild black hole are shown by the dashed and solid lines, respectively, for a number of impact parameters. The dotted lines show the null geodesics for comparison. The x axis lies along the ray paths at infinity, and the y axis is orthogonal to both, the x axis and the slice of impact parameters considered. The plasma density is $\propto r^{-3/2}$ and $\omega_P(r = 3M) = \omega_{\rm obs}$. The magnetic field has a split monopole geometry with its strength $\propto r^{-5/4}$ and $\omega_B(r = 3M) = 2\omega_{\rm obs}$. The horizon is shown by the filled region in the center.

frequency observed at infinity. In Figure 6.3 rays are propagated in the vicinity of a Schwarzschild black hole. For comparison, in Figure 6.4 rays are propagated near a

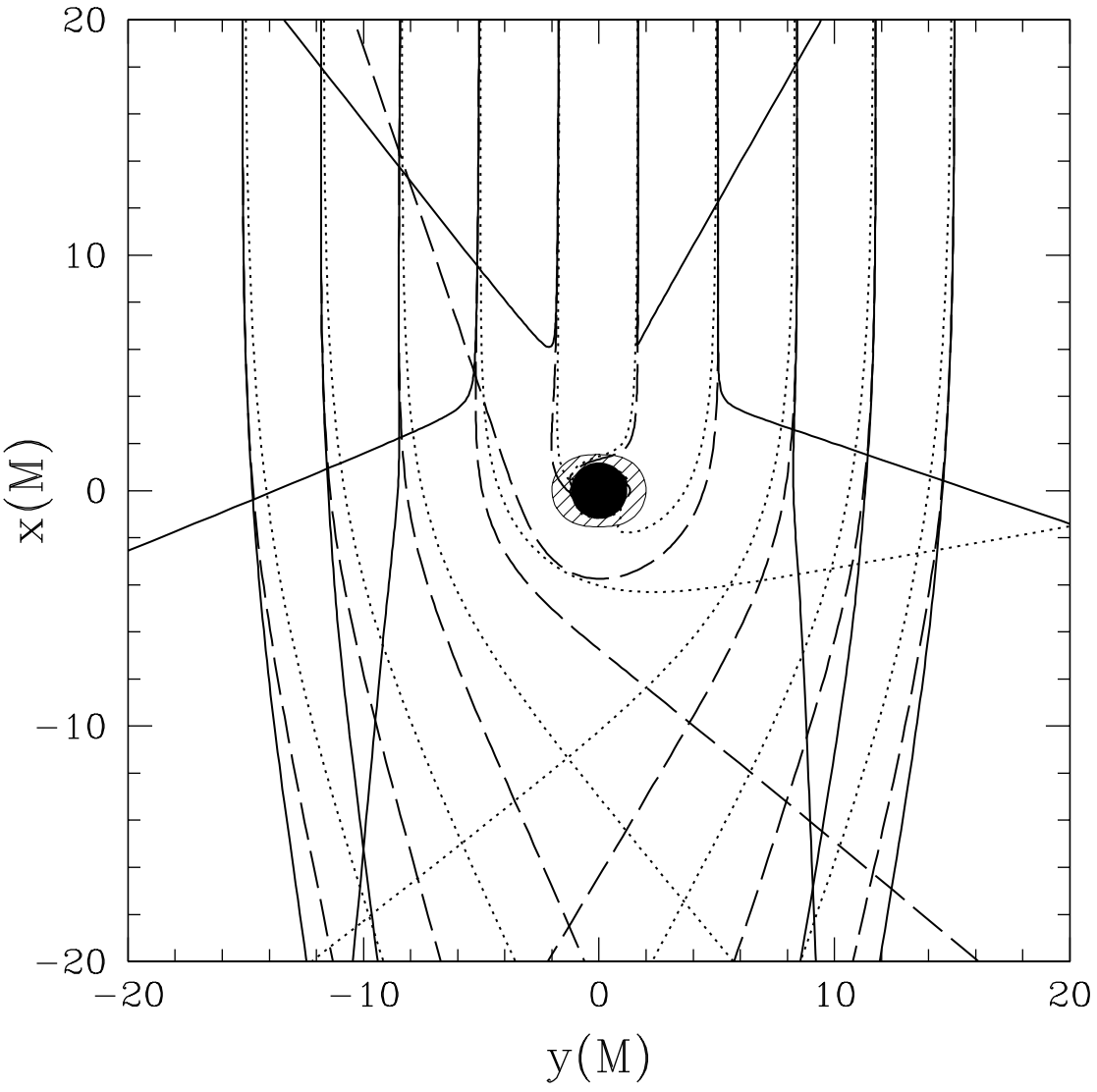

Figure 6.4: The paths of the ordinary and extraordinary polarization eigenmodes in the vicinity of maximally rotating Kerr black hole are shown by the dashed and solid lines, respectively, for a number of impact parameters. The dotted lines show null geodesics for comparison. The plasma parameters are the same as those for Figure 6.3. In addition to the horizon, the ergosphere is shown by the partially shaded region. The rays originate from 60° above the equatorial plane. The y axis is orthogonal to the the rotation axis of the black hole.

maximally rotating Kerr black hole. The null geodesics are shown by the dotted lines for reference. In both figures the extraordinary mode (solid lines) is refracted the most, and the ordinary mode (dashed lines) is refracted away from the null geodesics.

This is precisely what is expected on the basis of the capture cross sections presented in Section 6.4.1. In addition to dispersive plasma effects, comparison with the null geodesics demonstrates that general relativistic effects are also significant.

6.4.3 Polarization Maps

The impact that dispersive plasma effects can have upon the spectrum of an accreting object can be illustrated by maps of the intensity. Here, in addition to the plasma geometry employed in the previous two sections, an optically thick Shakura-Sunyaev disk is introduced. The emission is solely from this disk and assumed to be thermal with

$$T(r) \propto \left(1 - \sqrt{R_{\rm min}/r}\right)^{3/10}$$

(see, e.g., Frank et al., 1992). The overall constant is dependent upon a number of disk parameters and hence is not of particular interest here. Nonetheless, it is chosen such that $kT(r = \infty) = \nu_{\rm obs}$ for convenience. The innermost radius of the disk, $R_{\rm min}$, is chosen to be $3M$. Doppler effects due to the rotation of the disk are ignored here.

Shown in Figure 6.5 are the intensity maps for when (a) plasma effects are neglected, (b) plasma effects are included, (c) only the left-handed circular polarization (ordinary mode) is considered, (d) only the right-handed circular polarization (extraordinary mode) is considered. Because the overall flux from the disk is dependent upon the details of the accretion flow, the intensities are normalized by the highest intensity in panel (b). Comparing panels (a) and (b) demonstrates that including dispersive plasma effects makes a significant difference. This difference originates primarily from contribution by the extraordinary mode shown in panel (d).

As implied by Figure 6.2, the shadow the black hole casts upon the extraordinary mode is less than that cast upon the ordinary mode, which is in turn less than that upon the null geodesics. In addition to the differences in the overall intensities, there is a substantial difference between the contributions from the two polarizations as seen by comparing panels (c) and (d).

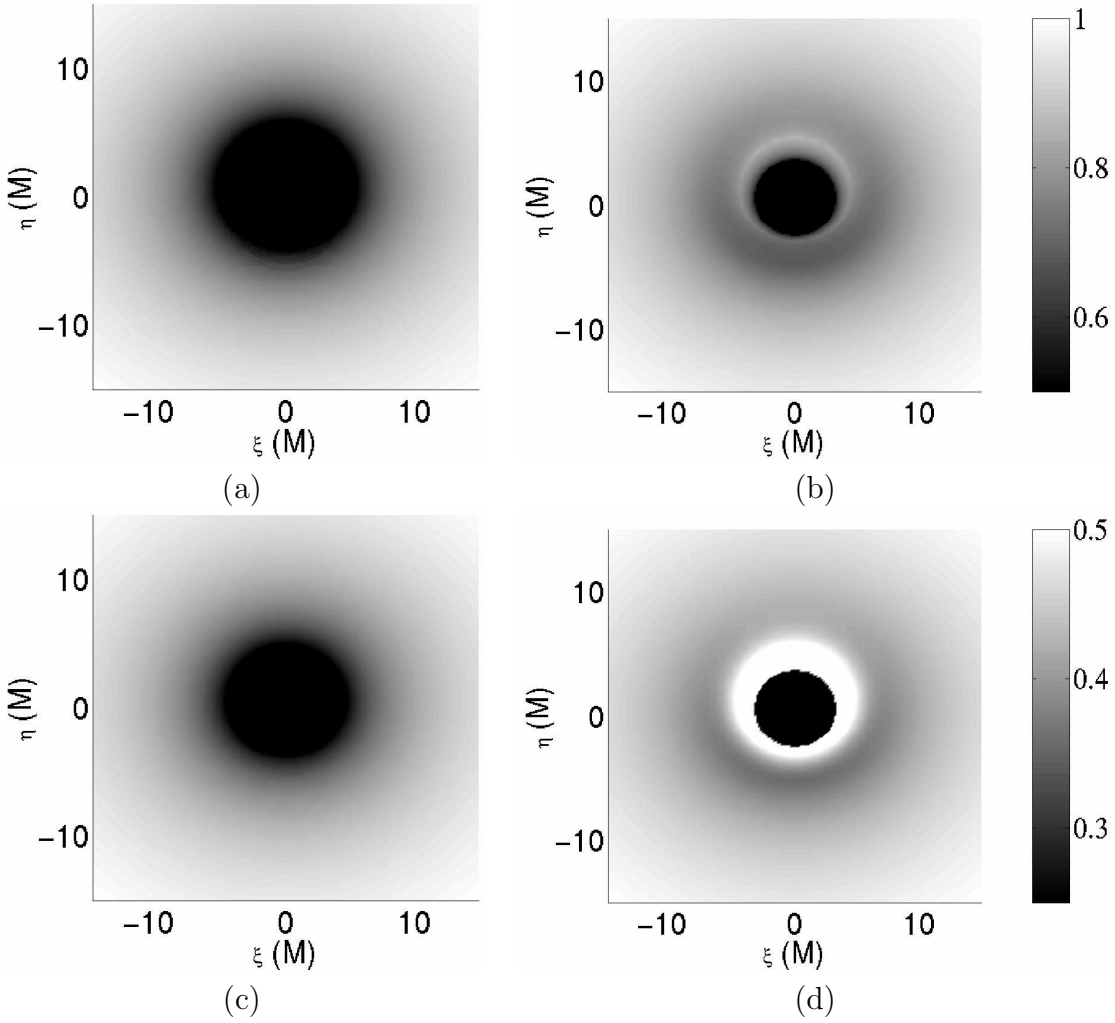

Figure 6.5: Shown is the normalized intensity for an optically thick, Shakura-Sunyaev disc around a Schwarzschild black hole when (a) plasma effects are neglected, (b) plasma effects are included, (c) only the left-handed circular polarization (ordinary mode) is included, (d) only the right-handed circular polarization (extraordinary mode) is included. Note the different scales for total intensities ((a) and (b)) and the polarized intensities ((c) and (d)). The disk is inclined 60° relative to the line of sight. ξ is parallel to the equatorial plane. η is in the line of sight-azimuthal axis plane. The overall scale is set by the choice of observation frequency and the parameters of the disk and hence are not relevant here. The plasma geometry is the same as that for Figures 6.3 and 6.4.

6.5 Thick Disk

6.5.1 Disk Model

Before any quantitative results are presented it is necessary to select a physically motivated plasma and magnetic field distribution. Here this takes the form of an

azimuthally symmetric, thick, barotropic disk around a maximally rotating Kerr black hole ($a \simeq 0.98$). The magnetic field is chosen to lie upon surfaces of constant angular velocity, thus insuring that it does not shear. In order to maintain such a field it must also be strong enough to suppress the magneto-rotational instability. Further details may be found in the Appendix B

6.5.2 Ray Trajectories

Figure 6.6 shows vertical and horizontal slices of rays propagated back through the disk from an observer elevated to 45° above the equatorial plane at a frequency $\omega_\infty = 3\omega_{P\,\mathrm{max}}/4$. Note that since the maximum occurs at $r_{\mathrm{eq}} = 2M$, the relativistically blue-shifted ω is approximately $1.8\omega_{P\,\mathrm{max}}$ placing it comfortably above the plasma resonance at all points (assuming Doppler effects do not dominate at this point.)

The refractive effects of the plasma are immediately evident with the extraordinary mode being refracted more so. Gravitational lensing is also shown to be important over a significant range of impact parameters. There will be an azimuthal asymmetry in the ray paths due to both the black hole spin and the Doppler shift resulting from the rotation of the disk. This can be clearly observed in panel (b) Figure 6.6.

In panel (a) of Figure 6.6 the transition between the two radiative transfer regimes is also clearly demonstrated. Each time a ray passes from the strongly coupled to the adiabatic regime it must be reprojected into the two polarization eigenmodes. If the plasma properties (e.g., density, magnetic field strength or direction, etc.) are not identical to when the polarization had previously frozen out (if at all), this decomposition will necessarily be different. As a result, when propagating the rays backwards, whenever one passes from the adiabatic to the strongly coupled regime, it is necessary to follow *both* polarization eigenmodes in order to ensure the correctness of the radiative transfer. The leads to a doubling of the rays at such points. When integrating the radiative transfer equations forward along the ray, the net intensity is then projected out using equation (5.17). This ray doubling is clearly present in panel (a) of Figure 6.6, where the rays pass into the strongly coupled regime and back

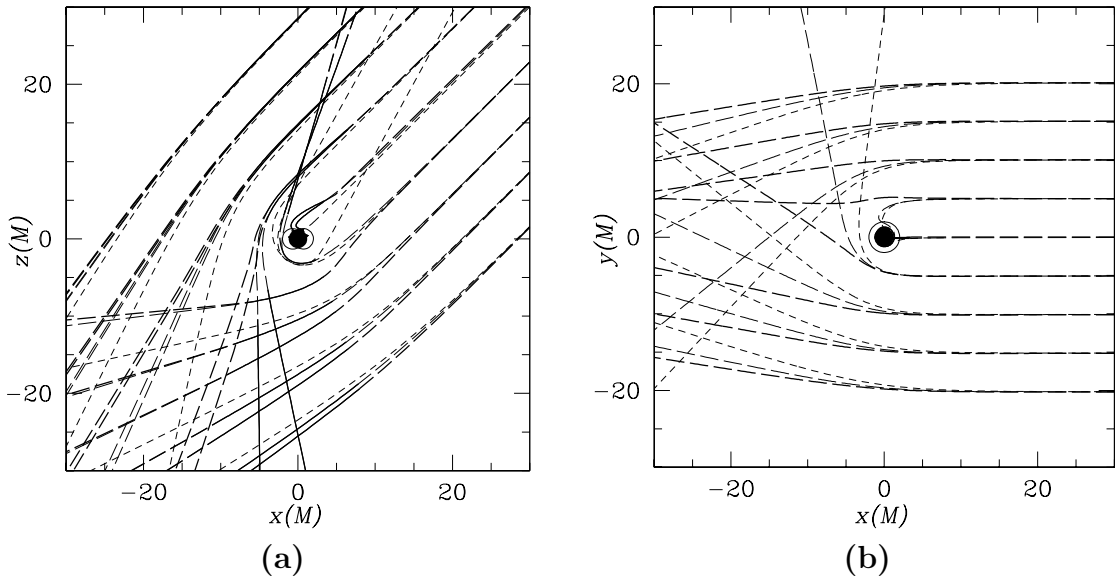

Figure 6.6: Shown in panels (a) and (b) are vertical and horizontal cross sections of rays propagating backwards from an observer located 45° above the equatorial plane. The strongly coupled (adiabatic) regime is denoted by the solid (long-dashed) lines for the ordinary (thin) and extraordinary (thick) polarization eigenmodes. For reference, the null geodesics are drawn in the short dash. In addition, the black hole horizon and the boundary of the ergosphere are also shown.

again as they traverse the evacuated funnel above and below the black hole.

Note that the trajectories of the rays depend upon ω_P/ω_∞ and ω_B/ω_∞ only (given a specified disk and magnetic field structure, of course), where ω_∞ is ω as measured at infinity. Therefore, the paths shown in Figure 6.6 are valid for any density normalization of the disk described in Appendix B as long as ω is adjusted accordingly.

6.5.3 Polarization Maps

In order to demonstrate the formalism described here, polarization maps were computed for the disk model described in Appendix B orbiting a maximally rotating black hole as seen by an observer at infinity elevated to 45° above the equatorial plane. Each map shows Stokes I, Q, U, and V.

As with the ray trajectories, the particular form of the polarization maps only depends upon a few unitless parameters. These necessarily include $\omega_{P\,\max}/\omega$ and

$\omega_{B\,\max}/\omega$ as these define the ray trajectories. In addition, the relative brightness depends upon the optical depth which is proportional to $(\omega_{P\,\max}/\omega)^2(\omega_{B\,\max}/\omega)Mf\omega/c$. As a result if the following dimensionless quantities remain unchanged, the polarization maps shown in the following sections will apply (up to a constant scale factor)

$$\begin{aligned} \frac{\omega_{P\,\max}}{\omega_\infty} &= \frac{4}{3} \\ \frac{\omega_{B\,\max}}{\omega_\infty} &= \frac{4}{3} \\ f\frac{M}{\lambda} &= 2.30 \times 10^3\,. \end{aligned} \tag{6.13}$$

Despite the fact that the form of the polarization maps will remain unchanged if the quantities in equation (6.13) remain constant, the normalization will change by a multiplicative constant in the same way as the source function, namely proportional to ω_∞^2. However, an additional multiplicative factor arises from the solid angle subtended by the source on the sky. As a result, Stokes I, Q, U, and V are all shown in units of

$$\left(\frac{M}{D}\right)^2 m_e\,\omega_{P\,\max}^2\,, \tag{6.14}$$

where D is the distance to the source. This amounts to plotting

$$\frac{kT_B}{m_e c^2}\left(\frac{\omega_\infty}{\omega_{P\,\max}}\right)^2\,, \tag{6.15}$$

where T_B is the brightness temperature of the source.

6.5.3.1 Unpolarized Emission

For the purpose of highlighting the role of refractive plasma effects in the production of significant quantities of circular polarization, Figure 6.7 shows Stokes I, Q, U, and V at $\omega_\infty = 3\omega_{P\,\max}/4$, calculated using the unpolarized emission model described in Section 5.7. Immediately noticeable are the regions of considerable polarization surrounding the black hole. In addition, the outlines of the evacuated funnel above and below the hole are clearly visible.

Differences in the refraction of the two polarization eigenmodes lead to two generic effects: (*i*) the presence of two maxima in the intensity map, each associated with the intensity maxima in a given polarization eigenmode; and (*ii*) a net excess of one polarization, and in particular, circular polarization. The polarization changes rapidly at the edges of the evacuated funnels because the refraction and mode decomposition changes rapidly for modes that just enter the funnel and those that pass wide of it. Note that *all* of the polarization is due *entirely* to refractive plasma effects in this case. The integrated values for the Stokes parameters are $I = 1.3$, $Q = -9.4 \times 10^{-4}$, $U = 4.9 \times 10^{-5}$, and $V = 6.2 \times 10^{-2}$, demonstrating that there does indeed exist a significant net circular polarization.

Figure 6.7 may be compared with Figure 6.8 in which Stokes I, Q, U, and V are shown at $\omega_\infty = 3\omega_{P\,\max}$ for the same unpolarized emission model. In the latter case the refractive effects are significantly repressed. This demonstrates the particularly limited nature of the frequency regime in which these types effects can be expected to occur. In this case there still does exist a net circular polarization, now with integrated values $I = 1.0$, $Q = -4.8 \times 10^{-6}$, $U = 2.4 \times 10^{-7}$, and $V = 1.2 \times 10^{-3}$.

6.5.3.2 Polarized Emission

In general, synchrotron emission will be polarized. As a result it is necessary to produce polarization maps using the emission model described in sections 5.5 and 5.6. In this case a net polarization will exist even in the absence of any refraction. In order to compare the amount of polarization generated by refractive effects to that created intrinsically, Figure 6.9 shows Stokes I, Q, U, and V calculated using the polarized emission model and ignoring refraction (i.e., setting the rays to be null geodesics) for $\omega_\infty = 3\omega_{P,\max}/4$. Strictly speaking, this is a substantial overestimate of the polarization. This is because, in the absence of refraction, in principle it is necessary to include Faraday rotation and conversion in the transfer effects considered. As a result of the high plasma density and magnetic field strengths, the Faraday rotation and conversion depths for this system should be tremendous for non-refractive rays, effectively depolarizing any emission.

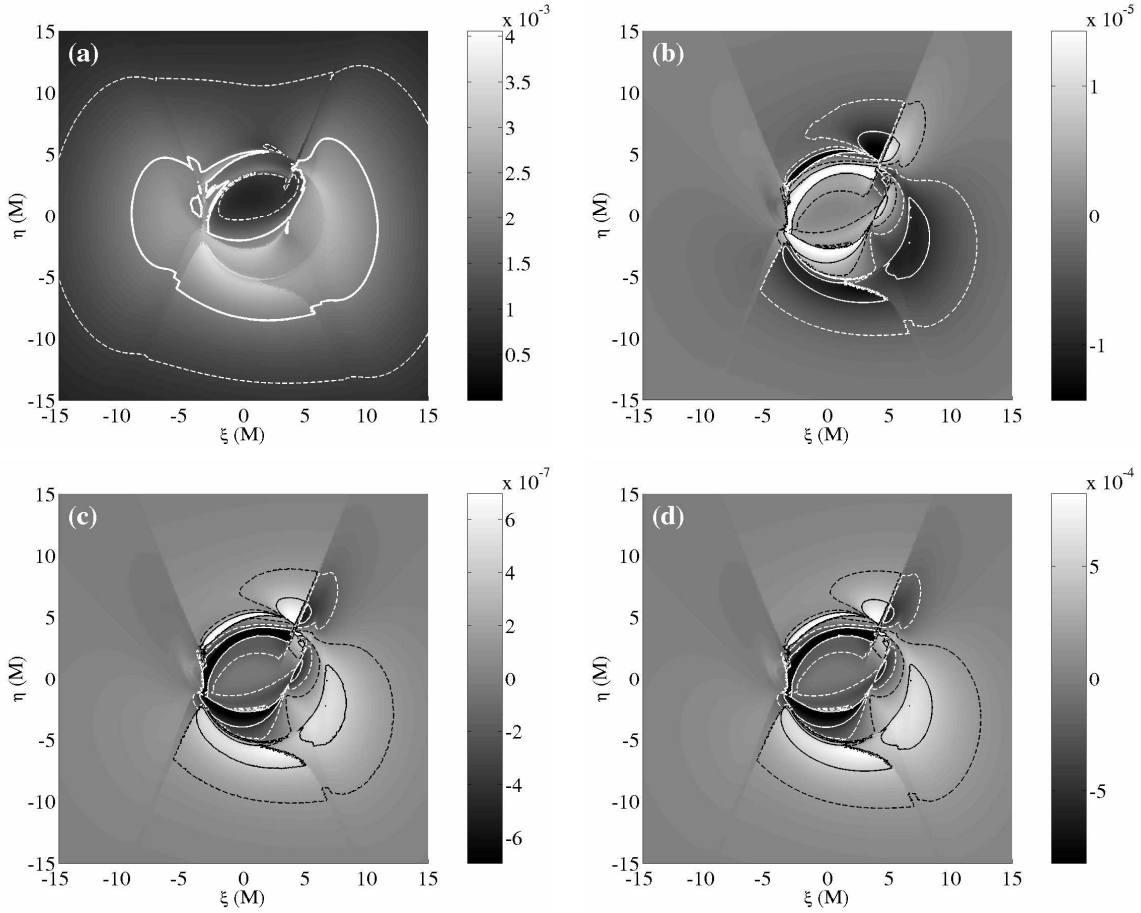

Figure 6.7: Stokes I, Q, U, and V per unit M^2 are shown in panels (a), (b), (c), and (d), respectively, for the unpolarized emission mechanism described in Section 5.7 and the disk model described in Appendix B orbiting a maximally rotating black hole from a vantage point 45° above the equatorial plane at the frequency $\omega_\infty = 3\omega_{P,\max}/4$. The contour levels are at 0.2 (dashed) and 0.6 (solid) of the maximum values shown on the associated colorbars. The integrated fluxes over the region shown are $I = 1.3$, $Q = -9.4 \times 10^{-4}$, $U = 4.9 \times 10^{-5}$, and $V = 6.2 \times 10^{-2}$. All fluxes are in units of $(M/D)^2 m_e \omega_{P\,\max}^2$ as discussed above equation (6.14).

In comparison to Figures 6.7 and 6.8, the general morphology of the polarization maps are substantially different. In addition, the amount of linear polarization is significantly larger, having an integrated value of over 60% compared to less than 0.1% in Figure 6.7 and less than 10^{-3}% in Figure 6.8. This calculation can be compared to that done by Bromley et al., 2001. In both it was assumed that the rays were null geodesics. In both Faraday rotation/conversion were neglected (in Bromley et al.,

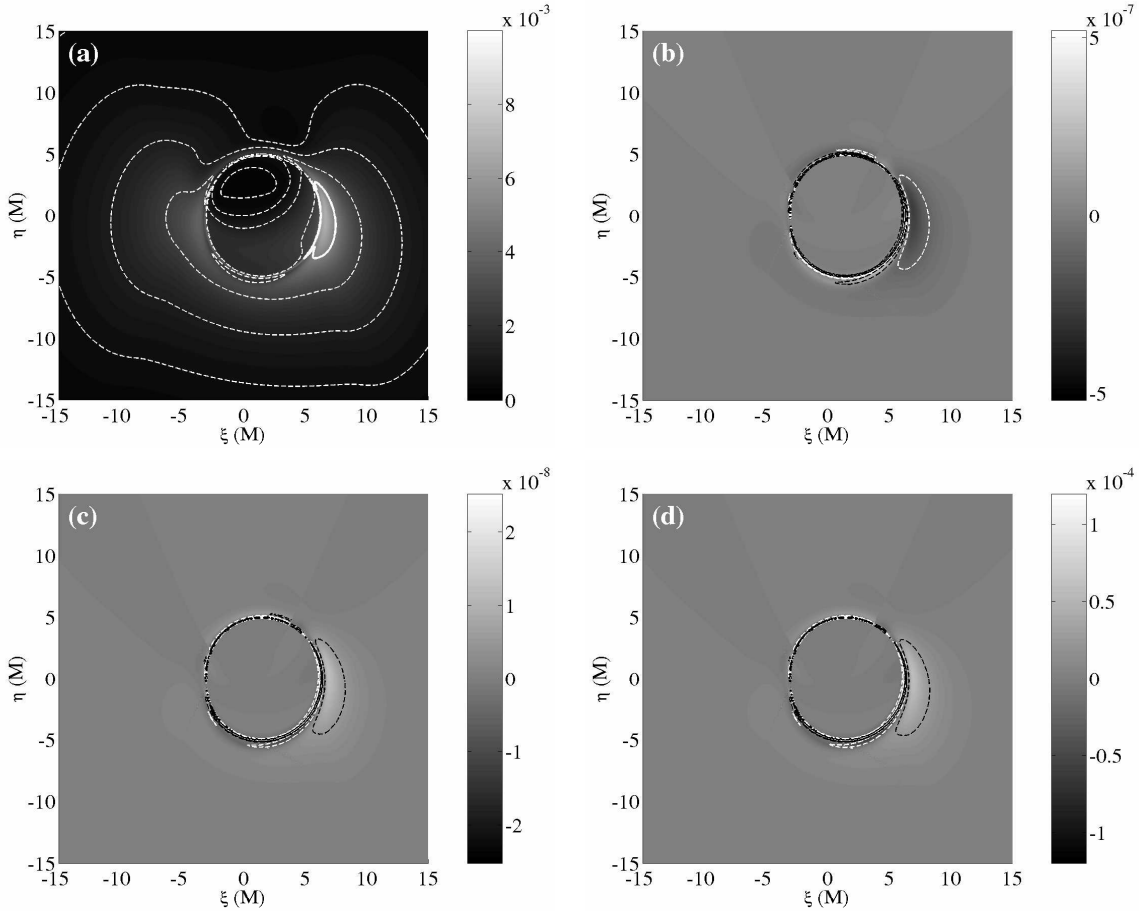

Figure 6.8: Same as Figure 6.7 except with $\omega_\infty = 3\omega_{P\,\max}$. The integrated fluxes over the region shown are $I = 1.0$, $Q = -4.8 \times 10^{-6}$, $U = 2.4 \times 10^{-7}$, and $V = 1.2 \times 10^{-3}$. All fluxes are in units of $(M/D)^2 m_e \omega_{P\,\max}^2$ as discussed above equation (6.14).

2001 because for their disk model it was assumed to be negligible.) However, in Bromley et al., 2001 it was also assumed that the radiative transfer could always be done in the adiabatic regime. As a result, the net polarization was determined entirely by the emission mechanism. However, as discussed in Section 5.1 this is only possible in the strongly coupled regime. In this case, the dichroic terms in equation (5.39) provide the source of circular polarization, even in the absence of a circularly polarized emission, resulting from the different absorption properties of the two polarization eigenmodes. This is what leads to the presence of circular polarization in Figure 6.9 but not in Bromley et al., 2001. In this case, the integrated values of the Stokes parameters are $I = 1.1$, $Q = 6.0 \times 10^{-1}$, $U = -4.9 \times 10^{-3}$, and $V = 6.9 \times 10^{-2}$. The

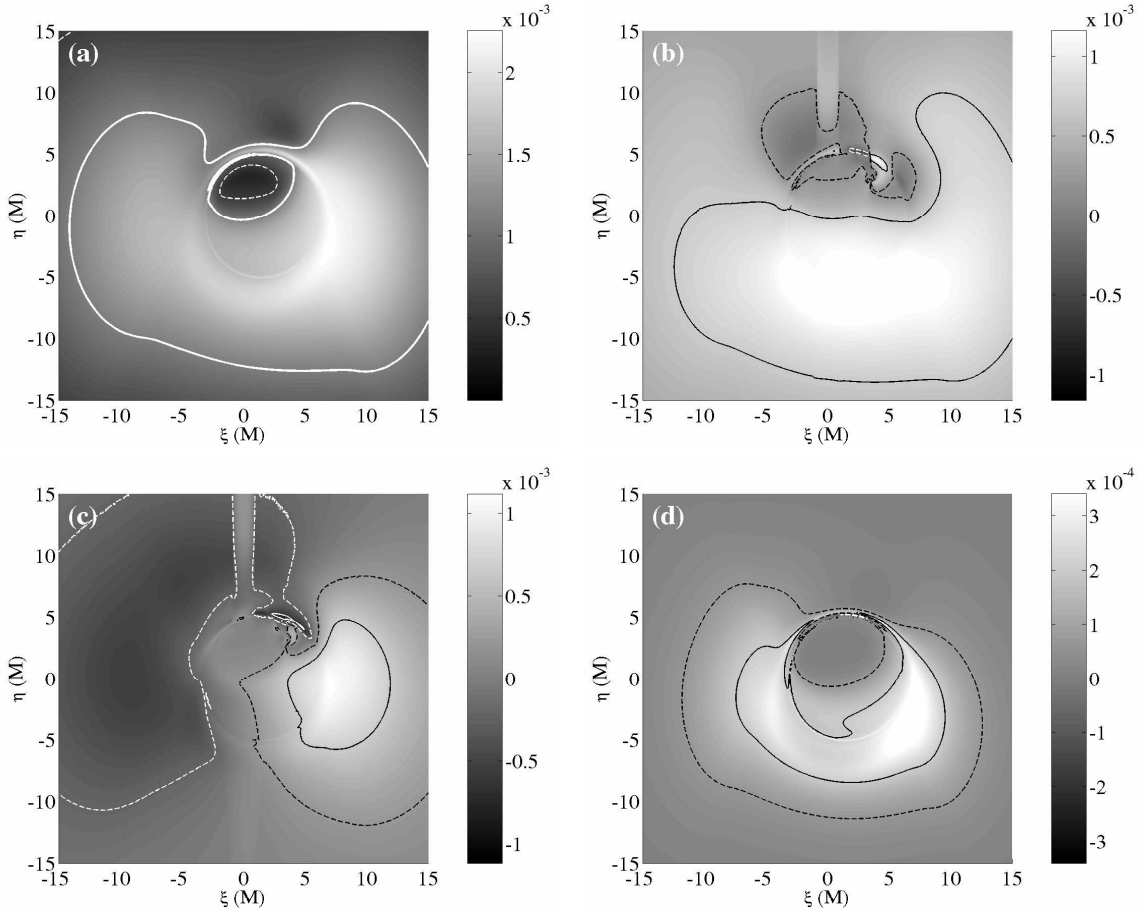

Figure 6.9: Same as Figure 6.7 except using the polarized emission mechanism (described in Sections 5.5 and 5.6) and ignoring refractive plasma effects. The integrated fluxes over the region shown are $I = 1.1$, $Q = 6.0 \times 10^{-1}$, $U = -4.9 \times 10^{-3}$, and $V = 6.9 \times 10^{-2}$. All fluxes are in units of $(M/D)^2 m_e \omega_{P\,\max}^2$ as discussed above equation (6.14).

vertical feature directly above the black hole in panels (b) and (c) is associated with the rapid decrease in the magnetic field strength in the evacuated funnel above and below the black hole and are due to the geometric transfer effect discussed in Section 5.1.2.

Finally, in Figure 6.10, both refractive effects and the polarized emission mechanism are included (again at $\omega_\infty = 3\omega_{P,\max}/4$). Many of the qualitative features of Figure 6.7 still persist. The integrated values of the Stokes parameters are $I = 1.3$, $Q = -2.2 \times 10^{-3}$, $U = 1.2 \times 10^{-4}$, and $V = 1.4 \times 10^{-1}$. While the intrinsic polarization

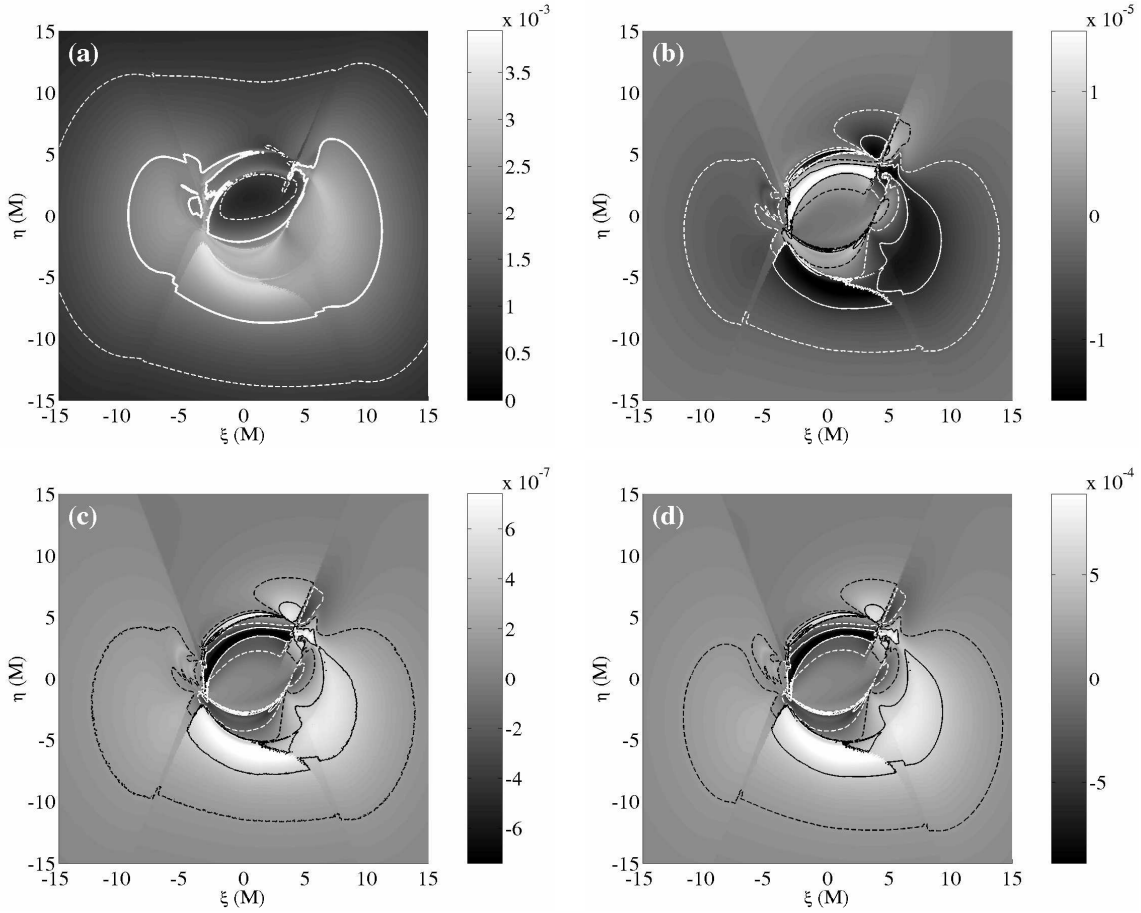

Figure 6.10: Same as Figure 6.9 except including refractive plasma effects. The integrated fluxes over the region shown are $I = 1.3$, $Q = -2.2 \times 10^{-3}$, $U = 1.2 \times 10^{-4}$, and $V = 1.4 \times 10^{-1}$. All fluxes are in units of $(M/D)^2 m_e \omega_{P\,\max}^2$ as discussed above equation (6.14).

in the emission does make a quantitative difference, it is clear that in this case the generic polarimetric properties are dominated by the refractive properties. This is most clearly demonstrated by noting the strong suppression of linear polarization. In Figure 6.10 the linear polarization fraction is less than 0.2% as compared with nearly 60% in Figure 6.9.

6.5.4 Integrated Polarizations

Figure 6.11 shows the Stokes parameters as a function of frequency for when only polarized emission is considered, only refractive plasma effects are considered, and

when both are considered. There are two notable effects due to refraction: (*i*) the significant suppression of the linear polarization, and (*ii*) the large amplification of circular polarization. The linear polarization is decreased by at least two orders of magnitude, and in particular, at least two orders of magnitude less than the final circular polarization. On the other hand, the circular polarization is more than doubled at its peak, and increases by many orders of magnitude at higher frequencies. Nonetheless, by $\omega_\infty = 10\omega_{P\,\mathrm{max}}$, both polarizations are less than one tenth of their maxima. As a result, it is clear that this mechanism is restricted to approximately one decade in frequency, centered about $\omega_{P\,\mathrm{max}}$.

Figure 6.12 shows the circular polarization fraction as a function of frequency for the same set of cases that were depicted in the previous figure. As can be seen in Figure 6.11, the circular and linear polarization spectral index are approximately equal, and both are softer than that of the total intensity. The result is a decreasing circular polarization fraction with increasing frequency.

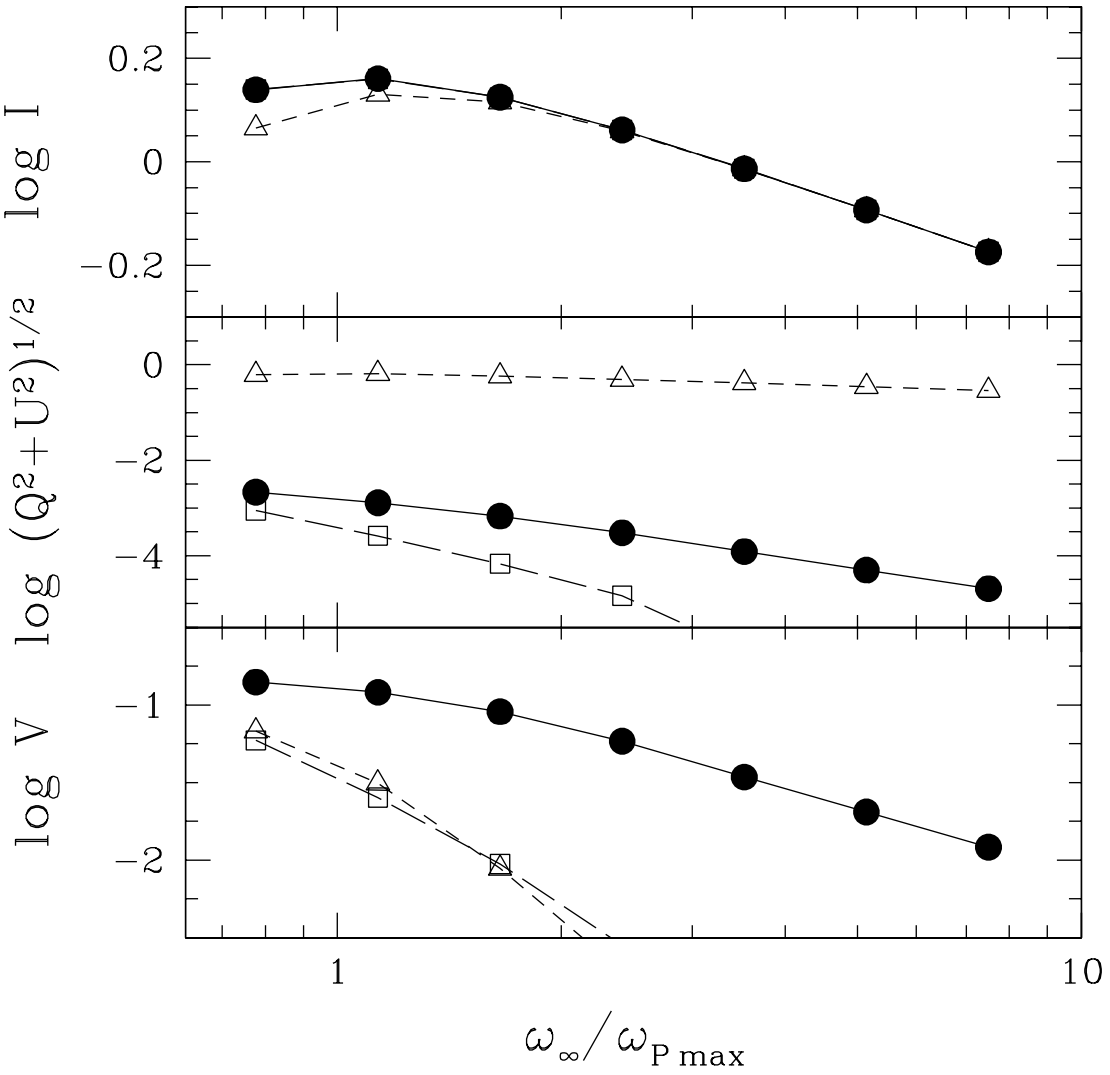

Figure 6.11: The log of the integrated intensity, total linear polarization, and circular polarization are shown as a function of the observation frequency at infinity for when only polarized emission is considered (open triangles), only refractive plasma effects are considered (open squares), and when both are considered (filled circles). As in Figures 6.6-6.10, the disk model described in Appendix B orbiting a maximally rotating black hole is viewed from a vantage point 45° above the equatorial plane. All fluxes are in units of $(M/D)^2 m_e \omega^2_{P\,\max}$ as discussed above equation (6.14).

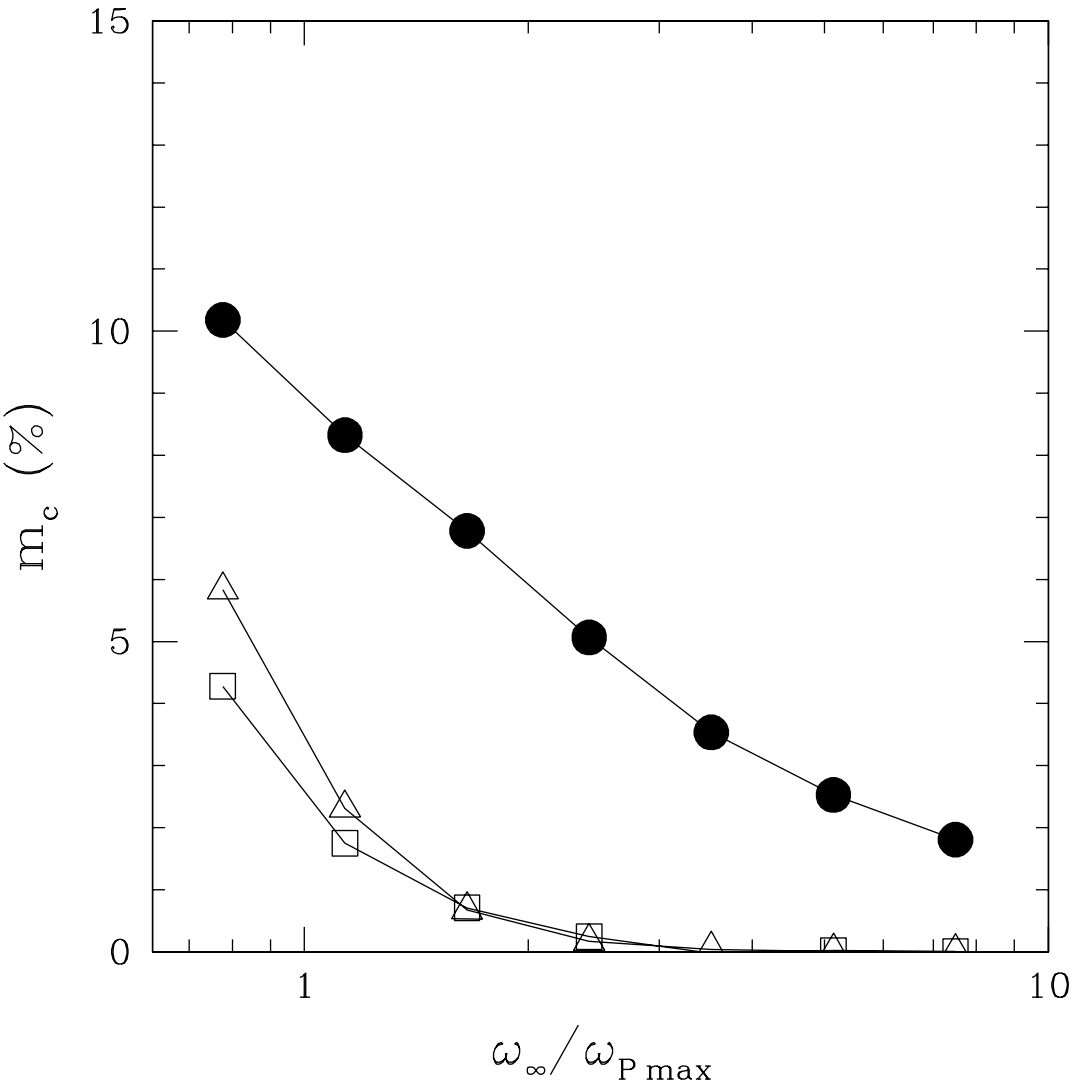

Figure 6.12: Shown is the circular polarization fraction as a function of the observation frequency at infinity for when only polarized emission is considered (open triangles), only refractive plasma effects are considered (open squares), and when both are considered (filled circles). As in Figures 6.6-6.11, the disk model described in Appendix B orbiting a maximally rotating black hole is viewed from a vantage point 45° above the equatorial plane.

Chapter 7

Application to Accreting Black Hole Systems

7.1 Galactic Nuclei

7.1.1 Sgr A*

The primary motivation for this project was to explain the observation of circular polarization in the Galactic center. As has been demonstrated in the previous chapter, refraction is capable of producing circular polarization at frequencies comparable with ω_P and ω_B near the horizon. In Sgr A* the circular polarization has been observed in the range $\nu \simeq 5$–15 GHz. Therefore, if this polarization is produced by refraction, this implies in general that ν_P is greater than 5 GHz.

More constraining is the magnitude of the circularly polarized flux. Because the refractive mechanism discussed in the previous chapter only operates near the horizon, the entirety of the circularly polarized flux must be produced in its vicinity ($\sim 10^{-2}$ Jy). The resulting brightness temperature is then,

$$T_b = 2 \times 10^{14} \left(\frac{r}{M}\right)^{-2} \left(\frac{\nu}{1\,\mathrm{GHz}}\right)^{-2} \mathrm{K}\,, \tag{7.1}$$

where $D \simeq 8\,\mathrm{kpc}$ was used, and r is the radius of the emitting region. Therefore, for an emitting region with a radius of $10M$, this lies below the Compton limit. If the flux is due to synchrotron emission from a power law electron distribution (presumably

accelerated via shocks), this produces a brightness temperature on the order of

$$T_{\rm synch} \simeq \frac{m_e c^2}{k}\sqrt{\frac{\omega}{\omega_B}} = 6\times 10^9 \sqrt{\frac{\omega}{\omega_B}}\,{\rm K}\,. \tag{7.2}$$

Therefore, for $\omega \simeq \omega_B$, the condition that $T_b = T_{\rm synch}$ corresponds to a constraint upon the size of the emitting region of

$$r \gtrsim 20M \left(\frac{\nu}{1\,{\rm GHz}}\right)^{-1} \left(\frac{\omega_B}{\omega}\right)^{1/4}\,, \tag{7.3}$$

which is not unreasonable (the inequality depends upon whether or not the region is optically thick). Following the equipartition arguments discussed in Appendix B.2, ω_B can be expected to be on the order of ω_P.

The above argument assumes that the polarization fraction is near unity. However, this is in general not the case. For the specific disk model discussed in Appendix B, the results of Section 6.5 may be appropriated given their generality. The maximum typical circularly polarized flux determined in that section is on the order of

$$V_\nu \simeq 0.9 \left(\frac{M}{D}\right)^2 m_e \omega_{P\,\rm max} \simeq 1.4\times 10^{-3} \left(\frac{\nu_{P\,\rm max}}{1\,{\rm GHz}}\right)^2\,{\rm mJy}\,, \tag{7.4}$$

(note that this is V_ν not V_ω). If the *maximum* plasma frequency is on the order of 30 GHz, this produces a circularly polarized flux on the order of 0.5 mJy as observed.

Figure 6.11 is reproduced with units appropriate for the Galactic center in Figure 7.1. Note that the spectra for the total intensity and the linear polarization need not correspond to those observed since in these cases the majority of the flux will arise much further out. However, because in this model the circular polarization is created in the vicinity of the black hole, the circular polarized spectrum should be compared to observations. In this case, there are two notable issues. Firstly, the polarized flux decreases by less than an order of magnitude from its maximum near 45 GHz to 200 GHz. Nonetheless, this will be mitigated by the increase in intensity for further out in the accretion flow at these frequencies. In addition, because the high degrees in circular polarization appear to be associated with a flaring state (as

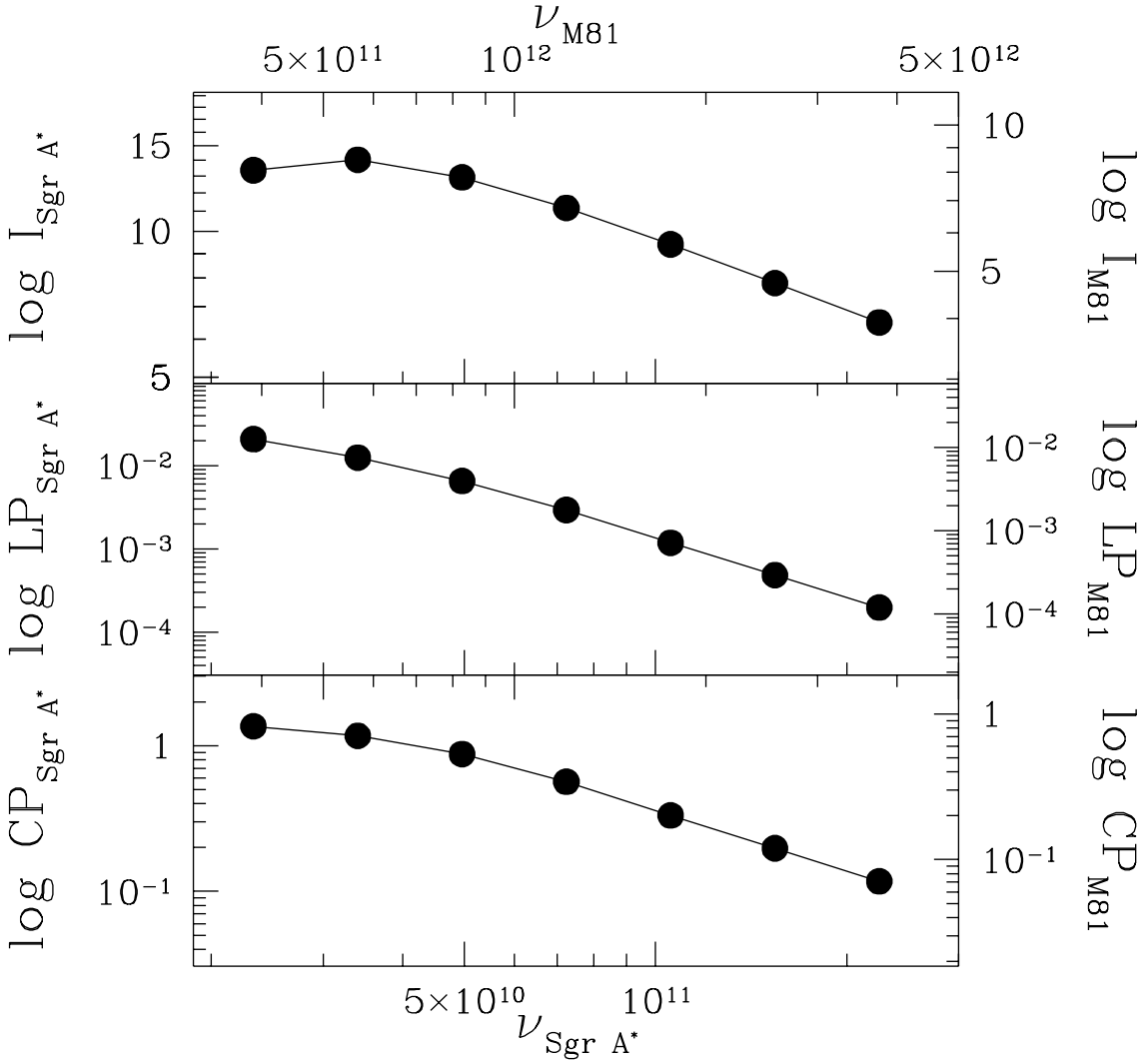

Figure 7.1: The log of the integrated intensity, total linear polarization, and circular polarization are shown as a function of the observation frequency at infinity. The bottom and left axis labels are for Sgr A*with $\nu_{P\,\rm max} = 30\,$GHz, while the top and right axis labels are for M81 with $\nu_{P\,\rm max} = 500\,$GHz. The disk model described in Appendix B orbiting a maximally rotating black hole is viewed from a vantage point 45° above the equatorial plane. All fluxes are in mJy.

opposed to quiescent state with a significantly lower polarization), it is possible that these predicted high degrees of circular polarization at high frequencies have simply not yet been observed. This would also mitigate the need for such high densities, implying that the high circular polarization states are associated with periods of in-

creased accretion. Secondly, at no point in Figure 7.1 does the circularly polarized flux increase. This is due to a combination of a decrease refractive effects and emissivities at higher frequencies. However, the circular polarization can be expected to decrease at lower frequencies as well (the beginning of the turn over is already apparent) as the accretion flow becomes optically thick and thus masks effects occurring near the horizon. Therefore, the fact that $\nu_P \simeq 30\,\mathrm{GHz}$ is marginally higher than the frequencies at which circular polarization has been measured is not particularly surprising. The $\nu \ll \nu_P$ case was not addressed here due to concerns regarding the way in which the cyclotron resonance was dealt with. However, in principle, this can be extended to this regime as well.

If refraction is responsible for the observed circular polarization, this places strong constraints upon the Galactic center environment. In order to assess the viability of this mechanism, it is necessary to consider the limits placed by other observations. The first of these is the sub-mm emission, which is presumed to arise from the innermost portions of the accretion flow. If the electrons can emit efficiently, the limiting factor is their coupling to the ions. If this primarily occurs via Coulomb scattering, the approximate volumetric heating rate of relativistic electrons is given by

$$\dot{E}_e \simeq m_e c^2 \frac{m_e}{m_p} \sigma_T c \ln\Lambda n_e^2 \,, \tag{7.5}$$

where σ_T is the Thomson cross section and Λ is the cutoff of the Coulomb integral (typically $\ln\Lambda \sim 10$–20), (see, e.g., Stepney, 1983). The resulting flux is then given by

$$F_\nu \simeq \frac{2\pi}{3}\frac{M^3}{D^2}\left(\frac{r}{M}\right)^3 \frac{\dot{E}_e}{\nu} \simeq 8\times10^{-21}\left(\frac{n_e}{\mathrm{cm}^{-3}}\right)^2\left(\frac{r}{M}\right)^3\left(\frac{\nu}{10^{12}\,\mathrm{Hz}}\right)\,\mathrm{Jy}\,. \tag{7.6}$$

Hence, in order to produce a typical sub-mm flux of 10 Jy, the electron number density is approximately

$$n_e \gtrsim 3.5\times10^{10}\left(\frac{r}{M}\right)^{-3/2}\,\mathrm{cm}^{-3}\,, \tag{7.7}$$

where the inequality is due to the fact that the electrons do not necessarily radiate

all of their energy. This corresponds to a maximum plasma frequency on the order of $\nu_P \simeq 2\,\mathrm{GHz}$. This is approximately an order of magnitude lower than what is required by the refractive mechanism.

The second significant observation is that of bipolar X-ray lobes about the Galactic center. The presence of two X-ray lobes (presumably powered by winds off of a disk) which require an energy infusion rate of $\sim 10^{39}$ erg/s, imply an accretion rate of approximately 10^{20} g/s (despite an available mass supply of $\sim 10^{22}$ g/s). Therefore, with $\dot{M} \simeq 4\pi M^2 m_p c\, n_e \beta (r/M)^2$, this implies that

$$n_e \simeq 6.4 \times 10^8 \beta^{-1} \left(\frac{M}{r}\right)^2 \mathrm{cm}^{-3}\,, \tag{7.8}$$

or in terms of the plasma frequency,

$$\nu_P \simeq 0.2 \frac{M}{r\sqrt{\beta}}\ \mathrm{GHz}\,. \tag{7.9}$$

Therefore, for $\nu_P \simeq 2$, this requires $\beta \simeq 0.01(M/r)^2$. Using an α prescription for the disk viscosity (although this is almost certainly not a good approximation in this case),

$$\beta \simeq \alpha \frac{c_s^2}{c v_\phi} \simeq \alpha \Gamma \frac{k T_i}{m_p c^2}\,, \tag{7.10}$$

where c_s is the sound speed in the disk, v_ϕ is its azimuthal velocity, Γ is the adiabatic index, and T_i is the ion temperature. Therefore,

$$T_i \simeq \frac{m_p c^2}{\alpha \Gamma k} \beta \simeq 6 \times 10^{10} \alpha^{-1} \left(\frac{M}{r}\right)^2 \mathrm{K}\,, \tag{7.11}$$

and hence for α on the order of 0.3 this gives ion temperatures in the innermost regions on the order of $10^{11}\,\mathrm{K}$, which are reasonable.

Despite the success in producing the circular polarization, and the conditional success in reproducing its gross features, it has a number of additional implications. The first is that the accretion disk must be significantly inclined. A possible X-ray jet, itself aligned with magnetic filaments at 30 pc, may suggest that the disk is aligned

with the Galactic plane. This is in contrast to the molecular torus locate at about 3 pc which appears to be inclined by approximately 60° (although both conditions may be satisfied by a disk inclined towards us). The second is that since the plasma frequency implied by the sub-mm emission is an order of magnitude too low, if refraction is producing the circular polarization, it cannot result from the steady-state accretion. However, since the circular polarization appears to be associated with a flaring state, it may be associated with episodes characterized by high accretion rates. Finally, the higher frequency emission must arise via optically thin emission from a larger region of the disk, with the resulting spectrum then due to the disk's radial structure. This may already be in conflict with recent measurements of the intrinsic source size at 7mm (Bower et al., 2004).

7.1.2 M81

M81 is similar to the Galactic center in many respects, including the presence of a relatively flat, inverted spectrum at GHz frequencies, lack of significant linear polarization, and the presence of circular polarization. As in Sgr A*, the total circularly polarized flux in M81 is on the order of 1 mJy. However, M81 is approximately 450 times further away than Sgr A* (3.6 Mpc) but only about 20 time larger ($\sim 7 \times 10^7 M_\odot$), significantly reducing its solid angle on the sky (Devereux et al., 2003). This is mitigated somewhat by the fact that since the normal is inclined at approximately 14° from the line of sight, it is nearly face on, and hence the fractional polarization will increase, although this will alter the emission as well. In addition, the X-ray luminosity, and hence the mass accretion rate, is approximately an order of magnitude higher, relaxing somewhat the constraints upon plasma densities near the central black hole.

Following equation (7.4), for M81

$$V_\nu \simeq 3.4 \times 10^{-6} \left(\frac{\nu_{P\,\max}}{1\,\mathrm{GHz}}\right)^2 \mathrm{mJy}\,. \tag{7.12}$$

Therefore, in order to provide mJy fluxes, $\nu_{P\,\max} \sim 500\,\mathrm{GHz}$, which is quite high. This may be decreased to 50 GHz, which is on the order of what is found for Sgr A*,

if the mass of M81 is increased by an order of magnitude. Due to the presence high non-circular velocities in the central 10 pc of M81, the degeneracy between mass and inclination is difficult to break, and hence the mass is currently poorly constrained. Thus, though perhaps not likely, it is nonetheless possible that current mass estimates of M81 are an order of magnitude low. The results from the previous sections are also shown for units appropriate for M81 in Figure 7.1.

7.1.3 Blazars

As the application to M81 suggests, there will be a brightness temperature problem for blazars. Consider, for example, the closest blazar showing circular polarization at at least the 5σ level in the survey by Rayner et al. (2000), PMN 1522-2730. This source is at least 7.7×10^2 Mpc away and shows a circularly polarized flux on the order of 7 mJy. If the entirety of the circularly polarized emission is to originate within $15M$, this requires a brightness temperature on the order of 10^{16} K. This should be compared with the maximum of approximately 10^{13} K set by releasing all of the gravitational binding energy of the ions. Therefore, it is clear that the refractive mechanism can not applied in the scheme discussed thus far to blazars. Hence, if the refractive mechanism is responsible for generating the circular polarization in LLAGN, these systems must be qualitatively different then blazars.

7.2 Application to X-ray Binaries

As discussed in Section 1.2, X-ray binaries can provide an analogous environment to LLAGN. However, due to the change in mass scale, accretion rate, and radiative efficiency, it is necessary to rescale the frequencies at which interesting effects may occur. As shown in Section 1.2, the plasma frequency and cyclotron frequencies should scale roughly as

$$\omega_P \sim \omega_B \propto \sqrt{\frac{\epsilon}{\eta M}}\,, \tag{1.6}$$

where ϵ is the luminosity in units of the Eddington rate and η is the radiative efficiency. Therefore, for a $10M_\odot$ XRB with a 0.01 Eddington luminosity and a radiative efficiency on the order of 0.01, this implies that

$$\omega_P,\, \omega_B \sim 4 \times 10^4\,\mathrm{GHz}\,, \tag{7.13}$$

which is in the near infrared. For an XRB as radiatively inefficient as the Galactic center ($\eta \sim 10^{-5}$), this gives $\omega_P,\, \omega_B \sim 1 \times 10^7\,\mathrm{GHz}$ which is in the ultraviolet/soft X rays.

Unfortunately, while XRB's are typically located at similar distances as the Galactic center, the horizon is five orders of magnitude smaller. Therefore, the integrated flux from the innermost $15M$, which decreases roughly as $M^{-1/2}$ for self-absorbed synchrotron sources, will be considerably smaller. Figure 6.11 is reproduced in Figure 7.2 with units appropriate for radiatively efficient and inefficient XRB's. Nonetheless, as demonstrated by the radiatively inefficient XRB, it is clearly possible to generate an observable circularly polarized flux, frequently larger than that in the Galactic center.

Figure 7.3 shows the regions in which the refractive mechanism may be observed as a function of M and $\dot{M}$. The Eddington limit for various values of ϵ/η and contours of the frequencies at which refractive effects will become important are shown. Because the local plasma density depends upon the infall velocity, the 10 GHz contour is also shown for $\beta = 10^{-3}$ and 10^{-6}. For reference, regions that are accesible to SIRTF and the VLBA are shown for these two infall velocities and for objects at 1 kpc and 8 kpc. While SIRTF does not have any polarization capabilities, it does provide insight into what may be acheived using current technologies. The Eddington limit places a restriction upon the detectability of polarization at high frequency from stellar mass black holes. The position of the Galactic center and the XRBs with known masses closer than 8 kpc in table 1.2 are also shown, assuming a radiative efficiency of 10%. Depending upon the radial velocity of the accretion flow, it may be feasible for experiments with present day sensitivities to measure a polarized signal from

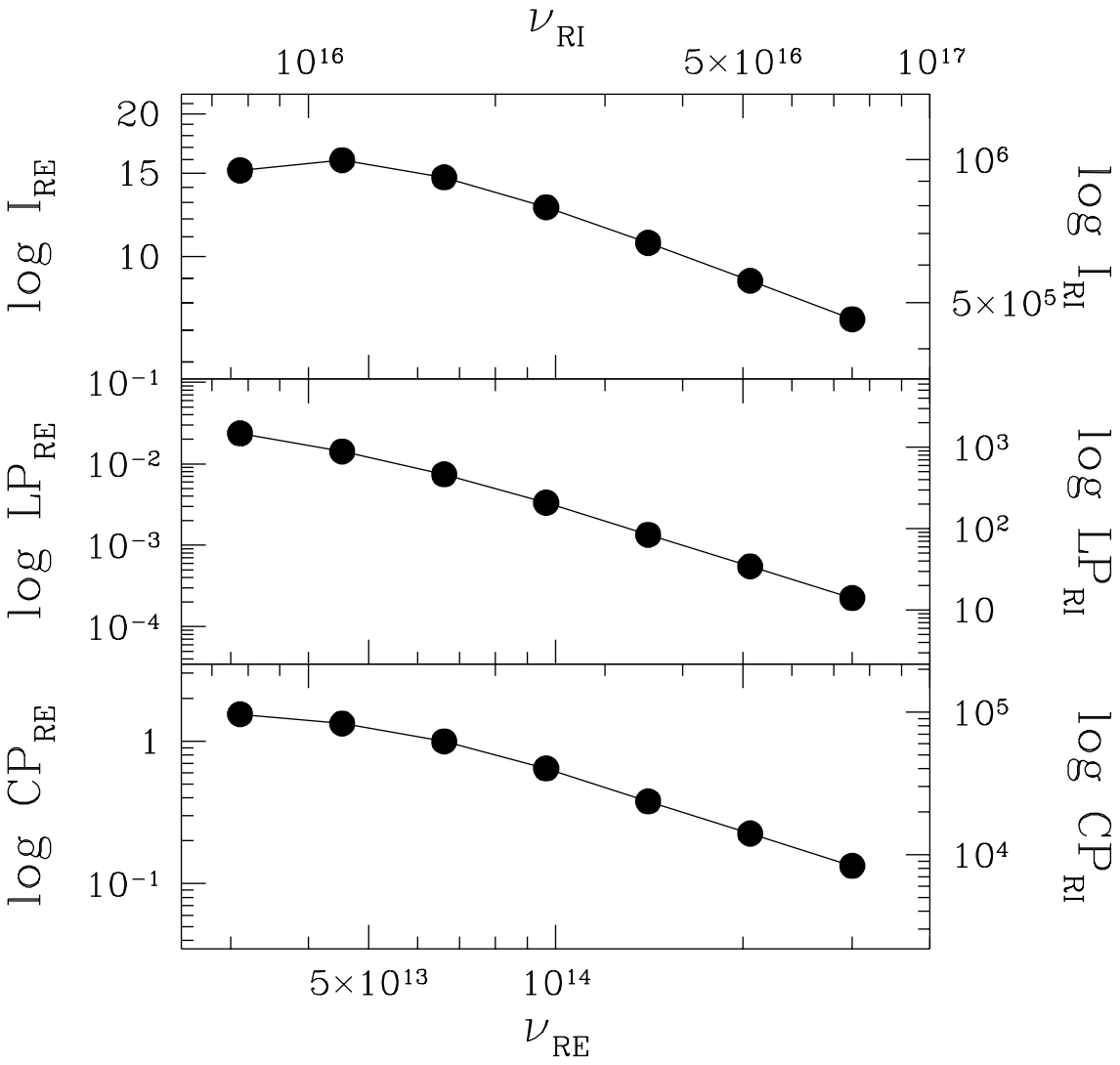

Figure 7.2: The log of the integrated intensity, total linear polarization, and circular polarization are shown as a function of the observation frequency at infinity. The bottom and left axis labels are for a radiatively efficient XRB with $\nu_{P\,\max} = 4 \times 10^4\,$GHz, while the top and right axis labels are for a radiatively inefficient XRB with $\nu_{P\,\max} = 1 \times 10^7\,$GHz. Both are at 3 kpc. The disk model described in Appendix B orbiting a maximally rotating black hole is viewed from a vantage point 45° above the equatorial plane. All fluxes are in mJy.

nearyby XRBs. As yet there have been no efforts to measure circular polarization in the infrared. Hence, this provides a motivation for conducting such investigations.

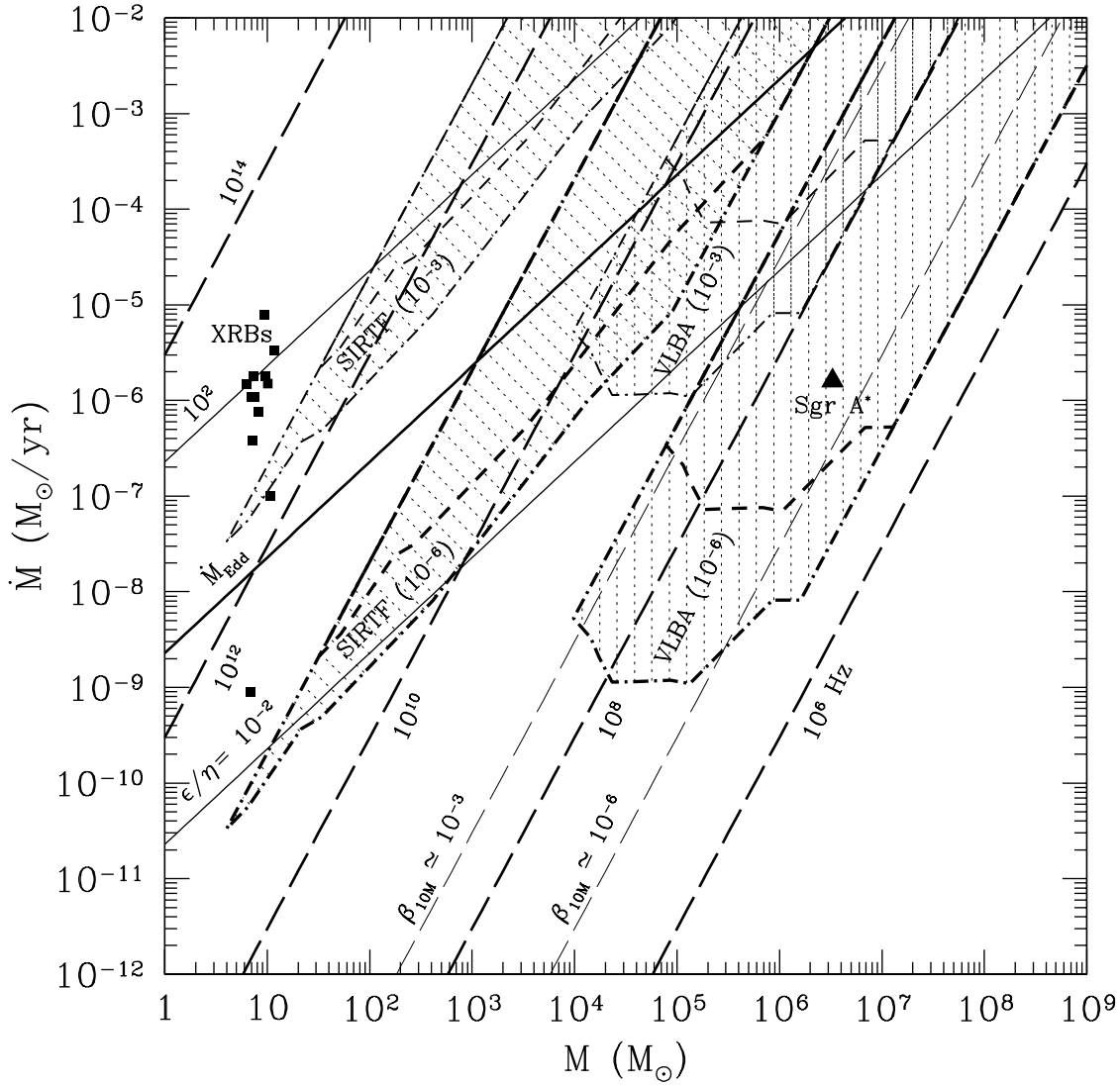

Figure 7.3: Limits upon the refractive mechanism in the M–$\dot{M}$ plane are shown. The thick solid line shows the Eddington limit when $\epsilon/\eta = 1$. For reference, $\epsilon/\eta = 10^2$ and 10^{-2} are also shown by the thin solid lines. The thick long dashed lines show curves of constant $\nu_{P\,\max}$ (assuming that the infall velocity at $10M$ is c) and hence where refractive effects may be expected to appear in the spectrum. In addition for 10^{10} Hz, the curves of constant $\nu_{P\,\max}$ are shown by the thin long dashed line for the cases when the inflow velocity at $10M$ is $10^{-3}c$ and $10^{-6}c$. Regions accessible to SIRTF and the VLBA are denoted by the shaded regions for the two inflow velocities. The thick dashed-dot border corresponds to an object at 1 kpc, while the thick short dashed border corresponds to an object at 8 kpc. Lastly, the position of Sgr A* and the XRBs closer than 8 kpc are shown for reference. For the XRBs it was assumed that $\eta \simeq 10\%$. The polarized emission is assumed to arise from the disk model described in Appendix B orbiting a maximally rotating black hole is viewed from a vantage point 45° above the equatorial plane.

Part III

Radiative Transfer Through Tangled Magnetic Fields

Polarized radiative transfer through self-absorbed synchrotron sources has been studied in detail (see, e.g., Jones & O'Dell, 1977b,a; Sazonov, 1969; Sazonov & Tsytovich, 1968). However, these have focused upon homogeneous media or assumed the quasi-longitudinal limit (the external magnetic field is nearly along the ray, or equivalently, the electric field vector is nearly transverse to the ray). Efforts to understand the radiative transfer have typically been focused on Faraday rotation (Enßlin & Vogt, 2003; Ruszkowski & Begelman, 2002, etc.). As more circular polarization observations become available Faraday conversion has been discussed as well (see, e.g., Jones & O'Dell, 1977b,a; Beckert & Falcke, 2002; Macquart, 2002). Both of these are directly due to the anisotropic nature of the dielectric tensor introduced by the presence of the magnetic field.

Geometric phase (also called Berry phase or anholonomic phase) effects result from variations in the basis vectors describing some system. In the context of anisotropic media, these basis vectors are simply the polarization eigenmodes, which may vary along the line of sight. An example that has received some recent attention is the effect associated with the rotation of the polarization plane about the line of sight (see, e.g., Enßlin, 2003). Previously, these had been discussed in terms of the electric field vectors (see, e.g., Hodge, 1982; Budden & Smith, 1976). Kubo & Nagata, 1983 demonstrate how to derive the radiative transfer equation from a propagation equation for the electric field vector in the limit of weak inhomogeneity. However, neither of these treatments are in a form that is readily applicable to astrophysical sources.

Here we derive the degree and frequency dependence of circular polarization that is due to tangled magnetic fields. We present a qualitative discussion of the mechanism in Section 8.1, discuss the source of the geometric terms (Section 8.2), the pure transfer problem (Section 8.3), and the transfer problem when *in situ* emission is considered (Section 8.4). We then discuss the frequency dependence and regime of validity in Section 8.5 and apply this mechanism to the radio polarization observations of the Galactic center in Section 9.1. While we focus upon the propagation through a stationary medium, additional interesting effects due to dynamical considerations are also possible. As a result, the formalism presented here may not apply near the

inner edge of an accretion flow.

Chapter 8

Polarized Radiative Transfer Through Tangled Magnetic Fields

8.1 Qualitative Discussion of the Mechanism

The effects discussed in this part arise from alterations in the polarization eigenmodes that occur due to changes in the physical conditions along the line of sight. While in principle these may include variations in the magnetic field strength and plasma density, the dominant effect is the rotation of orientation the magnetic field. A possible environment in which this might arise is an accretion disk in which differential rotation has produced a net magnetic helicity (presumably due to the magneto-rotational instability (MRI)), shown schematically for two possible mechanisms in Figure 8.1. Rotation of the magnetic field orientation about the line of sight leads to a rotation of the polarization ellipses of the plasma eigenmodes, and a subsequent transfer of power from one mode to the other, as depicted in Figure 8.2. This effect explicitly enters the radiative transfer equations in a manner analogous to Faraday rotation. If the local emission process is synchrotron emission, the resulting Stoke's Q can be transformed into Stoke's U via this process, and then into Stoke's V via Faraday conversion. Because the "extra" Faraday rotation does not depend upon the sign of the magnetic field, it will not depolarize as a result of field reversals. Furthermore, since the length scales over which this effect occurs must in general be large in comparison to those associated with Faraday rotation (see Section 8.2), it is possible to depolarize

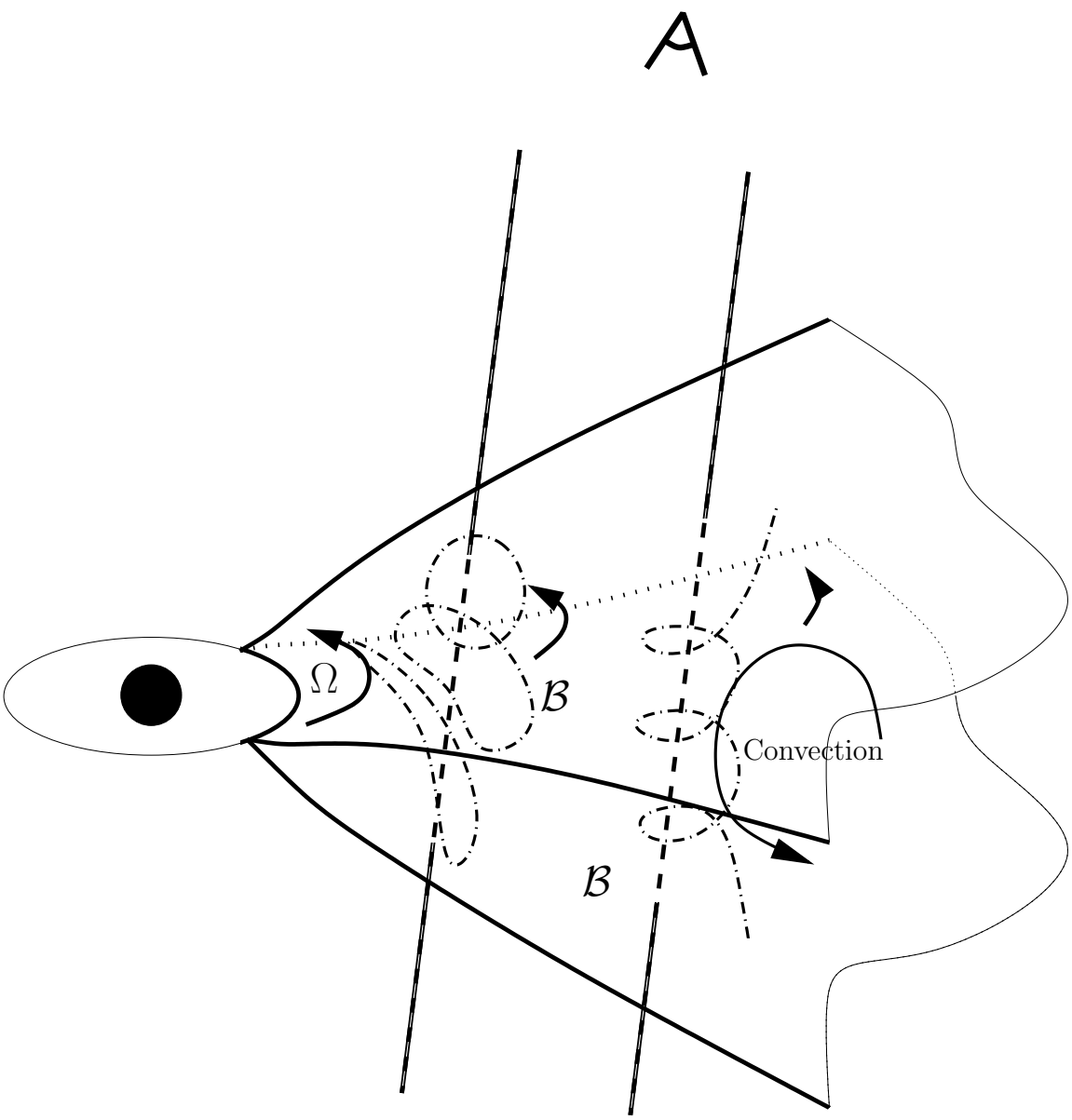

Figure 8.1: A shearing disk is shown in cross section. The angular velocity (Ω), magnetic field lines, and convection are shown for two possible sources of magnetic helicity. On the left, magnetic field lines are sheared by differential rotation in the disk by increasing degrees with increasing disk depth due to the vertical density gradient. On the right, convection within the disk coupled with differential rotation generates a helical field geometry.

the latter without significantly affecting the former.

The regions in which these processes may occur is limited to the those which obey

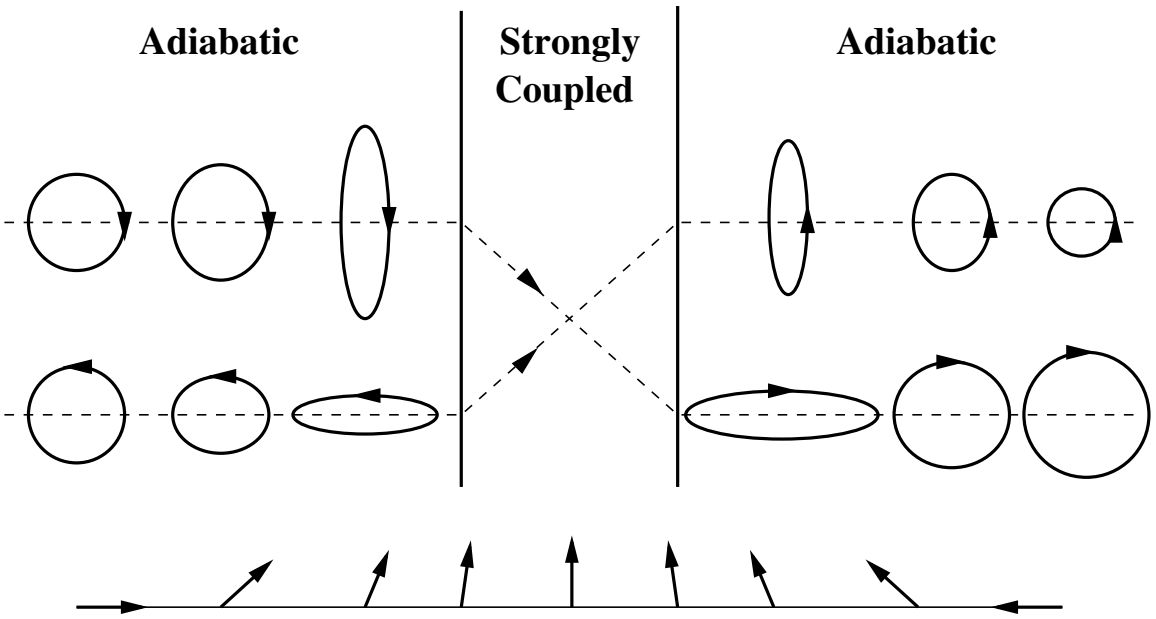

Figure 8.2: The two polarization eigenmodes are shown for a field reversal along the line of sight. The direction of the magnetic field relative to the line of sight is shown at the bottom. In addition to rotating against the line of sight, the field is also taken to be rotating about it in the sense of the top mode. Also demarked are the adiabatic and strongly coupled regimes (see Section 8.2 for more details).

the adiabatic criterion (equations (8.1)). Since this condition depends explicitly upon the angle between the magnetic field and the line of sight (θ), in tangled fields this criterion may be expected to be violated when this angle is near $\pi/2$. Because the geometric effects lead to a coupling between the plasma modes, their contributions will be dominated by regions near the strongly coupled limit ($\theta \sim \pi/2$). Therefore, the value of θ at which the condition fails can significantly modify the magnitude and spectral properties of the resulting polarization. This is indeed found to be the case, with the spectral properties changing character depending upon whether the dominant effect leading to a violation of the adiabatic criterion is rotation of the field about the line of sight, or the reversal of the field along the line of sight. Furthermore, at high enough frequencies there will be no region in which the adiabatic condition holds, and thus an upper frequency cutoff will exist in the circular polarisation spectrum.

8.2 Source of Geometric Phase Effects in Magnetized Plasmas

Geometric phase effects encompass a large class of physical phenomena which depend not only upon the current position in phase space of a given physical system, but also the path traversed by the system (usually taken to be closed). Examples range from the parallel-propagation of vectors on curved manifolds (in which the difference between the initial and final orientation of the vector depends upon the path taken) to the precession of electron magnetic moments in oscillating magnetic fields (as originally discussed by Berry 1984). In each of these instances a recurrent feature is the dependence of the eigenvectors of the physical system upon the position in the phase space. In the context of magnetized plasmas, geometric phase effects will occur when the polarizations of the plasma modes change.

As discussed in Appendix D, the polarization eigenmodes of a magnetized plasma can be specified by two angles, the polarization angle ϕ and the ellipticity angle χ. These are defined by the orientation of the polarization ellipse and the arctangent of its semi-major axis divided by its semi-minor axis, respectively. As discussed in detail in Ginzburg (1970), the two polarization eigenmodes must become strongly coupled in the limit of vanishing density. This is clearly the case in vacuum where the net polarization must be parallel propagated along the path of the ray regardless of the characteristics of a trace magnetic field and plasma density which are enough to formally specify the polarizations of the eigenmodes but have negligible impact upon the propagation of the polarization. Consequently there are two distinct limiting radiative transfer regimes, the *adiabatic* regime in which the modes propagate nearly independently, and the *strongly coupled* regime in which the net polarization propagates essentially as in vacuum (see, e.g., Appendix C). The two regimes are

delineated by

$$\begin{aligned}
&\sqrt{\left|\frac{d\chi}{dz}\right|^2+\left|\frac{d\phi}{dz}\right|^2} \ll \left|\frac{\Delta k}{2}\right| && \text{adiabatic} \\
&\sqrt{\left|\frac{d\chi}{dz}\right|^2+\left|\frac{d\phi}{dz}\right|^2} \gg \left|\frac{\Delta k}{2}\right| && \text{strongly coupled}\,,
\end{aligned} \tag{8.1}$$

where, in the high-frequency limit,

$$\Delta k \simeq \frac{\omega}{c} XY\cos\theta \equiv \delta k \mu\,, \tag{8.2}$$

in which X and Y are the square of the ratio of the plasma frequency to ω and the ratio of the cyclotron frequency to ω, respectively, θ is the angle between the line of sight and the magnetic field, $\delta k \equiv \omega XY/c$, and $\mu \equiv \cos\theta$. In the adiabatic limit (i.e., the limit of constant χ and ϕ) the modes can be treated as independent. The lowest-order corrections to this are derived in Appendix D for the general case of an anisotropic medium, and then in particular for the case of a magnetized plasma in Appendix E. Keeping lowest-order terms, the resulting radiative transfer equation can be written

$$\frac{d}{dz}\begin{pmatrix} I \\ Q \\ U \\ V \end{pmatrix} = \begin{pmatrix} 0 & 0 & 0 & 0 \\ 0 & 0 & b_3 & 0 \\ 0 & -b_3 & 0 & b_1 \\ 0 & 0 & -b_1 & 0 \end{pmatrix} \begin{pmatrix} I \\ Q \\ U \\ V \end{pmatrix}\,, \tag{8.3}$$

where

$$\begin{aligned}
b_1 &= -\frac{1}{2}\Delta k \cos 2\chi \\
b_3 &= \frac{1}{2}\Delta k \sin 2\chi + \frac{d\phi}{dz}\,.
\end{aligned} \tag{8.4}$$

Since I is decoupled from the other Stokes parameters at this level, in what follows we will restrict ourselves to Q, U, and V. Despite that the variation in ellipticity does

not explicity appear in equation (8.3), it does enter in two ways. Firstly, it appears in the evolution of χ in b_1 and b_3. Secondly, it appears in the determination of the minimum μ at which the propagation may be treated in the adiabatic regime.

8.2.1 Perturbative Treatment of the Transfer Equation

The dependence of b_1 and b_3 upon χ may be treated perturbatively. This can be done by defining ψ by

$$\tan 2\psi \equiv b_1/b_3 \quad \text{and} \quad d\tau \equiv \sqrt{b_1^2 + b_3^2}dz\,. \tag{8.5}$$

Note that to lowest order in $d\chi/dz$ and $d\phi/dz$,

$$\begin{aligned} \frac{d\psi}{d\tau} &\simeq \frac{d\chi}{d\tau} \\ \cos 2\psi &\simeq \cos 2\chi - \sin 2\chi \cos 2\chi \frac{d\phi}{d\tau} \\ \sin 2\psi &\simeq \sin 2\chi + \cos^2 2\chi \frac{d\phi}{d\tau}\,. \end{aligned} \tag{8.6}$$

Equation (8.3) can be simplified by expanding in the eigenvectors of the transfer matrix,

$$\begin{aligned} \hat{\mathbf{e}}_0 &= \begin{pmatrix} \cos 2\psi \\ 0 \\ \sin 2\psi \end{pmatrix} & \frac{d\hat{\mathbf{e}}_0}{d\tau} &= \sqrt{2}\frac{d\psi}{d\tau}\left(\hat{\mathbf{e}}_+ + \hat{\mathbf{e}}_-\right) \\ \hat{\mathbf{e}}_\pm &= \frac{1}{\sqrt{2}}\begin{pmatrix} \sin 2\psi \\ \pm i \\ -\cos 2\psi \end{pmatrix} & \frac{d\hat{\mathbf{e}}_\pm}{d\tau} &= \sqrt{2}\frac{d\psi}{d\tau}\hat{\mathbf{e}}_0\,. \end{aligned} \tag{8.7}$$

Then,

$$\frac{d}{d\tau}\begin{pmatrix} S^+ \\ S^0 \\ S^- \end{pmatrix} = \left[\begin{pmatrix} i & 0 & 0 \\ 0 & 0 & 0 \\ 0 & 0 & -i \end{pmatrix} + \sqrt{2}\frac{d\psi}{d\tau}\begin{pmatrix} 0 & 1 & 0 \\ 1 & 0 & 1 \\ 0 & 1 & 0 \end{pmatrix}\right]\begin{pmatrix} S^+ \\ S^0 \\ S^- \end{pmatrix}\,. \tag{8.8}$$

where the additional term comes from the dependence of the eigenvectors upon position. The Stoke's parameters may be expanded perturbatively in terms of an order parameter ϵ which is comparable to $d\psi/d\tau$ (but to be set to unity in the end),

$$\begin{pmatrix} S^+ \\ S^0 \\ S^- \end{pmatrix} = \begin{pmatrix} S_0^+ \\ S_0^0 \\ S_0^- \end{pmatrix} + \epsilon \begin{pmatrix} S_1^+ \\ S_1^0 \\ S_1^- \end{pmatrix} + \dots , \tag{8.9}$$

Then, inserting this into equation (8.8) and equating like orders gives

$$\begin{aligned} \frac{d}{d\tau}\begin{pmatrix} S_0^+ \\ S_0^0 \\ S_0^- \end{pmatrix} &= \begin{pmatrix} i & 0 & 0 \\ 0 & 0 & 0 \\ 0 & 0 & -i \end{pmatrix}\begin{pmatrix} S_0^+ \\ S_0^0 \\ S_0^- \end{pmatrix} \\ \frac{d}{d\tau}\begin{pmatrix} S_1^+ \\ S_1^0 \\ S_1^- \end{pmatrix} &= \begin{pmatrix} i & 0 & 0 \\ 0 & 0 & 0 \\ 0 & 0 & -i \end{pmatrix}\begin{pmatrix} S_1^+ \\ S_1^0 \\ S_1^- \end{pmatrix} + \sqrt{2}\frac{d\psi}{d\tau}\begin{pmatrix} 0 & 1 & 0 \\ 1 & 0 & 1 \\ 0 & 1 & 0 \end{pmatrix}\begin{pmatrix} S_0^+ \\ S_0^0 \\ S_0^- \end{pmatrix} \\ &\vdots \end{aligned} \tag{8.10}$$

This process may be iterated to what ever order is desired. However, here we shall be interested only to linear order.

8.2.2 Dependence of $\mu_{\min}$ upon Plasma Parameters

The adiabatic condition can be recast in terms of the reversal length scale

$$L_R \equiv \pi \left(\left|\frac{d\chi}{dz}\right|^2 + \left|\frac{d\phi}{dz}\right|^2 \right)^{-1/2} = L_R^0 \left\{ 1 + \left[\frac{Y}{4} \frac{\sqrt{1-\mu^2}(1+\mu^2)}{(Y/2)^2+\mu^2} \xi \right]^2 \right\}^{-1/2} , \tag{8.11}$$

where $L_R^0 \equiv \pi \left| d\phi/dz \right|^{-1}$, $\xi \equiv \left| d\theta/dz \right| / \left| d\phi/dz \right|$ (which is typically of order unity), and the Faraday rotation length scale

$$L_F = \frac{2\pi}{\Delta k} = L_F^0 \mu^{-1} , \tag{8.12}$$

where $L_F^0 \equiv 2\pi/\delta k$. Explicitly, the adiabatic (strongly coupled) regime corresponds to $L_R \gg L_F$ ($L_R \ll L_F$). Roughly, when $L_F \simeq L_R$, the polarization will "freeze" out. As $\mu \to 0$, $L_F \to \infty$, and hence the modes will become strongly coupled at some $\mu_{\min}$. Note, however, that when keeping terms to quadratic order in Y in Δk, near $\mu = 0$, $\Delta k \simeq \delta k Y$. Therefore, it is possible for the modes to remain in the adiabatic regime even when $\mu = 0$ as long as $L_R/L_F^0 \gg Y^{-1}$.

Because the quantities L_R and L_F depend upon μ explicitly, it is more transparent to restate the adiabatic condition in terms of L_R^0 and L_F^0 which depend upon the plasma parameters alone. Because of its nontrivial dependence upon μ, L_R is easiest to expand in three distinct limiting regimes:

$$L_R \simeq L_R^0 \begin{cases} 1 & \text{if} \quad \left(\dfrac{Y\xi}{4}\right)^{1/2} \ll \mu \\ \dfrac{4\mu^2}{Y\xi} & \text{if} \quad \dfrac{Y}{2} \ll \mu \ll \left(\dfrac{Y\xi}{4}\right)^{1/2} \\ \dfrac{Y}{\xi} & \text{if} \quad \mu \ll \dfrac{Y}{2} \end{cases} . \tag{8.13}$$

Thus the adiabatic condition in each of these regimes is

$$\frac{L_F^0}{L_R^0} \ll \begin{cases} \mu & \text{if} \quad \left(\dfrac{Y\xi}{4}\right)^{1/2} \ll \mu \\ \dfrac{4\mu^3}{Y\xi} & \text{if} \quad \dfrac{Y}{2} \ll \mu \ll \left(\dfrac{Y\xi}{4}\right)^{1/2} \\ \dfrac{Y^2}{\xi} & \text{if} \quad \mu \ll \dfrac{Y}{2} \end{cases} . \tag{8.14}$$

For $\mu = 0$, $L_F/L_R = Y^{-1}L_F^0/L_R^0$, thus in order to remain adiabatic through an entire field reversal, $L_F^0/L_R^0 \ll Y^2$, which typically does not occur in practice. Hence, the minimum μ for which the modes remain adiabatic is then given by

$$\mu_{\min} = \begin{cases} \dfrac{L_F^0}{L_R^0} & \text{if} \quad \left(\dfrac{Y\xi}{4}\right)^{1/2} \ll \dfrac{L_F^0}{L_R^0} \\ \left(\dfrac{Y\xi}{4}\dfrac{L_F^0}{L_R^0}\right)^{1/3} & \text{if} \quad \dfrac{Y^2}{2\xi} \ll \dfrac{L_F^0}{L_R^0} \ll \left(\dfrac{Y\xi}{4}\right)^{1/2} \end{cases} . \tag{8.15}$$

In all cases, $\mu_{\min} > Y$, thus the $Y/2$ terms in the denominators of equations (E.4) may be neglected.

The fact that the modes become strongly coupled for $\mu < \mu_{\min}$ has two direct consequences. Firstly, the modes will nearly always become strongly coupled when propagating sufficiently orthogonal to the magnetic field, forcing the fast mode to map onto the slow mode and vice-versa.[1]

Secondly, because the geometric phase terms presented here are precisely the lowest-order coupling terms, the results in Appendix D are only applicable in the adiabatic regime. Therefore, it will be generally true that $\Delta k > d\phi/dz$. However, when the Faraday depth is large, the resulting polarimetric properties can be dominated by the geometric phase terms due to Faraday depolarization.

8.3 Transfer of an Incident Polarization

The transfer of an incident polarization provides a simple example that produces many of the main effects due to the additional terms.

8.3.1 With $d\chi/dz = 0$

While in general the ellipticity of the polarization eigenmodes will change, first consider a scenario in which it does not. This provides insight into the source of the effect while avoiding the complications of the detailed perturbative approach. In this case the magnetic field geometry is helical (shown in Figure 8.3) where the pitch angle is determined by the strength of the field and the ratio of $d\phi/dz$ to Δk. The radiative transfer equation is simply the zeroth-order equation in equation (8.10), and has the

[1] As a result, the Faraday rotation is proportional to $\mathbf{B} \cdot d\mathbf{x}$, as commonly quoted, and not $|\mathbf{B} \cdot d\mathbf{x}|$ as would occur otherwise. This can be explicity effected by replacing μ with $|\mu|$ in the definition of Δk.

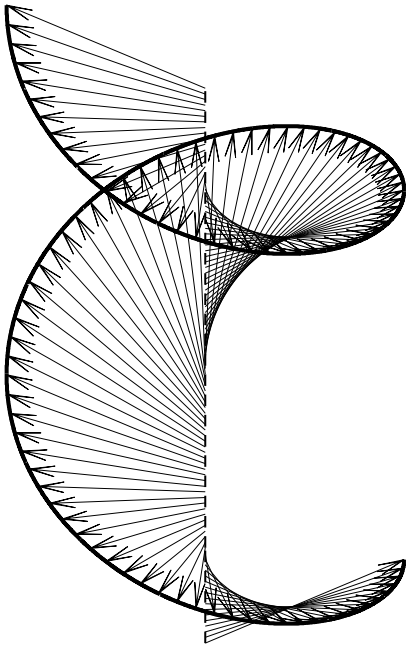

Figure 8.3: Shown is the helical field (vectors) discussed in Section 8.3.1 along the line of sight (dashed line) inclined at 60° to better demonstrated the geometry. Also shown is the loci of the tips of the magnetic field vectors (sold line).

general solutions

$$\begin{aligned} S_0^+ &= C_0^+ e^{i\tau} \\ S_0^0 &= C_0^0 \\ S_0^- &= C_0^- e^{-i\tau} \,. \end{aligned} \tag{8.16}$$

In terms of the initial conditions

$$\begin{aligned} C_0^0 &= cQ_i + sV_i \\ C_0^\pm &= \frac{1}{\sqrt{2}} \left(sQ_i \mp iU_i - cV_i \right) \,, \end{aligned} \tag{8.17}$$

where $c \equiv \cos 2\psi$ and $s \equiv \sin 2\psi$. The resulting final polarization is then

$$\begin{aligned} Q_f &= cS_0^0 + \frac{s}{\sqrt{2}}\left(S_0^+ + S_0^-\right) \\ &= \left(c^2 + s^2\cos\tau\right)Q_i + sU_i\sin\tau + (1-\cos\tau)\,scV_i \\ U_f &= \frac{i}{\sqrt{2}}\left(S_0^+ - S_0^-\right) \\ &= -sQ_i\sin\tau + U_i\cos\tau + cV_i\sin\tau \\ V_f &= sS^0 - \frac{c}{\sqrt{2}}\left(S_0^+ + S_0^-\right) \\ &= (1-\cos\tau)\,scQ_i - cU_i\sin\tau + \left(s^2 + c^2\cos\tau\right)V_i\,. \end{aligned} \tag{8.18}$$

These may be averaged over variations in τ associated with differing path lengths (denoted by angle brackets), resulting in

$$\begin{aligned} \langle Q_f\rangle &= c^2Q_i + scV_i \\ \langle U_f\rangle &= 0 \\ \langle V_f\rangle &= s^2V_i + scQ_i\,. \end{aligned} \tag{8.19}$$

In order to select out geometric phase effects associated with a nonzero $d\phi/dz$ consider the average (denoted by an over-bar) of this with the case in which the magnetic field is reversed (define quantities associated with the former with a pre-superscript of $+$ and the latter with a pre-superscript of $-$). For the reversed field

$$\sin 2\,{}^+\chi = -\sin 2\,{}^-\chi \quad \text{and} \quad \cos 2\,{}^+\chi = \cos 2\,{}^-\chi\,, \tag{8.20}$$

and hence,

$$\begin{aligned} \frac{1}{2}\left({}^-s^2 + {}^+s^2\right) &\simeq \sin^2\chi \\ \frac{1}{2}\left({}^-c^2 + {}^+c^2\right) &\simeq \cos^2\chi \\ \frac{1}{2}\left({}^-s\,{}^-c + {}^+s\,{}^+c\right) &\simeq \left(\cos^2\chi - \sin^2\chi\right)\cos\chi\frac{d\phi}{d\tau}\,, \end{aligned} \tag{8.21}$$

where the lack of pre-superscripts on the χ in these expressions reflects the fact that they may be evaluated for either case. Using the values in Appendix E for $\cos 2\chi$ and $\sin 2\chi$, and the fact that $\mu_{\min} \gg Y$,

$$\begin{aligned}
\frac{1}{2}\left({}^{-}s^2 + {}^{+}s^2\right) &\simeq 1 \\
\frac{1}{2}\left({}^{-}c^2 + {}^{+}c^2\right) &\simeq \frac{Y^2}{4\mu_i \mu} \ll 1 \\
\frac{1}{2}\left({}^{-}s{}^{-}c + {}^{+}s{}^{+}c\right) &\simeq -\frac{Y}{2\mu^2}\frac{L_F^0}{L_R^0}\,,
\end{aligned} \tag{8.22}$$

where

$$\frac{d\phi}{d\tau} = \frac{d\phi/dz}{\Delta k/2} \simeq |\mu|^{-1}\frac{L_F^0}{L_R^0}\,, \tag{8.23}$$

was used. Therefore

$$\begin{aligned}
\overline{\langle Q_f \rangle} &\simeq \frac{Y^2}{4\mu^2} Q_i - \frac{Y}{2\mu_i^2}\frac{L_F^0}{L_R^0} V_i \\
\overline{\langle U_f \rangle} &= 0 \\
\overline{\langle V_f \rangle} &\simeq V_i - \frac{Y}{2\mu^2}\frac{L_F^0}{L_R^0} Q_i\,.
\end{aligned} \tag{8.24}$$

Some distinct features are immediately clear from equation (8.24). Firstly, the average linear polarization is strongly Faraday depolarized. Secondly, the average circular polarization is relatively unaffected, except for contributions from the initial Q. These depend strongly upon the value of μ, being dominated by $\mu_{\min}$. Given a flat distribution of θ on the sphere, and assuming that $V_i = 0$ yields

$$\overline{\langle V_f \rangle}_\Omega \simeq -\frac{Y}{2\mu_{\min}}\frac{L_F^0}{L_R^0} Q_i\,. \tag{8.25}$$

As a result, the spectral dependence of $\mu_{\min}$ enters directly into that of the circular polarization. In particular, inserting equation (8.15) into the expression for $\overline{\langle V_f \rangle}_\Omega$,

gives

$$\overline{\langle V_f \rangle}_\Omega \simeq -\frac{Q_i}{2} \begin{cases} Y & \text{if} \quad \left(\frac{Y\xi}{4}\right)^{1/2} \ll \frac{L_F^0}{L_R^0} \\ \frac{4}{\xi}\left(\frac{Y\xi}{4}\frac{L_F^0}{L_R^0}\right)^{2/3} & \text{if} \quad \frac{Y^2}{2\xi} \ll \frac{L_F^0}{L_R^0} \ll \left(\frac{Y\xi}{4}\right)^{1/2} \end{cases} . \tag{8.26}$$

Of particular interest is the fact that for $Y^2 \ll L_F^0/L_R^0 \ll (Y\xi)^{1/2}$ the circular polarization *increases* with frequency as $\nu^{2/3}$ ($L_F^0 \propto \nu^2$ and $Y \propto \nu^{-1}$). However, this occurs when the $d\chi/dz$ term dominates the inequality in equation (8.1), and hence when it is nonzero, violating the assumption that χ was constant. For most values of θ this is not a serious oversight as for a constant $d\theta/dz$, $d\chi/dz$ is only significant when μ is small. But as seen in equation (8.25), this precisely the region which dominates the effect. Hence, the perturbative approach may shed some light upon the mitigating effects that a nonzero $d\chi/dz$ may have upon this polarization mechanism.

8.3.2 With $d\chi/dz \neq 0$

In the previous section the zeroth-order terms in equation (8.10) were obtained. These may then be substituted directly into the first-order equations to solve for the first-order corrections to the constant χ case. Strictly speaking it is also necessary to distinguish between $s_i = \sin\psi_i$, $c_i = \cos\psi_i$ and $s_f = \sin\psi_f$, $c_f = \cos\psi_f$ where ψ_i and ψ_f are the initial and final values of ψ. The first-order solutions are then

$$\begin{aligned} S_1^+ &= e^{i\tau} \int d\tau e^{-i\tau} \sqrt{2} \frac{d\psi}{d\tau} S_0^0 \\ &\simeq e^{i\tau} \int d\tau C_0^0 e^{-i\tau} \sqrt{2} \frac{d\chi}{d\tau} \\ S_1^0 &= \int d\tau \sqrt{2} \frac{d\psi}{d\tau} \left(S_0^+ + S_0^-\right) \\ &\simeq e^{i\tau} \int d\tau \left(C_0^+ e^{i\tau} + C_0^- e^{-i\tau}\right) \sqrt{2} \frac{d\chi}{d\tau} \\ S_1^- &= e^{-i\tau} \int d\tau e^{i\tau} \sqrt{2} \frac{d\psi}{d\tau} S_0^0 \\ &\simeq e^{-i\tau} \int d\tau C_0^0 e^{i\tau} \sqrt{2} \frac{d\chi}{d\tau} . \end{aligned} \tag{8.27}$$

Because $\mu_{\rm min}$ is generally greater than Y for physically reasonable scenarios,

$$\frac{d\chi}{dz} \simeq -\frac{Y}{4\mu^2}\frac{d\theta}{dz} \tag{8.28}$$

and hence the integrals for $S_1^{\pm}$ and S_1^0 will be dominated by contributions from around $\mu_{\rm min}$, yielding a value dependent upon τ_0, the optical depth at which $\mu = \mu_{\rm min}$. As a direct result, after averaging over variations in path length, and hence over τ and τ_0, the contributions at the first-order level will vanish. This is only permissable if there are a large number of Faraday rotations along the line of sight, i.e., if the source is Faraday thick.

As a result, even when nonzero $d\chi/dz$ effects are accounted for, the result is essentially that of the previous section:

$$\begin{aligned}
Q_f &= c_f S_0^0 + \frac{s_f}{\sqrt{2}}\left(S_0^+ + S_0^-\right) \\
&= \left(c_f c_i + s_f s_i \cos\tau\right) Q_i + s_f U_i \sin\tau + \left(c_f s_i - s_f c_i \cos\tau\right) V_i \\
U_f &= \frac{i}{\sqrt{2}}\left(S_0^+ - S_0^-\right) \\
&= -s_i Q_i \sin\tau + U_i \cos\tau + c_i V_i \sin\tau \\
V_f &= s_f S^0 - \frac{c_f}{\sqrt{2}}\left(S_0^+ + S_0^-\right) \\
&= \left(s_f c_i - c_f s_i \cos\tau\right) Q_i - c_f U_i \sin\tau + \left(s_f s_i + c_f c_i \cos\tau\right) V_i \,.
\end{aligned} \tag{8.29}$$

Again, these are averaged over variations in τ, resulting in

$$\begin{aligned}
\langle Q_f \rangle &= c_f c_i Q_i + c_f s_i V_i \\
\langle U_f \rangle &= 0 \\
\langle V_f \rangle &= s_f s_i V_i + s_f c_i Q_i \,.
\end{aligned} \tag{8.30}$$

Again, the geometric effects can be selected out by averaging with the case where the

magnetic field is reversed. Therefore

$$\begin{aligned}
\overline{\langle Q_f \rangle} &\simeq \frac{Y^2}{4\mu_i\mu_f} Q_i - \frac{Y}{2\mu_i^2}\frac{L_F^0}{L_R^0} V_i \\
\overline{\langle U_f \rangle} &= 0 \\
\overline{\langle V_f \rangle} &\simeq V_i - \frac{Y}{2\mu_f^2}\frac{L_F^0}{L_R^0} Q_i \,,
\end{aligned} \tag{8.31}$$

with all of the attendant consequences, with the distinct advantage that this now does extend to the $d\chi/dz \neq 0$ case.

8.4 *In Situ* Synchrotron Emission

While the previous section provides some insight into how the general mechanism works, it is also possible for the plasma itself to emit. The natural mechanism is synchrotron emission, which will be strongly polarized in Q. For simplicity we have assumed that the emission and absorption are isotropic. In this case, in terms of the eigenbasis, the transfer equation is now given by

$$\frac{d}{d\tau}\begin{pmatrix} S_0^+ \\ S_0^0 \\ S_0^- \end{pmatrix} = \frac{\epsilon_Q \zeta}{\sqrt{2}}\begin{pmatrix} \sin 2\psi \\ \sqrt{2}\cos 2\psi \\ \sin 2\psi \end{pmatrix} + \begin{pmatrix} i-\eta & 0 & 0 \\ 0 & -\eta & 0 \\ 0 & 0 & -i-\eta \end{pmatrix}\begin{pmatrix} S_0^+ \\ S_0^0 \\ S_0^- \end{pmatrix} , \tag{8.32}$$

where $\eta = \alpha dz/d\tau$ is the appropriately normalized absorption coefficient, ζ is properly normalized emissivity $\zeta = j dz/d\tau$, and ϵ_Q is the degree of polarization of the intrinsic emission. Also, as $d\psi/dz$ is going to be small (but nonzero), approximate the ψ terms in the emission as being equal to the final value and constant. For the same reason as before the explicit first-order contributions from $d\chi/dz$ vanish. Again, the solutions

are straightforward.

$$\begin{aligned} S^+ &= \frac{s_f \epsilon_Q \zeta}{\sqrt{2}(i-\eta)} \left(e^{(i-\eta)\tau} - 1\right) \\ S^0 &= -\frac{c_f \epsilon_Q \zeta}{\eta} \left(e^{-\eta\tau} - 1\right) \\ S^- &= -\frac{s_f \epsilon_Q \zeta}{\sqrt{2}(i+\eta)} \left(e^{-(i+\eta)\tau} - 1\right) \,, \end{aligned} \tag{8.33}$$

and hence

$$\begin{aligned} Q_f =& \frac{c_f^2 \epsilon_Q \zeta}{\eta} \left(1 - e^{-\eta\tau}\right) \\ &+ \frac{s_f^2 \epsilon_Q \zeta}{1+\eta^2} \left(e^{-\eta\tau} \sin\tau - \eta e^{-\eta\tau} \cos\tau + \eta\right) \\ U_f =& \frac{s_f \epsilon_Q \zeta}{1+\eta^2} \left(e^{-\eta\tau} \cos\tau - 1 + \eta e^{-\eta\tau} \sin\tau\right) \\ V_f =& \frac{s_f c_f \epsilon_Q \zeta}{\eta} \left(1 - e^{-\eta\tau}\right) \\ &- \frac{s_f c_f \xi}{1+\eta^2} \left(e^{-\eta\tau} \sin\tau - \eta e^{-\eta\tau} \cos\tau + \eta\right) \end{aligned} \tag{8.34}$$

After averaging over variations in τ,

$$\begin{aligned} \langle Q_f \rangle &= \frac{c_f^2 \epsilon_Q \zeta}{\eta} \left(1 - e^{-\eta\tau}\right) + \frac{s_f^2 \xi \eta}{1+\eta^2} \\ \langle U_f \rangle &= -\frac{s_f \epsilon_Q \zeta}{1+\eta^2} \\ \langle V_f \rangle &= \frac{s_f c_f \epsilon_Q \zeta}{\eta} \left(1 - e^{-\eta\tau}\right) - \frac{s_f c_f \epsilon_Q \zeta \eta}{1+\eta^2} \,. \end{aligned} \tag{8.35}$$

Again, we average over reversed fields to get the geometric terms and express the result in terms of the plasma parameters

$$\begin{aligned}
\overline{\langle Q_f \rangle} &\simeq \left[\frac{Y^2}{4\mu_f^2} \frac{1}{\eta} \left(1 - e^{-\eta\tau}\right) + \frac{\eta}{1+\eta^2} \right] \epsilon_Q \zeta \\
\overline{\langle U_f \rangle} &\simeq -\frac{Y^2}{4|\mu_f|^3} \frac{L_F^0}{L_R^0} \frac{\epsilon_Q \zeta}{1+\eta^2} \\
\overline{\langle V_f \rangle} &\simeq -\frac{Y}{2\mu_f^2} \frac{L_F^0}{L_R^0} \epsilon_Q \zeta \left[\frac{1}{\eta} \left(1 - e^{-\eta\tau}\right) + \frac{\eta}{1+\eta^2} \right] .
\end{aligned} \tag{8.36}$$

The intensity in this case is given by

$$I_f = \frac{\zeta}{\eta} \left(1 - e^{-\eta\tau}\right) . \tag{8.37}$$

As a result the polarization fraction is given by

$$m_c = \frac{\overline{\langle V_f \rangle}}{I_f} \simeq -\frac{Y}{2\mu_f^2} \frac{L_F^0}{L_R^0} \epsilon_Q \left[1 + \frac{\eta^2}{1+\eta^2} \left(1 - e^{-\eta\tau}\right)^{-1} \right] . \tag{8.38}$$

The quantity η is roughly the amount of absorption in one Faraday length. As such, this quantity may be expected to be very small. Since τ must be large for the averaging over τ to apply, even for $\eta \simeq 1$, this produces a correction on the order of $1/2$, and hence may be neglected. Consequently, regardless of $\eta\tau$ (i.e. in both the optically thin and thick regimes)

$$m_c \simeq -\frac{Y}{2\mu_f^2} \frac{L_F^0}{L_R^0} \epsilon_Q \, , \tag{8.39}$$

which is precisely what would have been expected on the basis of equation (8.24). After averaging over magnetic field directions, this yields

$$\begin{aligned} m_c &\simeq -\frac{Y}{2\mu_{\min}}\frac{L_F^0}{L_R^0}\epsilon_Q \\ &\simeq -\frac{\epsilon_Q}{2}\begin{cases} Y & \text{if} \quad \left(\frac{Y\xi}{4}\right)^{1/2} \ll \frac{L_F^0}{L_R^0} \\ \frac{4}{\xi}\left(\frac{Y\xi}{4}\frac{L_F^0}{L_R^0}\right)^{2/3} & \text{if} \quad \frac{Y^2}{2\xi} \ll \frac{L_F^0}{L_R^0} \ll \left(\frac{Y\xi}{4}\right)^{1/2} \end{cases}, \end{aligned} \tag{8.40}$$

with all of the properties discussed after equation (8.26).

8.5 Frequency Dependence

In order to compare this circular polarization to observations it is useful to express equation (8.40) in terms of frequency. At a high enough frequency the adiabatic condition will fail at all points along the ray. This first occurs when $L_R^0 = L_F^0$ and hence at

$$\nu_u \equiv \nu_P \left(\nu_B \frac{L_R^0}{c}\right)^{1/2} = \nu_P \left(\frac{L_R^0}{\lambda_B}\right)^{1/2}, \tag{8.41}$$

where ν_P and ν_B are the plasma and cyclotron frequencies and λ_B is the cyclotron radius. In terms of ν_u, the transition frequency is given by

$$\nu_t \equiv \nu_B \left(\frac{\xi}{4}\right)^{1/5} \left(\frac{\nu_u}{\nu_B}\right)^{4/5}. \tag{8.42}$$

While the lower limit in the second inequality in equation (8.40) occurs when the modes remain adiabatic even through field reversals, usually a more stringent limit is reached when only one Faraday rotation occurs in the last optical depth, and hence the line of sight averages are no longer justified. Specifically, for a power-law electron distribution with index 2,

$$\tau \simeq Y\frac{z}{L_F^0}, \tag{8.43}$$

and hence this occurs when

$$\nu_l \simeq \nu_B \,. \tag{8.44}$$

Note that at this point, the source depth is given by

$$z \simeq L_F^0 \simeq \frac{\nu_B c}{\nu_P^2} \simeq \left(\frac{\nu_B}{\nu_u}\right)^2 L_R^0 \ll L_R^0 \tag{8.45}$$

In terms of these limits, the circular polarization fraction is given by,

$$m_c \simeq -\frac{\epsilon_Q}{2}\frac{\nu_B}{\nu_t}\begin{cases} 0 & \text{if} \quad \nu_u \ll \nu \\ (\nu/\nu_t)^{-1} & \text{if} \quad \nu_t \ll \nu < \nu_u \\ (\nu/\nu_t)^{2/3} & \text{if} \quad \nu_l \ll \nu \ll \nu_t \end{cases} . \tag{8.46}$$

While this mechanism does not in general require a tangled magnetic field to operate, the examples discussed in the next section such a field is present. This field is assumed to be created in an accretion disk via the MRI. The condition for the MRI to occur can be roughly given by $P_G/P_B \lesssim 1$. In terms of the plasma and cyclotron frequencies

$$\begin{aligned} \frac{P_G}{P_B} &= 2\left(\frac{\nu_P}{\nu_B}\right)^2 \frac{kT_i}{m_e c^2} \\ &= 4\xi^{-1/2}\frac{\lambda_B}{L_R^0}\left(\frac{\nu_t}{\nu_B}\right)^{5/2}\frac{kT_i}{m_e c^2}\,, \end{aligned} \tag{8.47}$$

where T_i is the ion temperature. That this ratio must be greater than unity places the following constraint upon the ion temperature:

$$kT_i > m_e c^2 \xi^{1/2}\frac{L_R^0}{4\lambda_B}\left(\frac{\nu_t}{\nu_B}\right)^{-5/2} . \tag{8.48}$$

Chapter 9

Applications

As an example application consider the polarimetric properties of a shearing magnetized disk. Despite the existence of a weak, and possibly structured seed field, the MRI will quickly create a highly tangled environment. Nonetheless, the preferential shearing (with disk radius and disk height) of the magnetic field associated with the disk will lead to a nonvanishing $\langle d\phi/dz \rangle$ and $\langle d\chi/dz \rangle$, the sign and magnitude of which will be determined by the gradient of the disk angular velocity. As a result, the sign of the polarization may be stable over long timescales.

9.1 Radio Emission in Sgr A*

The polarized emission from the Galactic center seen at 1.4, 4.8, 8.4, and 15 GHz (Bower et al., 2002) may be explained by considering the above scenario. This polarization has been found to have an increasing circular polarization fraction and variability with increasing frequency. Despite this, it has been found to have negligible circular polarization at 112 GHz (Bower et al., 2001).

These observations place immediate limits upon ν_t and ν_B. The transition frequency can not be any smaller than 15 GHz, while the cyclotron frequency can not be any larger than 1 GHz. Here, we assume that $\nu_t = 20$ GHz and $\nu_B = 0.5$ GHz. These provide a maximum (average) circular polarization fraction on the order of 1%

ν_B	0.5 GHz
ν_t	20 GHz
T_i	10^{12} K
ν_u	70 GHz
ν_P	2.7×10^{-2} GHz
L_R^0	4.1×10^8 cm
M	5×10^{11} cm
$m_{c\,\max}$	0.8%
B	180 G
n_e	9×10^6 cm^{-3}
A	$3 \times 10^4\, M^2$

Table 9.1: Listed are a number of quantities of interest in the Galactic center. The first three quantities, the cyclotron frequency ν_B, the transition frequency ν_t, and the ion temperature T_i were chosen a priori. Those in the second group, the upper cutoff frequency ν_u, the plasma frequency ν_P, and the typical reversal length scale L_R^0, are derived directly from the first group. The mass of the central black hole M is given for comparison. The third group are properties of the emitting region, including the strength of the random field B, electron number density n_e, and the approximate area of the emission region at GHz frequencies A in units of M^2.

as observed. The associated condition placed upon the temperature by the MRI is

$$T_i \gtrsim 1.5 \times 10^5 \xi^{1/2} \frac{L_R^0}{\lambda_B}\,\mathrm{K}\,. \tag{9.1}$$

Since the ion temperature can easily reach $10^{12}\,$K, this puts $L_R^0 \simeq 4.1 \times 10^8\,$cm. Since this should be identified with the shortest reversal length scale (i.e., the highest $d\phi/dz$) this is consistent with the other length scale in the problem, namely the mass of the black hole ($5 \times 10^{11}\,$cm). The associated plasma and upper cutoff frequencies are then approximately $2.7 \times 10^{-2}\,$GHz and 70 GHz, respectively. The pertinent frequencies and plasma characteristics are listed in Table 9.1.

Since $\nu_u \simeq 70$ GHz, no circular polarization would be expected at 112 GHz. Furthermore, at this frequency the polarization properties intrinsic to the emission should dominate, which in the case of synchrotron emission can be highly linearly polarized and is in fact what is observed. Also note that the magnetic field strength is that of the stochastic field, *not* the net field, which in this case has been assumed

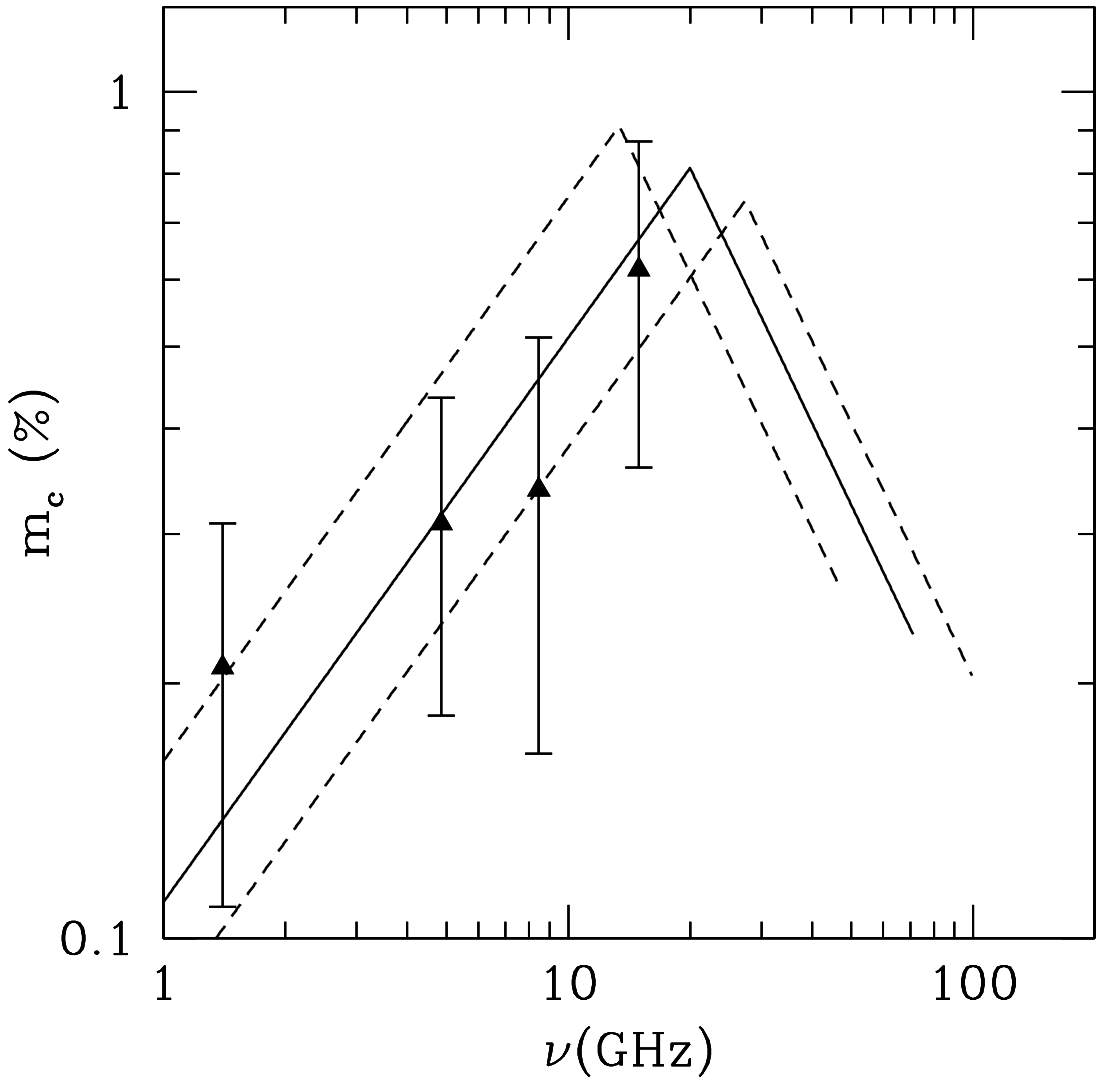

Figure 9.1: The circular polarization spectrum predicted by equation (8.46) (solid line) is compared to the average observed values from Sgr A* (filled triangles) (taken from Bower et al., 2002). The degree of variability is denoted by the errorbars (not to be confused with intrinsic uncertainty of the measurement). The parameters used are described in the text. Also shown by the dashed lines are the spectra when the magnetic field strength and plasma density are varied by $\pm 25\%$ to provide some measure of the strong connection between the variability of the environment and the polarization.

to vanish (though this is not necessary). Shown in Figure 9.1 is the resulting circular polarization spectrum compared to data points from Bower et al., 2002.

ν_B	3.0×10^2 GHz
ν_t	9.2×10^2 GHz
T_i	10^{12} K
ν_u	1.7×10^3 GHz
ν_P	16 GHz
L_R^0	1.2×10^3 cm
M	1.5×10^6 cm
$m_{c\,\max}$	11%
B	10^5 G
n_e	3×10^{12} cm^{-3}
A	—

Table 9.2: Same as Table 9.1 for a $10M_\odot$ black hole.

9.2 X-ray Binaries

X-ray binaries present a stellar mass analogue to the situation described in the previous section for the Galactic center. As described in Section 1.2, due to the differences in the scales between the two systems, the frequencies at which the polarization properties manifest themselves will differ. Based upon the scaling arguments discussed in that section,

$$\nu_P \propto \nu_B \propto M^{-1/2}\,. \tag{9.2}$$

Further, let the length scale over which field reversals occur scale as M. Then, from their definitions, the cyclotron, transition, and upper cutoff frequencies scale as

$$\nu_B \propto M^{-1/2} \tag{9.3}$$

$$\nu_t \propto M^{-3/10} \tag{9.4}$$

$$\nu_u \propto M^{-1/4}\,. \tag{9.5}$$

Note that since the maximum polarization fraction is proportional to ν_B/ν_t, it will scale as $M^{-1/5}$, and thus can be significantly higher for stellar mass systems. Table 9.2 lists the resulting quantities of interest for a black hole with a mass of $10M_\odot$ that is analogous to Sgr A*. The values shown in the table result in a strong circular polarization in the far infrared. However, this can be shifted to the near infrared

by assuming a higher radiative efficiency, which for stellar mass systems is almost certainly true. In any case, the high degree of circular polarization should be easily observable.

Part IV

Conclusions

A fully covariant generalization of magnetoionic theory has been developed. This has been done for cold and warm plasma, although due to its considerable complication the latter was not taken beyond the stage of determining the covariant extension of the conductivity tensor. The ability to perform radiative transfer in a covariant fashion has also been developed. This includes accounting for the anisotropic nature of magnetized plasmas, refraction, relativistic effects such as gravitational red-shifts and Doppler shifts, and the transport of the polarization vector along the ray.

The inclusion of relativistic effects has a number of unique consequences. They qualitatively change the topology of the dispersion relations, adding a new branch. In strongly sheared bulk flows (e.g., jets), they can substantially augment transfer and emission effects leading to the production of a net polarization. In the context of an accreting black hole, when the observation frequency is on the order of the plasma and cyclotron frequencies near the horizon, refraction can produce significant degrees of polarization, regardless of the intrinsic polarization of the emission mechanism. This occurs when one of the plasma eigenmodes is preferentially captured by the black hole, leading to a net excess of the other. The character of the resulting polarization will depend upon the nature of the plasma. In an ion plasma, the created polarization will typically be circular as a result of the plasma eigenmodes being nearly circular at the limiting polarization surface. In a pair plasma, the resulting polarization will in general be linear.

The refractive mechanism was demonstrated in detail by considering a geometrically thick, strongly magnetized accretion disk. Polarization fractions on the order of 10% were attained for emission originating near the horizon. This will be subsequently diluted by emission further out in the accretion flow, and hence the final polarization fraction depends upon the processes there. Nonetheless, it was possible to apply this mechanism to the Galactic center with marginal success. It was necessary to assume an extremely low radial velocity, however this is consistent with the requirement in the disk model that the magnetic field be strong enough to suppress the MRI. Unless the mass of M81 is larger by an order of magnitude than current estimates, this mechanism does not appear feasible in that system. Brightness temperature limits

rule out this mechanism completely in blazars. As a result, it requires the existence of another mechanism for producing the circular polarization in blazars, as well as an explanation for why it is not operating in the Galactic center.

XRBs in the quiescent or low/hard states may provide stellar mass analogues to the Galactic center. As a result, the refractive effects discussed in the context of Sgr A* may also be present in these as well. Due to the difference in mass scales, circular polarization resulting from the refractive mechanism would be expected to lie in the infrared, although for radiatively inefficient XRBs, this may reach as high as the ultraviolet. However, due to their much smaller size, effects occurring near the horizon will be extremely difficult to see. Nonetheless, current technologies exist, which if fitted with polarization capabilities, could in principle begin to study interesting portions of the M–$\dot{M}$ parameter space. This is a clear motivation for the development of such capabilities.

Lastly, because refractive plasma effects will be confined to approximately the decade in frequency surrounding the plasma frequency, they should be easily distinguishable from effects due to accretion models. As a result, they provide a unique tool with which to probe the plasma density and/or magnetic field strength near the horizon.

The second aspect of this work considered the transfer of radiation through strongly inhomogeneous environments. In this case, all effects are local and occur as a result of changes in the plasma parameters, and in particular the direction of the magnetic field. It was found that if the plasma is Faraday thick (i.e., there are a large number of Faraday rotations along the line of sight), it was possible for geometric effects to dominate. Given a net magnetic helicity, even in the absence of a net magnetic field, it is possible to generate a net circular polarization. This situation may result in the case of a differentially rotating accretion disk, in which the axial vector which determines the handedness of the circular polarization is the angular momentum of the disk as opposed to a structured magnetic field. The degree and spectral character of this circular polarization is sensitively dependent upon when/if the plasma eigenmodes become strongly coupled. This condition is dependent upon two distinct measures of

the change of polarization of the plasma eigenmodes, the rate of rotation of the polarization ellipse about the line of sight, and the rate of change of its shape. Depending upon which of these dominate the condition, the frequency of the dependence of the resulting circular polarization changes. For frequencies such that the change in shape dominates the condition the polarization fraction increases with frequency as $\nu^{2/3}$. In both cases, the high degree of Faraday rotation would be expected to depolarize any linear polarization. However, for sufficiently high or low frequencies there is no region in which the plasma eigenmodes are not strongly coupled, thus exhibiting the intrinsic polarization of the emission.

This mechanism was applied with success to the Galactic center, reproducing the general shape of the circularly polarized spectrum and its variability, for reasonable parameters. Because this mechanism is local, it can be applied to extragalactic sources with out suffering from the brightness temperature constraints inherent in the refractive mechanism. Therefore, it remains a viable explanation of the circular polarization in M81 and blazars. Because the circular polarization is constrained to be on the order of $0.3\nu_B/\nu_t$, it naturally predicts small polarizations at GHz frequencies, on the order of a few percent, as observed.

This has also been applied to XRBs. Again, this will produce a polarization signal in the infrared. However, because the cyclotron, transition, and upper cutoff frequencies scale differently, the predicted polarization in this case will be on the order of 10%. Therefore, this should be considered a strong motivation for the development of infrared polarimetry.

Detections of circular polarization arising from this mechanism provide a probe of the underlying degree of randomness of the magnetic field. In particular, since m_c depends upon the ratio of the number of field rotations to the number of Faraday rotations along the line of sight, measurements of the latter (e.g., by higher frequency observations) imply a value for the former. In this way, information regarding the MRI, field geometry, and accretion disk physics may be obtained.

Future investigations of refractive plasma effects in black hole accretion flows will require more realistic thick disk models. These may be obtained from the many

pseudo-Newtonian, and more recently, relativistic MHD disk simulations available in the computational literature (see, e.g., Gammie et al., 2003; Hawley et al., 2001). Two additional applications discussed in Part I, but not covered in detail thus far, are those to jets and neutron star atmospheres. Jets provide an obvious environment in which a highly magnetized plasma is present. Although the precise composition and structure of the jet plasma is not yet known, a number of plasma effects are already apparent, including Faraday rotation. In this environment, as suggested in Section 6.2, even at high frequencies dispersion may be able to produce polarization. Neutron star atmospheres have been shown to have considerable consequences for the emergent X-ray polarization, which therefore may be diagnostic of the conditions there (Lai & Ho, 2003a). Due to the highly anisotropic nature of the opacity in this environment, even a small change in direction can have substantial effects upon the resultant polarization. Since in both applications, refractive and dispersive plasma effects can have a significant impact, future work should consider these as well.

The discussion of polarized radiative transfer through tangled magnetic fields has focused on a constant strength field which, while random along the line of sight, rotates about it at a nearly constant rate. This is, of course, not the expected case in many environments of interest. Monte Carlo simulations can provide a method with which to investigate the geometric effects in realistic environments. Ultimately, it will be necessary to develop a treatment in which the resultant polarization is obtained in terms of the statistics of the magnetic field. In this fashion, circular polarization measurements will be able to provide quantitative information regarding the magnetic field geometry.

Bibliography

Aitken D. K., Greaves J., Chrysostomou A., Jenness T., Holland W., Hough J. H., Pierce-Price D., Richer J., 2000, ApJL, 534, L173

Arons J., Barnard J. J., 1986, ApJ, 302, 120

Baganoff F., , 2004, private communication

Baganoff F. K., Bautz M. W., Brandt W. N., Chartas G., Feigelson E. D., Garmire G. P., Maeda Y., Morris M., Ricker G. R., Townsley L. K., Walter F., 2001, Nature, 413, 45

Bao G., Hadrava P., Wiita P. J., Xiong Y., 1997, ApJ, 487, 142

Bao G., Wiita P. J., Hadrava P., 1998, ApJ, 504, 58

Barnard J. J., Arons J., 1986, ApJ, 302, 138

Barr P., Mushotzky R. F., 1986, Nature, 320, 421

Barr P., Pollard G., Sanford P. W., Ives J. C., Ward M., Hine R. G., Longair M. S., Penston M. V., Boksenberg A., Lloyd C., 1980, MNRAS, 193, 549

Beckert T., Falcke H., 2002, A&A, 388, 1106

Bekefi G., 1966, Radiation Processes in Plasma Physics. Wiley, New York

Berry M. V., 1984, Proc. Roy. Soc., A392, 45

Blandford R. D., 1985, Theoretical models of active galactic nuclei. Active galactic nuclei. Manchester University Press, Manchester, pp 281–299

Blandford R. D., Begelman M. C., 1999, MNRAS, 303, L1

Blandford R. D., Begelman M. C., 2004, MNRAS, 349, 68

Bower G. C., 2003, Ap&SS, 288, 69

Bower G. C., Falcke H., Backer D. C., 1999, ApJL, 523, L29

Bower G. C., Falcke H., Herrnstein R. M., Zhao J., Goss W. M., Backer D. C., 2004, astro-ph/0404001

Bower G. C., Falcke H., Mellon R. R., 2002, ApJL, 578, L103

Bower G. C., Falcke H., Sault R. J., Backer D. C., 2002, ApJ, 571, 843

Bower G. C., Wright M. C. H., Falcke H., Backer D. C., 2001, ApJL, 555, L103

Boyd T. J. M., Sanderson J. J., 1969, Plasma Dynamics. Thomas Nelson and Sons LTD, London

Bromley B. C., Melia F., Liu S., 2001, ApJL, 555, L83

Brown G. E., Bethe H. A., 1994, ApJ, 423, 659

Budden K. G., 1952, Proc. Roy. Soc., 215, 215

Budden K. G., 1961, Radio Waves in the Ionosphere. Cambridge University Press, Cambridge

Budden K. G., Smith M. S., 1976, Royal Society of London Proceedings Series A, 350, 27

Chandrasekhar S., 1960, Radiative transfer. Dover, New York

Chandrasekhar S., 1992, The mathematical theory of black holes. Oxford University Press, New York

Connors P. A., Stark R. F., 1977, Nature, 269, 128

Connors P. A., Stark R. F., Piran T., 1980, ApJ, 235, 224

Dendy R. O., 1990, Plasma Dynamics. Oxford University Press, Oxford

Denn G. R., Mutel R. L., Marscher A. P., 2000, ApJS, 129, 61

Devereux N., Ford H., Tsvetanov Z., Jacoby G., 2003, AJ, 125, 1226

Dovciak M., Bianchi S., Guainazzi M., Karas V., Matt G., 2004, astro-ph/0401607

Eckart A., Baganoff F. K., Morris M., Bautz M. W., Brandt W. N., Garmire G. P., Genzel R., Ott T., Ricker G. R., Straubmeier C., Viehmann T., Schödel R., 2004, astro-ph/0403577

Enßlin T. A., 2003, A&A, 401, 499

Enßlin T. A., Vogt C., 2003, A&A, 401, 835

Fabian A. C., Vaughan S., Nandra K., Iwasawa K., Ballantyne D. R., Lee J. C., De Rosa A., Turner A., Young A. J., 2002, MNRAS, 335, L1

Faraday M., 1846, Phil. Trans. Roy. Soc., 136, 1

Frank J., King A., Raine D., 1992, Accretion Power in Astrophysics. Cambridge University Press, Cambridge

Gammie C. F., McKinney J. C., Tóth G., 2003, ApJ, 589, 444

Gedalin M., Melrose D. B., Gruman E., 1998, Phys. Rev. E, 57, 3399

Genzel R., Schödel R., Ott T., Eckart A., Alexander T., Lacombe F., Rouan D., Aschenbach B., 2003, Nature, 425, 934

Ghez A. M., Salim S., Hornstein S. D., Tanner A., ris M. M., Becklin E. E., Duchene G., 2003, astro-ph/0306130

Ginzburg V. L., 1970, The propagation of electromagnetic waves in plasmas. Pergamon, Oxford

Glass I. S., 1981, MNRAS, 197, 1067

Green A. R., McHardy I. M., Lehto H. J., 1993, MNRAS, 265, 664

Hawley J. F., Balbus S. A., 1995, Publications of the Astronomical Society of Australia, 12, 159

Hawley J. F., Balbus S. A., Stone J. M., 2001, ApJL, 554, L49

Heyl J. S., Shaviv N. J., Lloyd D., 2003, MNRAS, 342, 134

Hodge P. E., 1982, ApJ, 263, 595

Homan D. C., Attridge J. M., Wardle J. F. C., 2001, ApJ, 556, 113

Ichimaru S., 1977, ApJ, 214, 840

Jones T. W., O'Dell S. L., 1977a, ApJ, 214, 522

Jones T. W., O'Dell S. L., 1977b, ApJ, 215, 236

Kellermann K. I., Vermeulen R. C., Zensus J. A., Cohen M. H., 2000, in Hirabayashi H., Edwards P., Murphy D., eds, Astrophysical Phenomena Revealed by Space VLBI Observations of Relativistic Outflow in AGN and the Brightness Temperature of Synchrotron Sources. pp 159–166

Komesaroff M. M., Roberts J. A., Milne D. K., Rayner P. T., Cooke D. J., 1984, MNRAS, 208, 409

Krall N. A., Trivelpiece A. W., 1973, Principles of plasma physics. McGraw-Hill Kogakusha, Tokyo

Krolik J. H., 1999, Active galactic nuclei : from the central black hole to the galactic environment. Princeton University Press, Princeton

Kubo H., Nagata R., 1983, J. Opt. Soc. Am., 73, 1719

Kulsrud R., Loeb A., 1992, Phys. Rev. D, 45, 525

Lai D., Ho W. C., 2003a, Physical Review Letters, 91, 071101

Lai D., Ho W. C. G., 2003b, ApJ, 588, 962

Laor A., Netzer H., Piran T., 1990, MNRAS, 242, 560

Legg M. P. C., Westfold K. C., 1968, ApJ, 154, 499

Lifshitz E. M., Pitaevskii L. P., 1981, Physical kinetics. Pergamon Press, Oxford

Lister M. L., 2001, ApJ, 562, 208

Lloyd D. A., Hernquist L., Heyl J. S., 2003, ApJ, 593, 1024

Macquart J.-P., 2002, Publications of the Astronomical Society of Australia, 19, 43

Macquart J.-P., Melrose D. B., 2000, ApJ, 545, 798

Maoz E., 1998, ApJL, 494, L181

Matt G., Fabian A. C., Reynolds C. S., 1997, MNRAS, 289, 175

McClintock E. J., Remillard R. A., 2003, astro-ph/0306213

McClintock J. E., Narayan R., Garcia M. R., Orosz J. A., Remillard R. A., Murray S. S., 2003, ApJ, 593, 435

Melia F., Falcke H., 2001, ARAA, 39, 309

Melrose D. B., Gedalin M., 2001, Phys. Rev. E, 64, 027401

Melrose D. B., Gedalin M. E., Kennett M. P., Fletcher C. S., 1999, J. Plasma Phys., 62, 233

Miniutti G., Fabian A. C., Goyder R., Lasenby A. N., 2003, MNRAS, 344, L22

Misner C. W., Thorne K. S., Wheeler J. A., 1973, Gravitation. W.H. Freeman and Co., San Francisco

Montgomery D. C., Tidman D. A., 1964, Plasma kinetic theory. McGraw-Hill, New York

Narayan R., Heyl J. S., 2002, ApJL, 574, L139

Narayan R., Mahadevan R., Grindlay J. E., Popham R. G., Gammie C., 1998, ApJ, 492, 554

Papadakis I. E., 2004, MNRAS, 348, 207

Pariev V. I., Bromley B. C., Miller W. A., 2001, ApJ, 547, 649

Petrova S. A., 2000, A&A, 360, 592

Petrova S. A., 2002, A&A, 383, 1067

Rayner D. P., Norris R. P., Sault R. J., 2000, MNRAS, 319, 484

Rees M. J., Phinney E. S., Begelman M. C., Blandford R. D., 1982, Nature, 295, 17

Reynolds C. S., Nowak M. A., 2003, Phys. Rep., 377, 389

Ruszkowski M., Begelman M. C., 2002, ApJ, 573, 485

Rybicki G. B., Lightman A. P., 1979, Radiative processes in astrophysics. Wiley-Interscience, New York

Saikia D. J., Salter C. J., 1988, ARAA, 26, 93

Sault R. J., Macquart J.-P., 1999, ApJL, 526, L85

Sazonov V. N., 1969, JETP, 56, 1075

Sazonov V. N., Tsytovich V. N., 1968, Radiofizika, 11, 1287

Schödel R., Genzel R., Baganoff F. K., Eckart A., 2004, Galactic Center Newsletter, 17, 5

Schödel R., Ott T., Genzel R., Eckart A., Mouawad N., Alexander T., 2003, ApJ, 596, 1015

Schödel R., Ott T., Genzel R., Hofmann R., Lehnert M., Eckart A., Mouawad N., Alexander T., Reid M. J., Lenzen R., Hartung M., Lacombe F., Rouan D., Gendron E., Rousset G., Lagrange A.-M., Brandner W., et al., 2002, Nature, 419, 694

Shapiro S. L., Lightman A. P., Eardley D. M., 1976, ApJ, 204, 187

Shapiro S. L., Teukolsky S. A., 1983, Black holes, white dwarfs, and neutron stars: The physics of compact objects. Wiley-Interscience, New York

Shaviv N. J., Heyl J. S., Lithwick Y., 1999, MNRAS, 306, 333

Stepney S., 1983, MNRAS, 202, 467

Tanaka Y., Nandra K., Fabian A. C., Inoue H., Otani C., Dotani T., Hayashida K., Iwasawa K., Kii T., Kunieda H., Makino F., Matsuoka M., 1995, Nature, 375, 659

Thompson C., Blandford R. D., Evans C. R., Phinney E. S., 1994, ApJ, 422, 304

Timmes F. X., Woosley S. E., Weaver T. A., 1996, ApJ, 457, 834

Torres D. F., Capozziello S., Lambiase G., 2000, Phys. Rev. D, 62, 104012

Urry C. M., Padovani P., 1995, PASP, 107, 803

Van den Heuvel E. P. J., 1992, in Environment Observation and Climate Modelling Through International Space Projects Endpoints of stellar evolution: The incidence of stellar mass black holes in the galaxy. pp 29–36

Walker M., Penrose R., 1970, Commun. math. Phys., 18, 265

Weiler K. W., de Pater I., 1983, ApJS, 52, 293

Weinberg S., 1962, Physical Review, 126, 1899

Weltevrede P., Stappers B. W., van den Horn L. J., Edwards R. T., 2003, A&A, 412, 473

Westfold K. C., 1959, ApJ, 130, 241

Appendix A

Geodesic Motion in the Dispersion Formalism

Given the dispersion relation in equation (4.74),

$$D(k_\mu, x^\mu) = k^\mu k_\mu + m^2 \,,$$

and the ray equations (4.19),

$$\frac{dx^\mu}{d\tau} = \left(\frac{\partial D}{\partial k_\mu}\right)_{x^\mu} \quad \text{and} \quad \frac{dk_\mu}{d\tau} = -\left(\frac{\partial D}{\partial x^\mu}\right)_{k_\mu} ,$$

it is possible to derive the geodesic equation. The partial derivatives on the right side of the ray equations are

$$\left(\frac{\partial D}{\partial k_\mu}\right)_{x^\mu} = 2k^\mu \,, \tag{A.1}$$

and

$$\begin{aligned}\left(\frac{\partial D}{\partial x^\mu}\right)_{k_\mu} &= \left(\frac{\partial k_\alpha k_\beta g^{\alpha\beta}}{\partial x^\mu}\right)_{k_\mu} = k_\alpha k_\beta \frac{\partial g^{\alpha\beta}}{\partial x^\mu} \\ &= -k^\alpha k^\beta g_{\alpha\beta,\mu} \,. \end{aligned} \tag{A.2}$$

Combining the ray equations gives

$$\begin{aligned}
\frac{d^2x^\mu}{d\tau^2} &= 2\frac{dk^\mu}{d\tau} = 2\frac{dk_\nu g^{\mu\nu}}{d\tau} \\
&= 2k_\nu \frac{dx^\alpha}{d\tau}\frac{\partial g^{\mu\nu}}{\partial x^\alpha} + 2g^{\mu\nu}\frac{dk_\mu}{d\tau} \\
&= -4k^\beta k^\alpha g^{\mu\nu} g_{\beta\nu,\alpha} + 2g^{\mu\nu}k^\alpha k^\beta g_{\alpha\beta,\mu} \\
&= -4k^\alpha k^\beta \frac{1}{2} g^{\mu\nu}\left(g_{\alpha\nu,\beta} + g_{\beta\nu,\alpha} - g_{\alpha\beta,\nu}\right) \\
&= -\frac{dx^\alpha}{d\tau}\frac{dx^\beta}{d\tau}\Gamma^\mu_{\alpha\beta}\,, \qquad \text{(A.3)}
\end{aligned}$$

where the definition of the Christoffel symbols were used, $\Gamma^\mu_{\alpha\beta} \equiv \frac{1}{2}g^{\mu\nu}\left(g_{\alpha\nu,\beta} + g_{\beta\nu,\alpha} - g_{\alpha\beta,\nu}\right)$. Collecting terms on the left produces the well-known geodesic equation:

$$\frac{d^2x^\mu}{d\tau^2} + \frac{dx^\alpha}{d\tau}\frac{dx^\beta}{d\tau}\Gamma^\mu_{\alpha\beta} = 0\,,$$

or

$$v^\nu \nabla_\nu v^\mu = 0 \;\text{ where }\; v^\mu \equiv \frac{dx^\mu}{d\tau}\,.$$

Appendix B

A Thick Disk Model

In general, the innermost portions of the accretion flow will take the form of a thick disk. The equation for hydrostatic equilibrium in the limit that $\Omega \gg v_r$ is given by

$$\frac{\partial_\mu P}{\rho + \frac{\Gamma}{\Gamma-1}P} = -\partial_\mu \ln E + \frac{\Omega \partial_\mu L}{1-\Omega L}\,, \tag{B.1}$$

where here Γ is the adiabatic index, $E = -\overline{u}_t$, $\Omega = \overline{u}^\phi/\overline{u}^t$, and $L = -\overline{u}_\phi/\overline{u}_t$ (Blandford & Begelman, 2004, and references therein). Note that, given the metric, any two of the quantities E, Ω, or L, may be derived from the third. Explicitly, Ω and L are related by

$$\Omega = \frac{g^{\phi\phi}L + g^{t\phi}}{g^{tt} + g^{t\phi}L}\,, \tag{B.2}$$

and the condition that $\overline{u}^\mu \overline{u}_\mu = \overline{u}^t \overline{u}_t + \overline{u}^\phi \overline{u}_\phi = -1$ gives E in terms of Ω and L to be

$$E = \left[-\left(g^{tt} + g^{t\phi}L\right)(1-\Omega L)\right]^{-1/2}\,. \tag{B.3}$$

In principle this should be combined with a torque balance equation which explicitly includes the mechanism for angular momentum transport through the disk. However, given a relationship between any two of the quantities E, Ω, and L this is specified automatically. Thus the problem can be significantly simplified if such a relationship can be obtained, presumably from the current MHD disk simulations.

B.1 Barotropic Disks

For a barotropic disk the left side of equation (B.1) can be explicitly integrated to define a function H:

$$H = \int \frac{dP}{\rho(P) + \frac{\Gamma}{\Gamma-1}P}\,, \tag{B.4}$$

which may be explicitly integrated for gases with constant Γ to yield

$$H = \ln\left(1 + \frac{\Gamma}{\Gamma - 1}\frac{P}{\rho}\right)\,. \tag{B.5}$$

Therefore, reorganizing equation (B.1) gives

$$\partial_\mu\left(H + \ln E\right) = \frac{\Omega\partial_\mu L}{1 - \Omega L}\,, \tag{B.6}$$

which in turn implies that Ω is a function of L alone. Specifying this function allows the definition of another function Ξ:

$$\Xi = \int \frac{\Omega(L)dL}{1 - \Omega(L)L}\,. \tag{B.7}$$

Using their definitions, it is possible to solve $\Omega = \Omega(L)$ for $L(x^\mu)$ and hence $\Xi(x^\mu)$. Then H and Ξ are related by

$$H = H_0 + \ln E - \Xi\,, \tag{B.8}$$

which may then be inverted to yield $\rho(H_0 - \ln E + \Xi)$. Inverting H for ρ then yields $\rho(x^\mu)$. The quantity H_0 sets the density scale and may itself be set by choosing ρ at some point:

$$H_0 = H(\rho_0) - (\ln E - \Xi)(x_0^\mu)\,. \tag{B.9}$$

B.1.1 Keplerian Disk

As a simple, but artificial, example of the procedure, a Keplerian disk is briefly considered in the limit of weak gravitating Schwarzschild black hole (i.e., $r \gg M$).

Note that this cannot be done in flat space because in equation (B.1) the gravitational terms are present in the curvature only. For a Keplerian flow, $\Omega = \sqrt{M/(r\sin\theta)^3} \simeq M^2 L^{-3}$. In that case using the definition of Ξ gives

$$\begin{aligned}\Xi &= M^2 \int \frac{dL}{L^3 - M^2 L} \\ &= \int \frac{d\ell}{\ell^3 - \ell} = \ln\sqrt{1-\ell^{-2}}\,,\end{aligned} \tag{B.10}$$

where $\ell = L/M$. $\ln E$ is given by

$$\ln E = -\ln\sqrt{-g^{tt}(1-\Omega L)} = \ln\sqrt{1-\frac{2M}{r}} - \ln\sqrt{1-\ell^{-2}}\,, \tag{B.11}$$

and hence,

$$\begin{aligned}H &= H_0 - \ln E + \Xi \\ &= H_0 - \ln\sqrt{1-\frac{2M}{r}} + \ln\left(1-\ell^{-2}\right) \\ &\simeq H_0 + \frac{M}{r} - \frac{M}{r\sin\theta}\,,\end{aligned} \tag{B.12}$$

where $\ell = \sqrt{r\sin\theta/M}$ and the weakly gravitating condition were used. As expected, along the equatorial plane H, and therefore ρ, is constant. For points outside of the equatorial plane pressure gradients are required to maintain hydrostatic balance.

B.1.2 Pressure Supported Disk

Accretion disks will in general have radial as well as vertical pressure gradients. Inward pressure gradients can support a stable disk between the innermost stable orbit and the photon orbits, thus decreasing the radius of the inner edge of the disk. Around a Schwarzschild black hole this can bring the inner edge of the disk down to $3M$. In a maximally rotating Kerr spacetime this can allow the disk to extend down nearly to the horizon.

Far from the hole, accreting matter will create outward pressure gradients. An

angular momentum profile appropriate for a Kerr hole which goes from being super to sub-Keplerian is

$$L(r_{\rm eq}) = \begin{cases} \left(\sqrt{g^{t\phi}{}_{,r}{}^2 - g^{tt}{}_{,r} g^{\phi\phi}{}_{,r}} - g^{t\phi}{}_{,r} \right) g^{\phi\phi}{}_{,r}{}^{-1} \Big|_{r=r_{\rm eq}} & \text{if } r_{\rm eq} < r_{\rm inner} \\ c_1 M^{3/2} r_{\rm eq}^{-1} + c_2 M^{1/2} + l_0 \sqrt{M r_{\rm eq}} & \text{otherwise} \end{cases}$$

$$\Omega(r_{\rm eq}) = \left. \frac{g^{\phi\phi} L + g^{t\phi}}{g^{tt} + g^{t\phi} L} \right|_{r=r_{\rm eq}} , \tag{B.13}$$

where both L and Ω are parametrized in terms of the equatorial radius, $r_{\rm eq}$. The condition that L reduces to the angular momentum profile of a Keplerian disk for radii less than the inner radius ensures that no pathological disk structures are created within the photon orbit. The constants c_1 and c_2 are defined by the requirement that at the inner edge of the disk, $r_{\rm inner}$, and at the density maximum, $r_{\rm max}$, the angular momentum must equal that of the Keplerian disk. In contrast, l_0 is chosen to fix the large r behavior of the disk. The values chosen here were $r_{\rm inner} = 1.3M$, $r_{\rm max} = 2M$, and $l_0 = 0.1$. The value of H_0 was set so that $H(r_{\rm eq} = 100M) = 0$, thus making the disk extend to $r_{\rm eq} = 100M$.

In addition to defining Ω and L it is necessary to define $P(\rho)$. Because the gas in this portion of the accretion flow is expected to be inefficiently couple the ions and electrons, the pressure will be ion dominated and $\Gamma = 5/3$ was chosen. The proportionality constant in the polytropic equation of state, κ, is set by enforcing the ideal gas law for a given temperature (T_0) at a given density (ρ_0). Thus,

$$P(\rho) = \rho_0 \frac{k T_0}{m_p} \left(\frac{\rho}{\rho_0} \right)^{5/3} . \tag{B.14}$$

Note that ρ_0 and T_0 provide a density and temperature scale. A disk solution obtained for a given ρ_0 and T_0 may be used to generate a disk solution for a different set of scales simply by multiplying the density everywhere by the appropriate constant factor.

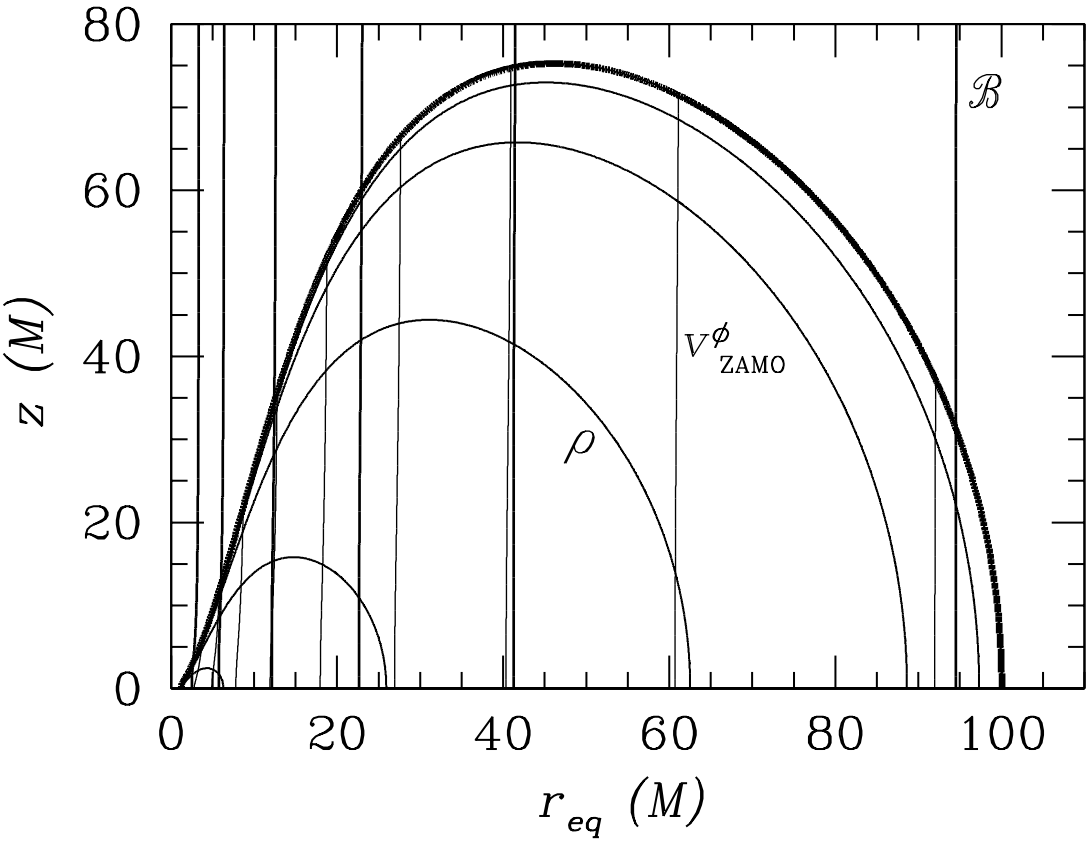

Figure B.1: Shown are the contours of the density and azimuthal velocity as measured by the zero angular momentum observer, and the magnetic field lines. Starting at the density maximum ($r_{\rm eq} = 2M$ and $z = 0$), the density is contoured at levels $10^{-0.5}$ to $10^{-4.5}$ times the maximum density in multiples of 10^{-1}. From left to right, the velocity is contoured at levels $2^{-0.5}c$ to $2^{-5}c$ in multiples of $2^{-0.5}$. In order to provide a distinction between the velocity contours and the magnetic field lines, the velocity contours are terminated at the disks surface.

B.2 Non-Sheared Magnetic Field Geometries

The disk model discussed thus far is purely hydrodynamic. Typically, magnetic fields will also be present. In general, it is necessary to perform a full MHD calculation

in order to self-consistently determine both the plasma and magnetic field structure. However, an approximate steady-state magnetic field can be constructed by requiring that the field lines are not sheared.

To investigate the shearing between two nearby, space-like separated points in the plasma, x_1^μ and x_2^μ, consider the invariant interval between them:

$$\Delta s^2 = \Delta x^\mu \Delta x_\mu \quad \text{where} \quad \Delta x^\mu = x_2^\mu - x_1^\mu \,. \tag{B.15}$$

The condition that this doesn't change in the LFCR frame is equivalent to

$$\frac{d\Delta s^2}{ds} = 0 \,. \tag{B.16}$$

Expanding in terms of the definition of Δs gives

$$\frac{d}{ds} g_{\mu\nu} \Delta x^\mu \Delta x^\nu = g_{\mu\nu,\sigma} \frac{dx^\sigma}{ds} \Delta x^\mu \Delta x^\nu + 2 g_{\mu\nu} \Delta x^\mu \frac{d\Delta x^\nu}{ds} = 0 \,. \tag{B.17}$$

Note that by definition,

$$\frac{dx^\mu}{ds} = \overline{u}^\mu \quad \text{and} \quad \frac{d\Delta x^\mu}{ds} = \overline{u}_2^\mu - \overline{u}_1^\mu = \overline{u}^\mu{}_{,\sigma} \Delta x^\sigma \,. \tag{B.18}$$

Hence,

$$\begin{aligned} \frac{d\Delta s^2}{ds} &= \left(g_{\mu\nu,\sigma} \overline{u}^\sigma + 2 g_{\mu\sigma} \overline{u}^\sigma{}_{,\nu} \right) \Delta x^\mu \Delta x^\nu \\ &= \left(g_{\mu\nu,\sigma} \overline{u}^\sigma + 2 \overline{u}_{\mu,\nu} - 2 g_{\mu\sigma,\nu} \overline{u}^\sigma \right) \Delta x^\mu \Delta x^\nu \\ &= 2 \left(\overline{u}_{\mu,\nu} - \Gamma^\sigma_{\mu\nu} \overline{u}_\sigma \right) \Delta x^\mu \Delta x^\nu \\ &= 2 \left(\nabla_\mu \overline{u}_\nu \right) \Delta x^\mu \Delta x^\nu = 0 \,. \end{aligned} \tag{B.19}$$

The final equality is easy to understand from a geometrical viewpoint; for there to be no shearing, there can be no change in the plasma four-velocity along the direction Δx^μ.

That a stationary, axially symmetric magnetic field must lie upon the non-shearing

surfaces can be seen directly by considering the covariant form of Maxwell's equations. In particular $\nabla_\nu {}^*F^{\mu\nu} = 0$, where ${}^*F^{\mu\nu}$ is the dual of the electromagnetic field tensor, which in the absence of an electric field in the frame of the plasma takes the form ${}^*F^{\mu\nu} = \mathcal{B}^\mu \overline{u}^\nu - \mathcal{B}^\nu \overline{u}^\mu$. Therefore,

$$\begin{aligned} \mathcal{B}_\mu \nabla_\nu {}^*F^{\mu\nu} &= \mathcal{B}_\mu \mathcal{B}^\mu \nabla_\nu \overline{u}^\nu + \mathcal{B}_\mu \overline{u}^\nu \nabla_\nu \mathcal{B}^\mu \\ &\quad - \mathcal{B}_\mu \overline{u}^\mu \nabla_\nu \mathcal{B}^\nu - \mathcal{B}_\mu \mathcal{B}^\nu \nabla_\nu \overline{u}^\mu \\ &= -\mathcal{B}^\mu \mathcal{B}^\nu \nabla_\nu \overline{u}_\mu = 0 \,, \end{aligned} \tag{B.20}$$

where the first three terms vanish due to axial symmetry and the requirement that $\mathcal{B}^\mu \overline{u}_\mu = 0$. This is precisely the non-shearing condition obtained in equation (B.19).

For plasma flows that are directed along Killing vectors of the spacetime, ξ_i^μ, i.e.,

$$\overline{u}^\mu = u^t t^\mu + \sum_i u^i \xi_i^\mu \,, \tag{B.21}$$

where t^μ is the time-like Killing vector, it is possible to simplify the no-shear condition considerably.

$$\begin{aligned} \Delta x^\mu \Delta x_\nu \nabla_\mu \overline{u}^\nu &= \Delta x^\mu \Delta x_\nu \left(u^t \nabla_\mu t^\nu + \sum_i u^i \nabla_\mu \xi_i^\nu \right) \\ &\quad + \Delta x^\mu \Delta x_\nu \left(t^\nu \partial_\mu u^t + \sum_i \xi_i^\nu \partial_\mu u^i \right) \\ &= \Delta x_t \Delta x^\mu \partial_\mu u^t + \sum_i \Delta x_i \Delta x^\mu \partial_\mu u^i = 0 \,, \end{aligned} \tag{B.22}$$

where terms in the first parentheses vanish due to Killing's equation. The additional constraint that $\Delta x_\mu \overline{u}^\mu = 0$ gives

$$\Delta x_t = -\sum_i \Omega_i \Delta x_i \,, \tag{B.23}$$

where $\Omega_i \equiv u^i / u^t$ is a generalization of the definition of the Ω defined at the beginning

of this Appendix. Inserting this into equation (B.22) and simplifying yields

$$\sum_i \Delta x_i \Delta x^\mu \partial_\mu \Omega_i = 0\,, \tag{B.24}$$

i.e., the no shear hypersurfaces are those upon which all of the Ω_i are constant.

For the plasma flows considered in Section B.1 the plasma velocity is in the form of equation (B.21) where the space-like Killing vector is that associated with the axial symmetry, ϕ^μ. Thus with $\Omega_\phi = \Omega$, the no-shear condition for this class of plasma flows is

$$\Delta x^\mu \partial_\mu \Omega = 0\,. \tag{B.25}$$

Note that while we have been considering only axially symmetric plasma flows, this no shear condition is more generally valid, extending to the case where Ω is a function of t and ϕ as well as r and θ. However, in this case it is not the perfect-MHD limit of Maxwell's equations.

For a cylindrically symmetric disk, the no-shear condition may be used to explicitly construct the non-shearing poloidal magnetic fields by setting

$$\mathcal{B}^r = \mathcal{B}\Omega_{,\theta} \quad \text{and} \quad \mathcal{B}^\theta = -\mathcal{B}\Omega_{,r}\,. \tag{B.26}$$

Once the magnitude of $\mathcal{B}^\mu$ is determined at some point along each non-shearing surfaces (e.g., in the equatorial plane), it may be set everywhere by $\nabla_\mu \mathcal{B}^\mu - \mathcal{B}^\mu \overline{u}^\nu \nabla_\nu \overline{u}_\mu = 0$, which comes directly from Maxwell's equations in covariant form and $\mathcal{B}^\mu \overline{u}_\mu = 0$. Inserting the form in equation (B.26) into the first term gives

$$\begin{aligned}
\nabla_\mu \mathcal{B}^\mu &= \frac{1}{\sqrt{g}} \partial_\nu \sqrt{g} \mathcal{B}^\nu \\
&= \frac{1}{\sqrt{g}} \left(\partial_r \sqrt{g} \mathcal{B} \Omega_{,\theta} - \partial_\theta \sqrt{g} \mathcal{B} \Omega_{,r} \right) \\
&= \frac{1}{\sqrt{g}} \left(\Omega_{,\theta} \partial_r \sqrt{g} \mathcal{B} - \Omega_{,r} \partial_\theta \sqrt{g} \mathcal{B} \right) \\
&= \mathcal{B}^\nu \partial_\nu \ln \sqrt{g} \mathcal{B}\,.
\end{aligned} \tag{B.27}$$

The second term can be simplified using equation (B.21),

$$\begin{aligned}
\mathcal{B}^\mu \overline{u}^\nu \nabla_\nu \overline{u}_\mu &= \mathcal{B}^\mu \overline{u}^\nu \nabla_\nu \left(u^t t_\mu + u^\phi \phi_\mu \right) \\
&= \mathcal{B}^\mu \overline{u}^\nu \left(t_\mu \partial_\nu u^t + \phi_\mu \partial_\nu u^\phi - u^t \nabla_\mu t_\nu - u^\phi \nabla_\mu \phi_\nu \right) \\
&= \mathcal{B}_t \overline{u}^\nu \partial_\nu u^t + \mathcal{B}_\phi \overline{u}^\nu \partial_\nu u^\phi + \mathcal{B}^\mu \overline{u}^\nu \left(t_\nu \partial_\mu u^t \phi_\nu \partial_\mu u^\phi \right) + \mathcal{B}^\mu \overline{u}^\nu \nabla_\mu \overline{u}_\nu \\
&= \mathcal{B}^\mu \left(\overline{u}_t \partial_\mu u^t + \overline{u}_\phi \partial_\mu u^t \Omega \right) \\
&= \mathcal{B}^\mu \left(\overline{u}_t + \Omega \overline{u}_\phi \right) \partial_\mu u^t + \overline{u}_\phi u^t \mathcal{B}^\mu \partial_\mu \Omega \\
&= -\mathcal{B}^\mu \partial_\mu \ln u^t \,, \qquad \text{(B.28)}
\end{aligned}$$

where the stationarity and axially symmetry have been used in the third step and the no-shear condition was used in the final step. Therefore, the magnitude $\mathcal{B}$ can be determined by

$$\begin{aligned}
\nabla_\mu \mathcal{B}^\mu - \mathcal{B}^\mu \overline{u}^\nu \nabla_\nu \overline{u}_\mu &= \mathcal{B}^\mu \partial_\mu \ln \sqrt{g} \mathcal{B} - \mathcal{B}^\mu \partial_\mu \ln u^t \\
&= \mathcal{B}^\mu \partial_\mu \ln \frac{\sqrt{g} \mathcal{B}}{u^t} = 0 \,, \qquad \text{(B.29)}
\end{aligned}$$

and hence

$$\frac{\sqrt{g} \mathcal{B}}{u^t} = \text{constant} \qquad \text{(B.30)}$$

along the non-shearing surfaces. If $\mathcal{B}$ is given along a curve which passes through all of the non-shearing surfaces (e.g., in the equatorial plane), $\mathcal{B}^\mu$ is defined everywhere through equations (B.26) and (B.30).

B.2.1 Non-Shearing Magnetic Fields in a Cylindrical Flow

An example application of this formalism is a cylindrical flow in flat space. In this case, Ω is a function of the cylindrical radius $\varpi \equiv r \sin\theta$. The Keplerian disk is a specific example with $\Omega = \varpi^{-3/2}$. The direction of the magnetic field is determined by

$$\Omega_{,r} = \frac{d\Omega}{d\varpi} \sin\theta \qquad \text{and} \qquad \Omega_{,\theta} = \frac{d\Omega}{d\varpi} r \cos\theta \,. \qquad \text{(B.31)}$$

The magnitude, $\mathcal{B}$ is given by

$$\frac{r^2 \sin\theta}{\sqrt{1 - r^2 \sin^2\theta \Omega^2}} \mathcal{B} = f(\Omega)\,, \tag{B.32}$$

and thus

$$\mathcal{B} = \frac{1}{r} b(\varpi)\,, \tag{B.33}$$

where the particular form of $b(\varpi)$ depends upon the particular form of $f(\Omega)$. Therefore,

$$\mathcal{B}^r = b(\varpi)\cos\theta \qquad \text{and} \qquad \mathcal{B}^\theta = -b(\varpi)\frac{1}{r}\sin\theta\,, \tag{B.34}$$

which is precisely the form of a cylindrically symmetric vertical magnetic field.

B.2.2 Stability to the Magneto-Rotational Instability

A sufficiently strong non-shearing magnetic field configuration will remain stable to the magneto-rotational instability (MRI). The criterion for instability to the MRI is

$$\left(\mathbf{k} \cdot \mathbf{v}_\mathrm{A}\right)^2 < -r\frac{d\Omega^2}{dr}\,, \tag{B.35}$$

where $\mathbf{k}$ is the wave vector of the unstable mode and $\mathbf{v}_\mathrm{A}$ is the Alfvén velocity (Hawley & Balbus, 1995). For a nearly vertical magnetic field geometry, stability will be maintained if modes with wavelength less than twice the disk height (h) are not unstable. With

$$v_\mathrm{A} = \frac{B}{\sqrt{4\pi\rho}} = \frac{\omega_B}{\omega_P}\sqrt{\frac{m_e}{m_p}}\,c\,, \tag{B.36}$$

a Keplerian disk will be stable if

$$\frac{4\pi}{h}\frac{\omega_B}{\omega_P}\sqrt{\frac{m_e}{m_p}}\,c > \sqrt{3}\left(\frac{M}{r}\right)^{3/2}\frac{c}{M}\,. \tag{B.37}$$

A conservative criterion may be obtained by approximating $h \simeq h_0 r$ for some constant of proportionality h_0, hence

$$\frac{\omega_B}{\omega_P} \gtrsim 6h_0\sqrt{\frac{M}{r}} \simeq 0.3\,, \tag{B.38}$$

for $h_0 \simeq 0.1$ and $r \simeq 7$ which are typical for the disk pictured in Figure B.1.

Comparison to equipartion fields can provide some insight into how unrestrictive the stability criterion really is. Given $\beta = P_{\rm gas}/P_{\rm mag}$ and the ideal gas law it is straight forward to show that

$$\frac{\omega_B}{\omega_P} = \sqrt{\frac{2kT}{\beta m_e c^2}} \simeq \sqrt{3\beta^{-1}T_{10}}\,, \tag{B.39}$$

where T is the ion temperature. Because the ion temperature in a thick disk will typically be on the order of or exceed 10^{12} K, the equipartition ω_B ($\beta = 1$) will be at least an order of magnitude larger than ω_P. As a result the field needed to stabilize the disk against the MRI is an order of magnitude less than equipartition strength, and hence is not physically unreasonable.

B.2.3 Magnetic Field Model

Considering the restriction placed upon the magnetic field strength discussed in the previous sections, $\mathcal{B}$ was set such that in the equatorial plane

$$\omega_B = \omega_P + \eta\,(r + 10M)^{-5/4}\,, \tag{B.40}$$

where the second term provides a canonical scaling at large radii. Here η was chosen to be 0.01.

Appendix C

Radiative Transfer Regimes

In general, Maxwell's equations give

$$\left(\nabla^2 - \nabla\nabla + \omega^2\epsilon\right) \cdot \mathbf{E} = 0\,, \tag{C.1}$$

for an electric field $\mathbf{E}$, and a dielectric tensor ϵ. For plane waves propagating along the z-axis in a plane parallel medium, this reduces to

$$\frac{d^2\mathbf{F}}{dz^2} + \omega^2\epsilon \cdot \mathbf{F} = 0\,, \tag{C.2}$$

where $\mathbf{F}$ is the Jone's vector (i.e., a two-dimensional vector constructed from the transverse components of $\mathbf{E}$). For an anisotropic dielectric tensor, there will exist two nondegenerate transverse modes defined such that

$$\omega^2\epsilon\mathbf{F}_i = k_i^2\mathbf{F}_i\,. \tag{C.3}$$

In the case of a plasma, these are in general elliptically polarized, i.e.,

$$\mathbf{F}_1 = \mathbf{Q}\begin{pmatrix} \sin\chi \\ i\cos\chi \end{pmatrix} \quad \text{and} \quad \mathbf{F}_2 = \mathbf{Q}\begin{pmatrix} \cos\chi \\ -i\sin\chi \end{pmatrix}\,, \tag{C.4}$$

where the orientation of the polarization ellipses is determined by

$$\mathbf{Q} = \begin{pmatrix} \cos\phi & \sin\phi \\ -\sin\phi & \cos\phi \end{pmatrix} . \tag{C.5}$$

Then, $\mathbf{F} = F_1\mathbf{F}_1 + F_2\mathbf{F}_2$, may be inserted into equation (C.2) to give

$$\begin{aligned} F_1'' + 2is_2\varphi F_1' + \left(k_1^2 - \varphi^2 - \psi^2 + is_2\varphi' + 2ic_2\varphi\psi\right) F_1 \\ = 2\left(\psi - ic_2\varphi\right) F_2' + \left(\psi' - ic_2\varphi' + 2is_2\varphi\psi\right) F_2 \\ F_2'' - 2is_2\varphi F_2' + \left(k_2^2 - \varphi^2 - \psi^2 - is_2\varphi' - 2ic_2\varphi\psi\right) F_2 \\ = -2\left(\psi + ic_2\varphi\right) F_1' - \left(\psi' + ic_2\varphi' - 2is_2\varphi\psi\right) F_1 , \end{aligned} \tag{C.6}$$

where a prime denotes differentiation with respect to z, c_2 and s_2 are $\cos 2\chi$ and $\sin 2\chi$, respectively, and

$$\varphi = \frac{d\phi}{dz} \quad \text{and} \quad \psi = \frac{d\chi}{dz} . \tag{C.7}$$

When $\varphi = 0$, these reproduce Försterling's coupled equations (cf. Budden, 1961; Ginzburg, 1970).

Thus far, no approximations have been made regarding the wave length or scale lengths of the plasma. From the form of equations (C.6), it is clear that if ϕ and ψ vanish, the two modes will propagate completely independently. In the limit that φ and ψ are small in comparison to $k_{1,2}$, we may look for solutions of the form

$$F_i = \frac{f_i}{\sqrt{k_i}} \, \mathrm{e}^{i\int k_i dz} , \tag{C.8}$$

and hence

$$\begin{aligned} f_1' + is_2\varphi f_1 &= \left(\psi - ic_2\varphi\right) f_2 \, \mathrm{e}^{-i\int \Delta k dz} \\ f_2' - is_2\varphi f_2 &= -\left(\psi + ic_2\varphi\right) f_1 \, \mathrm{e}^{i\int \Delta k dz} , \end{aligned} \tag{C.9}$$

where terms on the order of ψ^2, φ^2, ψ', φ', $\psi\varphi$, and f_i'' were ignored as they are small

by assumption relative to those that remain. Further expand the f_i as

$$f_1 = u_1 \mathrm{e}^{-i\int(\Delta k/2)dz} \quad \text{and} \quad f_2 = u_2 \mathrm{e}^{i\int(\Delta k/2)dz}\,. \tag{C.10}$$

Then,

$$\begin{aligned} u_1' - i\left(\frac{\Delta k}{2} - s_2\varphi\right) u_1 &= (\psi - ic_2\varphi)\, u_2 \\ u_2' + i\left(\frac{\Delta k}{2} - s_2\varphi\right) u_2 &= -(\psi + ic_2\varphi)\, u_1\,, \end{aligned} \tag{C.11}$$

which may be combined to give

$$\begin{aligned} u_1'' + \left[\left(\frac{\Delta k}{2}\right)^2 + \psi^2 + \varphi^2 - s_2\varphi\Delta k - i\frac{\Delta k'}{2}\right] u_1 &= 0 \\ u_2'' + \left[\left(\frac{\Delta k}{2}\right)^2 + \psi^2 + \varphi^2 - s_2\varphi\Delta k + i\frac{\Delta k'}{2}\right] u_2 &= 0\,. \end{aligned} \tag{C.12}$$

If the ψ and φ terms are dominated by the Δk terms, then

$$u_{1,2} \simeq \text{const} \times \mathrm{e}^{\pm i\int(\Delta k/2)dz}\,, \tag{C.13}$$

and thus the f_i are constant. Therefore, in this limit the modes propagate independently (the so-called adiabatic regime). In the opposing limit, when ψ and φ dominate Δk, then equations (C.12) are indistinguishable from the isotropic case (i.e., $\Delta k = 0$), and therefore the polarization propagates unaltered (the so-called strongly coupled regime). This can be directly proved by solving for $u_{1,2}$ in this limit and expressing the answer in terms of $\mathbf{F}$.

In general, for the scenarios considered here $\Delta k' \ll (\Delta k)^2$, and thus this term may be safely ignored. Since the $\varphi\Delta k$ term will only be relevant when

$$\left(\frac{\Delta k}{2}\right) \sim \psi^2 + \varphi^2\,, \tag{C.14}$$

this term may also be neglected in determining the limiting regimes. Therefore, the

two distinct polarization transfer regimes are denoted by

$$\begin{aligned} \sqrt{\left|\frac{d\chi}{dz}\right|^2 + \left|\frac{d\phi}{dz}\right|^2} &\ll \left|\frac{\Delta k}{2}\right| && \text{adiabatic} \\ \sqrt{\left|\frac{d\chi}{dz}\right|^2 + \left|\frac{d\phi}{dz}\right|^2} &\gg \left|\frac{\Delta k}{2}\right| && \text{strongly coupled}\,, \end{aligned} \tag{C.15}$$

where the definitions of ψ and φ have been used.

Appendix D

Polarized Radiative Transfer Equation

D.1 Relation between Evolution of the Stokes Parameters and the Electric Field Vector

In the WKB limit, the propagation equation for the components of the electric field vector transverse to the wave-vector ($\mathbf{F}$) can be written in the form

$$\frac{d\mathbf{F}}{dz} = \mathbf{T} \cdot \mathbf{F}\,, \tag{D.1}$$

where $\mathbf{T}$ is a two-dimensional matrix. This may be expanded in terms of the basis of Pauli matrices and the identity:

$$\begin{aligned} \sigma_0 &= \begin{pmatrix} 1 & 0 \\ 0 & 1 \end{pmatrix}\,, \qquad \sigma_1 = \begin{pmatrix} 1 & 0 \\ 0 & -1 \end{pmatrix} \\ \sigma_2 &= \begin{pmatrix} 0 & 1 \\ 1 & 0 \end{pmatrix}\,, \qquad \sigma_3 = \begin{pmatrix} 0 & -i \\ i & 0 \end{pmatrix}\,, \end{aligned} \tag{D.2}$$

to give

$$\frac{d\mathbf{F}}{dz} = \sum_{j=0}^{3} (a_j + ib_j)\sigma_j \cdot \mathbf{F}\,. \tag{D.3}$$

It is well-known that in terms of the basis σ_j the Stokes parameters are given by

$$S_j = \mathbf{F}^\dagger \cdot \sigma_j \cdot \mathbf{F}\,, \tag{D.4}$$

where $\mathbf{S} = (I, Q, U, V)$. As a direct result,

$$\begin{aligned}\frac{dS_j}{dz} &= \frac{d\mathbf{F}^\dagger}{dz} \cdot \sigma_j \cdot \mathbf{F} + \mathbf{F}^\dagger \cdot \sigma_j \cdot \frac{d\mathbf{F}}{dz} \\ &= \mathbf{F}^\dagger \cdot \{\mathbf{T}, \sigma_j\} \cdot \mathbf{F} \\ &= \mathbf{F}^\dagger \cdot \sum_{k=0}^{3} \left(a_k \{\sigma_k, \sigma_j\} + i b_k [\sigma_j, \sigma_k]\right) \cdot \mathbf{F}\,. \end{aligned} \tag{D.5}$$

Therefore, in terms of the a_j and b_j, the radiative transfer equation is given by

$$\frac{d}{dz}\begin{pmatrix} S_0 \\ S_1 \\ S_2 \\ S_3 \end{pmatrix} = 2\begin{pmatrix} a_0 & a_1 & a_2 & a_3 \\ a_1 & a_0 & b_3 & -b_2 \\ a_2 & -b_3 & a_0 & b_1 \\ a_3 & b_2 & -b_1 & a_0 \end{pmatrix}\begin{pmatrix} S_0 \\ S_1 \\ S_2 \\ S_3 \end{pmatrix}, \tag{D.6}$$

as shown in Kubo & Nagata, 1983 (note that there is no contribution due to the phase b_0). Hence the primary difficulty is writing the propagation equation for the electric field in the form of equation (D.1).

D.2 Linearized Evolution Equation for the Electric Field Vector in a Weakly Refractive, Anisotropic Medium

In general equation (D.1) can be obtained by making a WKB expansion of Maxwell's equations. Here we present a derivation applicable to environments with disorganized, stationary magnetic fields in the non-refractive limit. Explicitly, Maxwell's equations

give the following for the electric field vector ($\mathbf{E}$)

$$\left(\nabla^2 - \nabla\nabla + \omega^2\epsilon\right) \cdot \mathbf{E} = 0\,, \tag{D.7}$$

assuming that all modes have the same $\exp(i\omega t)$ dependence. The WKB expansion assumes that $\mathbf{E}$ can be written as a quickly varying phase (Φ_j), a slowly varying amplitude (A_j), and a slowly varying basis vector ($\hat{\mathbf{E}}_j$),

$$\mathbf{E} = \sum_j e^{i\Phi_j} A_j \hat{\mathbf{E}}_j\,, \tag{D.8}$$

where the summation is over all the possible polarization modes. To zeroth order in the WKB expansion

$$\omega^2 \left(1 + \epsilon\right) \cdot \hat{\mathbf{E}} = \sum_j \left(k_j^2 - \mathbf{k}_j\mathbf{k}_j\right) \cdot \hat{\mathbf{E}}_j\,, \tag{D.9}$$

where $\mathbf{k}_j = \nabla\Phi_j$. To first order in the WKB expansion we find

$$\sum_j i\left(2\mathbf{k}_j \cdot \nabla - \mathbf{k}_j\nabla - \nabla\mathbf{k}_j\right) \cdot A_j\hat{\mathbf{E}}_j = \\ - \sum_j \left[i\left(\nabla \cdot \mathbf{k}_j\right) + 2\left(k_j^2 - \mathbf{k}_j\mathbf{k}_j\right)\right] \cdot A_j\hat{\mathbf{E}}_j\,, \tag{D.10}$$

where the zeroth-order result was used.

If the rays are weakly refracted then

$$\left(1 - \hat{\mathbf{k}}_j\hat{\mathbf{k}}_j\right)\mathbf{k}_j \cdot \nabla \simeq \mathbf{k}_j \cdot \nabla\left(1 - \hat{\mathbf{k}}_j\hat{\mathbf{k}}_j\right)\,. \tag{D.11}$$

This is a direct consequence of the fact that in this case the rays will follow geodesics.

Additionally,

$$\begin{aligned}\left(1-\hat{\mathbf{k}}_j\hat{\mathbf{k}}_j\right)\cdot\mathbf{k}_j\nabla &= 0\\ \left(1-\hat{\mathbf{k}}_j\hat{\mathbf{k}}_j\right)\cdot\nabla\mathbf{k}_j &\simeq 0\\ \nabla\cdot\mathbf{k}_j &\simeq 0\,,\end{aligned} \tag{D.12}$$

where the first is identically true and the others follows from the weakly refractive condition. As a result,

$$\sum_j k_j\hat{\mathbf{k}}\cdot\nabla\cdot\overline{A}_j\hat{\mathbf{F}}_j = \sum_j ik_j^2\overline{A}_j\hat{\mathbf{F}}_j\,, \tag{D.13}$$

where $\hat{\mathbf{F}}_j$ are the properly normalized, transverse components of the polarization eigenmodes (the normalization is absorbed into the $\overline{A}_j$.) Note that inherent in the WKB expansion it is assumed that the polarization eigenmodes propagate independently. The conditions for this to be true are outlined in Section 8.2. In the case of a lossless, anisotropic dielectric tensor it can be shown that the $\hat{\mathbf{F}}_j$ are unique and have differing wave-numbers. It can also be shown that they are necessarily orthogonal, despite the fact that if the dielectric tensor is spatially dispersive the different polarization modes are eigenmodes of different tensors (see, e.g., Section 5.4). As a result, the projection operator for the jth polarization mode is defined by

$$\mathbf{P}_j = \hat{\mathbf{F}}_j\hat{\mathbf{F}}_j^\dagger\,. \tag{D.14}$$

Therefore, with

$$\mathbf{F} = \sum_j \overline{A}_j\hat{\mathbf{F}}_j\,, \tag{D.15}$$

the individual contributions from each polarization mode can be obtained by

$$\overline{A}_j\hat{\mathbf{F}}_j = \mathbf{P}_j\cdot\mathbf{F}\,. \tag{D.16}$$

This may be inserted into equation (D.13) to yield

$$\left(\sum_j k_j \mathbf{P}_j\right) \hat{\mathbf{k}} \cdot \nabla \mathbf{F} = \left\{\sum_j \left[ik_j^2 \mathbf{P}_j - k_j \left(\hat{\mathbf{k}} \cdot \nabla \mathbf{P}_j\right)\right]\right\} \cdot \mathbf{F}\,. \tag{D.17}$$

The inverse of $\left(\sum_j k_j \mathbf{P}_j\right)$ exists and is trivially given by $\left(\sum_j k_j^{-1} \mathbf{P}_j\right)$. Therefore, in the form of equation (D.1),

$$\frac{d\mathbf{F}}{dz} = \left[\sum_j \left(ik_j \mathbf{P}_j - \sum_l \frac{k_l}{k_j} \mathbf{P}_j \cdot \frac{d\mathbf{P}_l}{dz}\right)\right] \cdot \mathbf{F}\,, \tag{D.18}$$

where z is chosen such that $\hat{\mathbf{k}} \cdot \nabla = d/dz$. The two polarization eigenmodes are directly coupled via the $d\mathbf{P}_l/dz$ in equation (D.18). As will be discussed in Chapter 8.2, the modes will necessarily be strongly coupled when the typical length scale over which the polarization changes is short in comparison the the Faraday rotation length. In the opposing limit (the adiabatic limit), the modes will propagate independently. The $d\mathbf{P}_l/dz$ term in equation (D.18) is the lowest-order coupling correction to the adiabatic limit. While in general this term will be small in comparison to $k_j \mathbf{P}_j$, as shown in the following sections, there are scenarios in which it can dominate the polarimetric properties of an astrophysical system.

In general the polarization can be described by a polarization angle (ϕ) and the degree of ellipticity. It is commonly useful to define the Stokes parameters with respect to a basis rotated such that $\phi = 0$ (e.g., one basis vector is rotated such that it is aligned with the magnetic field at all points along the line of sight). This can be included in equation (D.18) by setting $\mathbf{F} = \mathbf{Q} \cdot \mathbf{F}'$ where $\mathbf{F}'$ is the polarization in the rotated basis and

$$\mathbf{Q} \equiv \begin{pmatrix} \cos\phi & \sin\phi \\ -\sin\phi & \cos\phi \end{pmatrix}\,. \tag{D.19}$$

This transformation enforces a symmetry that causes a_2 vanish identically. Therefore,

$$\frac{d\mathbf{F}'}{dz} = \left[\sum_j \left(ik_j \mathbf{P}'_j - \sum_l \frac{k_l}{k_j} \mathbf{P}'_j \cdot \frac{d\mathbf{P}'_l}{dz}\right) - \mathbf{Q}^{-1} \frac{d\mathbf{Q}}{dz}\right] \cdot \mathbf{F}'\,, \tag{D.20}$$

where the primes denote quantities calculated in the rotated basis. For the $\mathbf{Q}$ given, $\mathbf{Q}^{-1}d\mathbf{Q}/dz = i(d\phi/dz)\sigma_3$, giving the well-known geometric analogue to Faraday rotation.

The ellipticity can be parametrized in terms of an angle (χ) giving

$$\mathbf{F}'_1 = \begin{pmatrix} \sin\chi \\ i\cos\chi \end{pmatrix} \quad \text{and} \quad \mathbf{F}'_2 = \begin{pmatrix} \cos\chi \\ -i\sin\chi \end{pmatrix} . \tag{D.21}$$

The subsequent projection operators are then given by

$$\mathbf{P}'_{1,2} = \frac{1}{2}\left(1 \pm \mathbf{M}\right) , \tag{D.22}$$

where

$$\begin{aligned} \mathbf{M} &\equiv \begin{pmatrix} -\cos 2\chi & -i\sin 2\chi \\ i\sin 2\chi & \cos 2\chi \end{pmatrix} \\ &= -\cos 2\chi\sigma_1 + \sin 2\chi\sigma_3 . \end{aligned} \tag{D.23}$$

In addition it is necessary to calculate $d\mathbf{P}_j/dz$ as these are what lead to the geometric phase effects in equation (D.18) (in addition to those introduced via $d\mathbf{Q}/dz$). Hence,

$$\begin{aligned} \frac{d\mathbf{P}'_{1,2}}{dz} &= \pm\frac{1}{2}\frac{d\mathbf{M}}{dz} \\ &= \pm\left(\sin 2\chi\sigma_1 + \cos 2\chi\sigma_3\right)\frac{d\chi}{dz} , \end{aligned} \tag{D.24}$$

As a result,

$$\begin{aligned}
&\sum_j \left(ik_j \mathbf{P}'_j - \sum_l \frac{k_l}{k_j} \mathbf{P}'_j \cdot \frac{d\mathbf{P}'_l}{dz} \right) \\
&\quad = \frac{i}{2}(k_1 + k_2) + \frac{i}{2}(k_1 - k_2)\,\mathbf{M} - \frac{(k_1 - k_2)^2}{4k_1 k_2}\mathbf{M} \cdot \frac{d\mathbf{M}}{dz} + \frac{k_1^2 - k_2^2}{4k_1 k_2}\frac{d\mathbf{M}}{dz} \\
&\quad = \frac{i}{2}(k_1 + k_2)\,\sigma_0 + \left[\frac{k_1^2 - k_2^2}{2k_1 k_2} \sin 2\chi \frac{d\chi}{dz} - \frac{i}{2}(k_1 - k_2)\cos 2\chi \right] \sigma_1 \\
&\qquad - i\frac{(k_1 - k_2)^2}{2k_1 k_2}\frac{d\chi}{dz}\sigma_2 + \left[\frac{k_1^2 - k_2^2}{2k_1 k_2} \cos 2\chi \frac{d\chi}{dz} + \frac{i}{2}(k_1 - k_2)\sin 2\chi \right] \sigma_3 \,. \qquad \text{(D.25)}
\end{aligned}$$

Therefore, the nonzero a_j and b_j are

$$\begin{aligned}
a_1 &= \frac{k_1^2 - k_2^2}{2k_1 k_2} \sin 2\chi \frac{d\chi}{dz} \\
a_3 &= \frac{k_1^2 - k_2^2}{2k_1 k_2} \cos 2\chi \frac{d\chi}{dz} \\
b_0 &= \frac{1}{2}(k_1 + k_2) \\
b_1 &= -\frac{1}{2}(k_1 - k_2)\cos 2\chi \\
b_2 &= -\frac{(k_1 - k_2)^2}{2k_1 k_2}\frac{d\chi}{dz} \\
b_3 &= \frac{1}{2}(k_1 - k_2)\sin 2\chi + \frac{d\phi}{dz} \,. \qquad \text{(D.26)}
\end{aligned}$$

Faraday conversion and rotation are due to b_1 and b_3, respectively. Note that, it is also possible to convert Stokes Q directly to Stokes V as a result of b_2. In addition, there are two dichroic terms, a_1 and a_3 which couple Stokes I to Stokes Q and V.

Note that for $\Delta k \equiv k_1 - k_2 \ll k \equiv (k_1 + k_2)/2$,

$$\begin{aligned}
a_1 &= \frac{\Delta k}{k} \sin 2\chi \frac{d\chi}{dz} \\
a_3 &= \frac{\Delta k}{k} \cos 2\chi \frac{d\chi}{dz} \\
b_0 &= k \\
b_1 &= -\frac{1}{2} \Delta k \cos 2\chi \\
b_2 &= -\frac{1}{2} \left(\frac{\Delta k}{k} \right)^2 \frac{d\chi}{dz} \\
b_3 &= \frac{1}{2} \Delta k \sin 2\chi + \frac{d\phi}{dz} \,,
\end{aligned} \tag{D.27}$$

thus with equation (8.1), in the adiabatic regime, a_1 and a_3 are at least a factor of $\Delta k/k$ smaller than b_1 and b_3, while b_2 is at least a factor of $\Delta k/k$ smaller than this. As a result, to the level of approximations made in the determination of equations (D.27), these terms may be neglected. However, geometric terms persist in the additional term in b_3 and in the adiabatic condition.

Appendix E

Components of the Transfer Matrix for a Magnetized Plasma

In astrophysical environments, the typical source of anisotropy in the polarization eigenmodes is a magnetized plasma. In the high-frequency limit,

$$\Delta k \equiv k_1 - k_2 \simeq \frac{\omega}{c} XY \cos\theta \equiv \delta k \mu \,, \tag{E.1}$$

where X and Y are the square of the ratio of the plasma frequency to ω and the ratio of the cyclotron frequency to ω, respectively, θ is the angle between the line of sight and the magnetic field, $\delta k \equiv \omega XY/c$, and $\mu \equiv \cos\theta$. The ellipticity angle is given by (see, e.g., Ginzburg, 1970; Budden, 1961)

$$\cot\chi = x + \sqrt{1+x^2} \quad \text{where} \quad x \equiv \frac{Y\sin^2\theta}{2\,(1-X)\cos\theta} \,. \tag{E.2}$$

As a direct result, $\cot 2\chi = x$ and therefore,

$$\sin 2\chi = \frac{\operatorname{sgn} x}{\sqrt{1+x^2}} \simeq \frac{\mu}{\sqrt{(Y/2)^2+\mu^2}}$$

$$\cos 2\chi = \frac{|x|}{\sqrt{1+x^2}} \simeq \frac{Y}{2}\frac{1-\mu^2}{\sqrt{(Y/2)^2+\mu^2}}$$

$$\frac{d\chi}{dz} = -\frac{1}{2}\left(1+x^2\right)^{-1}\frac{dx}{dz} \simeq -\frac{Y}{4}\sqrt{1-\mu^2}\frac{1+\mu^2}{(Y/2)^2+\mu^2}\frac{d\theta}{dz} \,, \tag{E.3}$$

where the $\operatorname{sgn} x$ is necessary to choose the correct root, and the expressions for μ assume that $Y \ll 1$. Therefore,

$$b_1 = -\frac{1}{2}\Delta k \frac{|x|}{\sqrt{1+x^2}} \simeq -\frac{1}{2}\Delta k \frac{Y}{2} \frac{1-\mu^2}{\sqrt{(Y/2)^2+\mu^2}}$$

$$b_3 = \frac{1}{2}\Delta k \left(\frac{\operatorname{sgn} x}{\sqrt{1+x^2}} + \frac{2}{\Delta k}\frac{d\phi}{dz} \right) \simeq \frac{1}{2}\Delta k \left(\frac{\mu}{\sqrt{(Y/2)^2+\mu^2}} + \frac{2}{\Delta k}\frac{d\phi}{dz} \right) . \qquad \text{(E.4)}$$